MULTISCALE MODELING OF THE DYNAMIC RESPONSE OF COMPOSITE STRUCTURES

By

Tong Hui

Dissertation
Submitted to the Faculty of the
Graduate School of Vanderbilt University
in partial fulfillment of the requirements
for the degree of
DOCTOR OF PHILOSOPHY
in
Civil Engineering
August, 2014
Nashville, Tennessee

Approved:
Caglar Oskay, Ph.D.
Prodyot K. Basu, Ph.D.
Ravindra Duddu, Ph.D.
Haoxiang Luo, Ph.D.
Sankaran Mahadevan, Ph.D.

For Dad, Mom, Dan and Daihong

ACKNOWLEDGEMENTS

Firstly, I would like to express my special thanks to my research advisor Dr. Caglar Oskay for his persistent guidance during my research at Vanderbilt University. He has provided me with tremendous support and encouragement in my academic and career paths. Without his advice and support, it would have been impossible to wind my way through the difficulties of this research.

I would like to acknowledge the remaining members of my Ph.D. committee: Dr. Prodyot Basu, Dr. Ravindra Duddu, and Dr. Haoxiang Luo and Dr. Sankaran Mahadevan. I thank them for the knowledge they provided in class and for the guidance and time they gave in serving on my committee.

I am grateful to have been working with so many intelligent people at Vanderbilt University. Particularly, Dr. Robert Crouch has provided me with enormous help in my research and has always inspired me by thinking out of the box. I would also like to express my appreciation to the remaining members of my research group who have been sharing brilliant ideas and discussions at all times. Besides, I cannot make the achievements in my research without the academic preparation at Xi'an Jiaotong University in China. I was equipped with solid basics in solid mechanics during the six-year learning at Xi'an Jiaotong University. My great thanks go to Dr. Yiheng Chen, Dr. Yifeng Hu and Dr. Qun Li from whom I had learned a lot.

Nashville is where I began my American journey. I am more than grateful to my friends here for their precious friendships and kindly help to me during the five-year time in Nashville.

At last, I would like to give my deepest thanks to my parents, Feihu Hui and Chuyin Tang, who have supported me wholeheartedly in everything I have chosen. I can never make this far without their unconditional support and love. I also thank my brother Dan Hui and my wife Daihong Yuan for their support and love. They are

my best friends, and I cannot fathom life without them.

This research was supported by the National Science Foundation.

TABLE OF CONTENTS

Chapter

Appendices

LIST OF TABLES

LIST OF FIGURES

CHAPTER 1

INTRODUCTION

1 Motivation

Composites and other heterogeneous materials exhibit complex response patterns when subjected to dynamic loading conditions due to the intrinsic wave interactions at the interfaces between material constituents. The complexity of dynamic responses in heterogeneous materials also provides tremendous opportunities for devising tailored microstructures with optimal functional characteristics such as impact and blast resistance, health monitoring and others. The development of such tailored microstructures for optimal performance requires a deeper understanding of the pertinent microstructure-property relationships. Specifically, heterogeneous materials exhibit wave dispersion when the characteristic length of traveling waves approaches the size of material microstructure [58, 64], altering the shape and velocity of propagating waves. The realization of this phenomena dates back to the classical works of Cosserat and Cosserat [22], Mindlin [45], and Eringen [29]. The effects of micro-inertia and dispersion have been recently modeled using a number of approaches such as gradient enhancement [14], time-harmonic Bloch expansions [66], scale bridging through Hamilton's principle [77], and models based on Mindlin's theory [28, 35]. These approaches typically incorporate high order strain and inertia gradient terms to the macroscopic equations of motion, which has been demonstrated to be effective in the context of elastic composites.

The dispersion relation between wave frequency and wavenumber in the frequency domain displays a banded structure with alternating passbands and stopbands. Stopbands refer to frequency bands within which the wave propagation is completely blocked. Band structures were found in electromagnetic range (i.e., photonic bandgaps) [79, 80] as well as in the acoustic range (i.e., phononic bandgaps) [41, 67, 75]. In order to evaluate the reveal evanescent wave fields and bandgap structure, both the real and imaginary components of wavenumber must be included [69, 70]. Suzuki and Yu [70] and Andrianov et al. [6] employed the Floquet-Bloch theorem to reveal the appearance of bandgaps in photonics and phononic ranges, respectively.

One of the main foci of this dissertation is the predictive modeling of viscoelastic composite materials subjected to dynamic loadings. Viscoelastic composites are well-known for attenuating wave propagation due to material dissipation. A good example is polyurea based composite structures. Polyurea have been shown to improve the survivability of structures subjected to blast and impact loadings. The mitigative effects of polyurea on a number of different structural materials, including steel [3, 4, 27, 37, 78] and composites [9, 36] have been subject to a number of recent investigations. A predictive model for wave propagation in viscoelastic composites may serve to the optimal design of microstructures for satisfactory dynamic responses (i.e., blast mitigation).

The previously discussed scale disparity between a composite structure and the small scale interplay of composite constituents provides an example of a problem with multiple spatial scales. The mathematical homogenization theory with multiple spatial scales provides a rigorous methodology for modeling wave propagation in heterogeneous materials. Rooted in the works of Bakhvalov and Panasenko [11], Benssousan et al. [15], Sánchez-Palencia [65] and others, the multiscale homogenization theory has been used to evaluate the mechanical response of heterogeneous materials under static and quasi-static loading, as well as dynamic problems involving long wavelengths compared to the characteristic size of the heterogeneity (e.g., [24, 38]). The multiscale homogenization theory has also been employed to devise dispersion models for dynamic response of linear elastic heterogeneous materials in the context of one-dimensional and multi-dimensional problems [6, 12, 19, 30]. This dissertation provides a promising research path by proposing a multiscale approach accounting for wave dispersion in viscoelastic composites. Specifically, This multiscale approach for modeling the dynamic response of viscoelastic composites links the global structural response to the wave dispersion and dissipation in micro-heterogeneities. When wave dispersion is considered in viscoelastic composites, the reproduction of nonlinear responses with high resolution is required to accurately reveal wave propagation in micro-heterogeneities.

The primary goal of this dissertation is to develop a new multiscale homogenization model for wave propagation in elastic and viscoelastic composite structures within dynamic applications.

1. Computational models have been developed and numerical investigations have been performed for blast response of polyurea coated composite structures;

2. A novel computational homogenization-based multiscale approach has been devised, which accounts for micro-heterogeneity induced wave dispersion and viscoelastic material dissipation;

3. The effects of micro-heterogeneity induced wave dispersion on the dynamic response of composite structures have been investigated.

2 Dissertation Organization

The first research objective is addressed by computationally investigating a polyurea layered E-glass reinforced vinyl-ester (EVE) composite panel subjected to blast in Chapter 2. The blast mitigation of polyurea on the EVE composite is quantitatively measured through the deflection of the composite panel and is enhanced by parametric optimizations of the thickness and confinement of polyurea layer. The second and third objectives are responded in Chapter 3 through 5. In Chapter 3, a semi-analytical homogenization solution incorporating high order asymptotic terms is derived for one-dimensional wave propagation in viscoelastic composite structures.

The solution is used to predict the wave dispersion and dissipated energy in the numerical examples. Chapter 4 presents a multi-dimensional, high order homogenization model for elastic composite materials subjected to dynamic loading conditions. The high order asymptotic terms are considered to include micro-inertia effects caused by the impedance contrast at the microscale. The finite element solution for the microscale influence functions and the homogenized macroscale problem is developed and verified against the direct finite element solution in predicting wave propagation with strong dispersions. In Chapter 5, a complex high order homogenization defined in the Laplace domain is presented for multi-dimensional wave propagation in viscoelastic composite structures. The model is based on the homogenization procedure discussed in Chapter 4 and is developed in the Laplace domain allowing the representation of linear viscoelastic constitutive relationship using a proportionality law. The effects of wave dispersion on wave propagation, attenuation and energy dissipation are discussed. The work in this dissertation is summarized in Chapter 6.

CHAPTER 2

COMPUTATIONAL MODELING OF POLYUREA LAYERED COMPOSITES SUBJECTED TO BLAST

1 Introduction

This chapter provides a computational modeling of polyurea layered composite structures subjected to blast. The application of polyurea coatings on structures [9] have been recently shown to dramatically improve the blast resistance. By conducting the research, the understanding of how the presence of polyurea layers can mitigate blast will be gained.

Polyurea exhibits nearly incompressible, viscoelastic response with sensitivity to pressure, strain-rate, and temperature [5]. At high strain-rate, polyurea transitions from rubbery to glassy state, causing an increase in energy absorption capacity [82]. A number of recent experimental and theoretical investigations shed light into the mechanical response characteristics of polyurea such as rate effects, hysteresis and cyclic softening [82], influence of stoichiometry, inertial effects [33, 62], wave propagation characteristics [60], among others. Constitutive laws have also been proposed to model the high-strain rate behavior of polyurea. Amirkhizi *et al.* [5] developed a viscoelastic constitutive model based on split Hopkinson bar experiments. This model incorporates the effect of temperature based on time-temperature transformation idea, and pressure sensitivity. Li and Lua [42] extended Amirkhizi's model to include nonlinear viscous effects. Elsayed [26] developed a multi-network model, which has the capability to capture hysteresis, rate-effects, plastic deformation, micro-inertia effects and temperature dependence.

In this chapter, we computationally investigate the blast response of a E-glass fiber reinforced vinyl-ester (EVE) composite panel layered with polyurea, based on the experimental data provided by Tekalur *et al.* [72]. Polyurea is modeled using the constitutive model proposed by Amirkhizi et al. [5]. A multiscale computational model for the EVE composite with rate-dependent damage evolution and adiabatic heating effects is devised. Blast response of EVE composite is simulated using the proposed model and the numerical results are compared to the experimental data. We investigate the blast response of three polyurea layered EVE composite panels with different layup configurations. In the numerical simulation, polyurea is shown to have favorable mitigation effect on blast especially when the polyurea layer is sandwiched between the EVE composite panels. A parametric investigation is conducted to search for the approach to enhance the blast mitigation effect of polyurea. The numerical analysis reveals that better survivability is obtained by increasing the thickness or through confinement of the polyurea layer.

2 Modeling Approach

We consider a composite structure occupying domain Ω, subjected to high-rate loading. The dynamic response of the composite is governed by the momentum balance equation:

$$\boldsymbol{\nabla} \cdot \bar{\boldsymbol{\sigma}}\left(\mathbf{x}, t\right) + \bar{\mathbf{b}}\left(\mathbf{x}, t\right) = \bar{\rho}\left(\mathbf{x}, t\right) \ddot{\bar{\mathbf{u}}}\left(\mathbf{x}, t\right); \qquad \mathbf{x} \in \Omega; \qquad t \in [0, t_{\mathrm{o}}] \tag{1}$$

in which, $\bar{\boldsymbol{\sigma}}$ and $\bar{\mathbf{u}}$ denote the stress and displacement fields, respectively; $\bar{\mathbf{b}}$ the body force; $\bar{\rho}$ the density; and, $\mathbf{x}$ and t denote spatial and temporal coordinates, respectively; Superscribed dot denotes the time derivative. Overbar indicates that the corresponding field is associated with an equivalent homogeneous representation of the heterogeneous medium. The structure is subjected to initial and boundary conditions:

$$\begin{aligned}
\bar{\mathbf{u}}\left(\mathbf{x},t\right) &= \hat{\mathbf{u}}\left(\mathbf{x}\right); \quad \mathbf{x}\in\Omega; \quad t=0 && (2)\\
\dot{\bar{\mathbf{u}}}\left(\mathbf{x},t\right) &= \hat{\mathbf{v}}\left(\mathbf{x}\right); \quad \mathbf{x}\in\Omega; \quad t=0 && (3)\\
\bar{\mathbf{u}}\left(\mathbf{x},t\right) &= \tilde{\mathbf{u}}\left(\mathbf{x},t\right); \quad \mathbf{x}\in\Gamma_u; \quad t\in[0,t_\mathrm{o}] && (4)\\
\bar{\boldsymbol{\sigma}}\left(\mathbf{x},t\right)\cdot\mathbf{n} &= \tilde{\mathbf{t}}\left(\mathbf{x},t\right); \quad \mathbf{x}\in\Gamma_t; \quad t\in[0,t_\mathrm{o}] && (5)
\end{aligned}$$

where, $\hat{\mathbf{u}}$ and $\hat{\mathbf{v}}$ are prescribed initial displacement and velocity fields, respectively; $\tilde{\mathbf{u}}$ and $\tilde{\mathbf{t}}$ the prescribed displacements and tractions on the boundaries Γ_u and Γ_t, respectively, ($\Gamma=\Gamma_u\cup\Gamma_t$ and $\Gamma_u\cap\Gamma_t=\emptyset$); and; $\mathbf{n}$ the unit normal to Γ_t.

In this chapter, the failure response of the composite structure is evaluated by employing explicit finite element method to evaluate Eqs. 1-5, and the constitutive models for constituent materials with prescribed blast profiles (i.e., Eq. 5).

3 Constitutive Failure Model for Composite Constituents under High Rate Loading

The failure response of the composite material is modeled based on the eigendeformation-based reduced order computational homogenization (EHM) method recently proposed by Oskay and co-workers [24, 54, 81]. In the EHM method, microstructural information (e.g., localization operators, concentration tensors, influence functions) in the representative volume element (RVE) of EVE is precomputed prior to the analysis of EVE composite at the macroscale. The inelastic response fields within the RVE are taken to be piecewise constant (in space) within subdomains of the RVE corresponding to each phase. The proposed reduced order multiscale approach provides significant computational efficiency without compromising on solution accuracy when compared to standard computational homogenization approach, which requires repeated evaluation of the full scale RVE problem at each integration point of macroscopic domain for each time step. The details of the EHM method are not the focus of this dissertation and can be found in the work by Crouch and Oskay [24], and are therefore not presented in this dissertation. In this section, we propose a strain-rate dependent and temperature-dependent constitutive formulation to describe the failure response of the composite constituents. Strain-rate dependence is introduced through a Perzyna-type visco-damage formulation to account for embrittlement and hardening observed at high rates, as well as to avoid mesh sensitivity observed in standard continuum damage formulations. Temperature-dependence is introduced to investigate the effect of localized adiabatic heating on the blast response, which has been previously argued to have a significant effect on localization of damage under high rate loading Tekalur et al. [71].

The composite material is considered to be formed by the repetition of a locally periodic microstructure, which consists of n_{ph} phases (e.g., matrix and fiber). The behavior of each composite constituent is idealized based on a rate- and temperature-dependent continuous damage mechanics model. The phase-average stress within phase, η, is expressed as:

$$\boldsymbol{\sigma}^{(\eta)} = \mathbf{L}^{(\eta)} : \mathbf{e}^{(\eta)} = \mathbf{L}^{(\eta)} : \left(\boldsymbol{\epsilon}^{(\eta)} - \boldsymbol{\mu}^{(\eta)}\right) \tag{6}$$

where, $\boldsymbol{\epsilon}^{(\eta)}$, $\boldsymbol{\mu}^{(\eta)}$ and $\mathbf{e}^{(\eta)}$ are phase average total, inelastic and elastic strain tensors, respectively; $\mathbf{L}^{(\eta)}$ the tensor of elastic moduli; and, colon denotes double inner product operator.

Under high-rate loading conditions, the phase-average inelastic strain is expressed in terms of the scalar damage variable, $\omega^{(\eta)} \in [0, 1)$, indicating the state of damage, and localized adiabatic heating induced thermal strains:

$$\sum_{\gamma} \left[\delta_{\eta\gamma}\mathbf{I} - \mathbf{P}^{(\eta\gamma)}\omega^{(\eta)}\right] : \boldsymbol{\mu}^{(\gamma)} = \omega^{(\eta)}\mathbf{A}^{(\eta)} : \bar{\boldsymbol{\epsilon}}\left(\mathbf{x}, t\right) - \alpha^{(\eta)}\left[1 - \omega^{(\eta)}\right]\left[T^{(\eta)} - T_{\text{ref}}\right]\boldsymbol{\delta} \tag{7}$$

in which, $\bar{\boldsymbol{\epsilon}}$ is the RVE average (macroscale) strain; $\alpha^{(\eta)}$ the coefficient of thermal expansion; $T^{(\eta)}$ and T_{ref} the current and reference temperatures, respectively; $\boldsymbol{\delta}$ and

$\mathbf{I}$ denote the second and fourth order identity tensors, respectively; and, $\delta_{\eta\gamma} = 1$ if $\eta = \gamma$ and vanish otherwise. the fourth order coefficient tensors, $\mathbf{P}^{(\eta\gamma)}$ and $\mathbf{A}^{(\eta)}$ are expressed as:

$$\mathbf{P}^{(\eta\gamma)} = \frac{1}{|\Theta^{(\eta)}|} \int\limits_{\Theta^{(\eta)}} \int\limits_{\Theta^{(\gamma)}} \mathbf{g}\left(\mathbf{y}, \hat{\mathbf{y}}\right) d\hat{\mathbf{y}} d\mathbf{y}; \quad \mathbf{A}^{(\eta)} = \frac{1}{|\Theta^{(\eta)}|} \int\limits_{\Theta^{(\eta)}} \mathbf{I} + \mathbf{G}\left(\mathbf{y}\right) d\mathbf{y} \tag{8}$$

where, $\Theta^{(\eta)}$ denotes the domain of the constituent, η; and, $\mathbf{g}$ and $\mathbf{G}$ are the inelastic deformation-induced and elastic polarization functions of the RVE problem, which are numerically evaluated based on the EHM method. Equation 7 is derived from the microscopic equilibrium as well as the constitutive equations, and provides the inelastic strains that *a-priori* satisfy the equilibrium at the microscopic (i.e. RVE) scale [54].

The RVE average (macroscale) stress of the overall composite material is expressed in terms of the macroscale strain and the phase average inelastic strains as:

$$\bar{\boldsymbol{\sigma}} = \bar{\mathbf{L}} : \bar{\boldsymbol{\epsilon}} + \sum_{\gamma} \bar{\mathbf{M}}^{(\gamma)} : \boldsymbol{\mu}^{(\gamma)} \tag{9}$$

in terms of the coefficient tensors, $\bar{\mathbf{M}}^{(\gamma)}$ and $\bar{\mathbf{L}}$,

$$\bar{\mathbf{M}}^{(\gamma)} = \sum_{\eta} \mathbf{L}^{(\eta)} : \left[c^{(\eta)} \mathbf{P}^{(\eta\gamma)} - \delta_{\eta\gamma} \mathbf{I}\right]; \quad \bar{\mathbf{L}} = \sum_{\eta} c^{(\eta)} \mathbf{L}^{(\eta)} : \mathbf{A}^{(\eta)} \tag{10}$$

where, $c^{(\eta)}$ denotes the volume fraction of phase η within the RVE.

Localized adiabatic heating during high-rate loading is taken to be due to reversible elastic deformations, as well as the irreversible damage process [1, 76]:

$$\rho^{(\eta)} C_p^{(\eta)} \dot{T}^{(\eta)} = \Upsilon^{(\eta)} \boldsymbol{\sigma}^{(\eta)} : \dot{\boldsymbol{\mu}}^{(\eta)} - 3K^{(\eta)} \alpha^{(\eta)} \left(1 - \omega^{(\eta)}\right) \mathrm{tr}(\dot{\mathbf{e}}^{(\eta)}) T^{(\eta)} + \frac{1}{3} \mathrm{tr}(\boldsymbol{\sigma}^{(\eta)}) \mathrm{tr}(\dot{\mathbf{e}}^{(\eta)}) \tag{11}$$

where, $C_p^{(\eta)}$ and $\rho^{(\eta)}$ represent the specific heat at constant pressure and density of phase η, respectively; $\Upsilon^{(\eta)}$ the ratio of inelastic work converted to heat; and, $K^{(\eta)}$ denotes bulk modulus; and, $\mathrm{tr}(\cdot)$ is the trace operator.

We consider a damage evolution model with viscous regularization of the Perzyna type [57] to idealize the rate-dependent response of the phases. Similar rate-dependent damage models with viscoplastic regularization have been proposed for failure modeling of other quasi-brittle materials [25, 68]. Rate-independent continuum damage mechanics models are well-known to exhibit spurious mesh sensitivity when loading extends to the softening regime. This phenomenon is marked by the localization of strains within the size of a finite element. Viscous regularization of the damage model employed in this study has been shown to alleviate damage localization and spurious mesh sensitivity [50, 55].

The effect of localized heating on the rate-dependent damage evolution is introduced. Let f be the temperature-dependent damage potential function in the form:

$$f\left(\nu^{(\eta)}, r^{(\eta)}, T^{(\eta)}\right) = \phi\left(\nu^{(\eta)}\right) - \phi\left(r^{(\eta)}\right)\left[1 - \left(\frac{T^{(\eta)} - T_{\mathrm{ref}}^{(\eta)}}{T_{\mathrm{m}}^{(\eta)} - T_{\mathrm{ref}}^{(\eta)}}\right)\right] \leq 0 \tag{12}$$

in which, $\nu^{(\eta)}$ is the phase damage equivalent strain; $r^{(\eta)}$ the damage hardening variable; and, $T_{\mathrm{m}}^{(\eta)}$ the melting temperature of constituent phase η. ϕ is the damage evolution function. The evolution equations for the damage and hardening variables are given as:

$$\dot{\omega}^{(\eta)} = \lambda \frac{\partial \phi}{\partial \nu^{(\eta)}}; \quad \dot{r}^{(\eta)} = \lambda \tag{13}$$

in which, the consistency parameter, λ, is described by the power law expression:

$$\lambda = \frac{1}{q^{(\eta)}} \langle f \rangle^{p^{(\eta)}} \tag{14}$$

where, $\langle \cdot \rangle \equiv \left((\cdot) + |\cdot| \right)/2$ denotes MacCauley brackets; and $p^{(\eta)}$ and $q^{(\eta)}$ are material parameters describing the rate-dependent response.

The phase damage equivalent strain is defined as

$$\nu^{(\eta)} = \sqrt{\frac{1}{2}\left(\mathbf{F}^{(\eta)} \hat{\boldsymbol{\epsilon}}^{(\eta)}\right) : \mathbf{L}^{(\eta)} : \left(\mathbf{F}^{(\eta)} \hat{\boldsymbol{\epsilon}}^{(\eta)}\right)} \tag{15}$$

in which, $\hat{\boldsymbol{\epsilon}}^{(\eta)}$ is the principal strain tensor; $\mathbf{F}^{(\eta)} = \mathrm{diag}(h_1^{(\eta)}, h_2^{(\eta)}, h_3^{(\eta)})$ is a diagonal weighting matrix introduced to differentiate damage growth rate in tensile and compressive loading:

$$h_{\xi}^{(\eta)} = \frac{1}{2} + \frac{1}{\pi} \arctan \left({c_1}^{(\eta)} \hat{\epsilon}_{\xi}^{(\eta)} \right); \quad \xi = 1, 2, 3 \tag{16}$$

where, $\hat{\epsilon}_{\xi}^{(\eta)}$ are components of $\hat{\boldsymbol{\epsilon}}^{(\eta)}$; and, $c_1^{(\eta)}$ is a material parameter.

A power law is considered to characterize the damage evolution function, ϕ, which increases monotonically as a function of the damage equivalent strain to satisfy Clausius-Duhem inequality for thermodynamic consistency:

$$\phi \left(X^{(\eta)} \right) = a^{(\eta)} \left\langle X^{(\eta)} \right\rangle^{b^{(\eta)}}; \quad \phi \left(X^{(\eta)} \right) \leq 1 \tag{17}$$

in which, X denotes either ν or r; and, $a^{(\eta)}$ and $b^{(\eta)}$ are material parameters. For each constituent, parameters $a^{(\gamma)}$ and $b^{(\gamma)}$ define the evolution of damage as a function of loading history; $c_1^{(\gamma)}$ models the strength anisotropy along the compression and tensile directions; and, $p^{(\gamma)}$ and $q^{(\gamma)}$ model the rate-dependent behavior.

4 Polyurea Model

The mechanical response of polyurea subjected to blast is modeled using the temperature- and pressure-dependent viscoelastic constitutive law proposed by Amirkhizi *et al.* [5]. Cauchy stress tensor is expressed in terms of the hereditary integral as a function of the shear relaxation modulus and the bulk modulus as:

$$\bar{\boldsymbol{\sigma}} = \int_0^t 2G^{(p)} \left(t, \tau \right) \mathbf{D}' \left(\tau \right) d\tau + K^{(p)} \frac{\ln J}{J} \boldsymbol{\delta} \tag{18}$$

where, $\mathbf{D}'(t)$ is the deviatoric component of the deformation-rate tensor, $\mathbf{D} = \left(\mathbf{L}^T + \mathbf{L} \right) / 2$; $\left(\mathbf{L} = \dot{\mathbf{F}} \mathbf{F}^{-1} \right)$ is the velocity gradient and $\mathbf{F}$ the deformation gradient); and, $J = \det(\mathbf{F})$ the jacobian of the deformation gradient. The bulk modulus of polyurea, $K^{(p)}$ is taken to be a linear function of the temperature:

$$K^{(p)} \left(T \right) = K^{(p)} \left(T_{\text{ref}} \right) + m^{(p)} \left(T - T_{\text{ref}} \right) \tag{19}$$

in which, $K^{(p)}(T_{\text{ref}})$ is the bulk modulus of polyurea at reference temperature; and, $m^{(p)}$ is the temperature sensitivity parameter.

The shear relaxation modulus, $G^{(p)}$, is expressed based on an exponential (Prony) series representation:

$$G^{(p)}(t,\tau) = \frac{T(\tau)}{T_{\text{ref}}} G_{\infty}^{(p)} \left(1 + \sum_{i=1}^{n} p_i^{(p)} \exp\left[\frac{-(\xi(t) - \xi(\tau))}{q_i^{(p)}} \right] \right); \quad \tau \in [0, t] \tag{20}$$

where, G_{∞} is the steady state shear modulus of polyurea; $p_i^{(p)}$ and $q_i^{(p)}$ are material constants; and:

$$\xi(t) = \int_0^t \frac{1}{a(T(\tau), P(\tau))} d\tau \tag{21}$$

in which, $P = -\text{tr}(\boldsymbol{\sigma})/3$ is pressure; $a(T, P)$ is the Williams-Landel-Ferry (WLF) empirical time-temperature-pressure shift function of the form:

$$\log(a(T, P)) = \frac{A^{(p)}\left(T - C_{tp}^{(p)} P - T_{\text{ref}}\right)}{B^{(p)} + T - C_{tp}^{(p)} P - T_{\text{ref}}} \tag{22}$$

where, $A^{(p)}$ and $B^{(p)}$ are time-temperature coefficients; and, $C_{tp}^{(p)}$ the time-pressure coefficient.

Viscous dissipation causes localized adiabatic heating in polyurea during blast:

$$\dot{T} = \frac{1}{C_{\text{v}}^{(p)}} \dot{W}_d = \frac{2G_{\infty}^{(p)}}{C_{\text{v}}^{(p)}} \frac{T(t)}{T_{\text{ref}}} \sum_{i=1}^{n} \frac{p_i^{(p)}}{q_i^{(p)}} \boldsymbol{\epsilon}_d^i(t) : \boldsymbol{\epsilon}_d^i(t) \tag{23}$$

in which, W_d is the dissipated work per unit reference volume; and, $C_{\text{v}}^{(p)}$ is the heat capacity per original volume; and,

$$\boldsymbol{\epsilon}_d^i(t) = \int_0^t \exp\left[\frac{-(\xi(t) - \xi(\tau))}{q_i^{(p)}} \right] \mathbf{D}'(\tau)\, d\tau \tag{24}$$

The material parameters of polyurea are calibrated based on Kolsky (Split Hopkinson) pressure bar experiments. The polyurea material parameters employed in our simulations are provided by Ref. [5] and summarized in Table 4.

Table 1: Calibrated parameters of the polyurea constitutive model.

$\rho^{(p)}$ [kg/m^3]	$A^{(p)}$	$B^{(p)}$ [K]	$m^{(p)}$ [GPa/K]	$K_{\text{ref}}^{(p)}$ [GPa]
1070	-10	107.54	-0.015	4.948
$C_{tp}^{(p)}$ [K/GPa]	$T_{ref}^{(p)}$ [K]	$C_V^{(p)}$ [J/mm^3 K]	$G_\infty^{(p)}$ [GPa]	
7.2	273	1.977×10^{-3}	0.0224	
$p_1^{(p)}$	$p_2^{(p)}$	$p_3^{(p)}$	$p_4^{(p)}$	
0.8458	1.686	3.594	4.342	
$q_1^{(p)}$ [ms]	$q_2^{(p)}$ [ms]	$q_3^{(p)}$ [ms]	$q_4^{(p)}$ [ms]	
463.4	0.06407	1.163×10^{-4}	7.321×10^{-7}	

5 Blast Simulation of EVE/Polyurea Composites

In this section, we numerically investigate the response of EVE and polyurea-layered EVE composite specimens subjected to blast. We employ the specimen geometry and the loading condition in the experiment provided by Tekalur and co-workers [72]. The geometry and discretization of composite panels are illustrated in Fig. 1. The EVE panels are 230 mm × 102 mm × 6 mm in length, width and thickness, respectively. The fill and warp fibers are oriented along x_1 and x_2 directions respectively. The panel is simply supported over a span of 152 mm along the vertical direction. The blast profile is applied at the center of the panel within a circular area with radius of 38 mm. Only a quadrant of the panel is modeled and simulated by exploiting the symmetry of the panel geometry, loading and boundary conditions. We consider four panel configurations: (1) EVE panel only (E-configuration; Fig. 1b); (2) 6mm polyurea layer at the back face (EP-configuration; Fig. 1d); (3) 6mm polyurea layer at the front face (PE-configuration; Fig. 1e); (4) 6mm polyurea layer sandwiched by two 3 mm-thick EVE panels (EPE-configuration; Fig. 1f). Fig. 2 illustrates the blast profiles employed in this study. The shock wave profile is characterized by a peak blast (reflected wave) amplitude, P_{ref}, incident wave amplitude, P_{inc}, and the time duration, $\lambda = 1.5$ ms, within which reflected wave amplitude decays to incident wave amplitude. Linear and nonlinear profiles are considered. The nonlinear wave profile

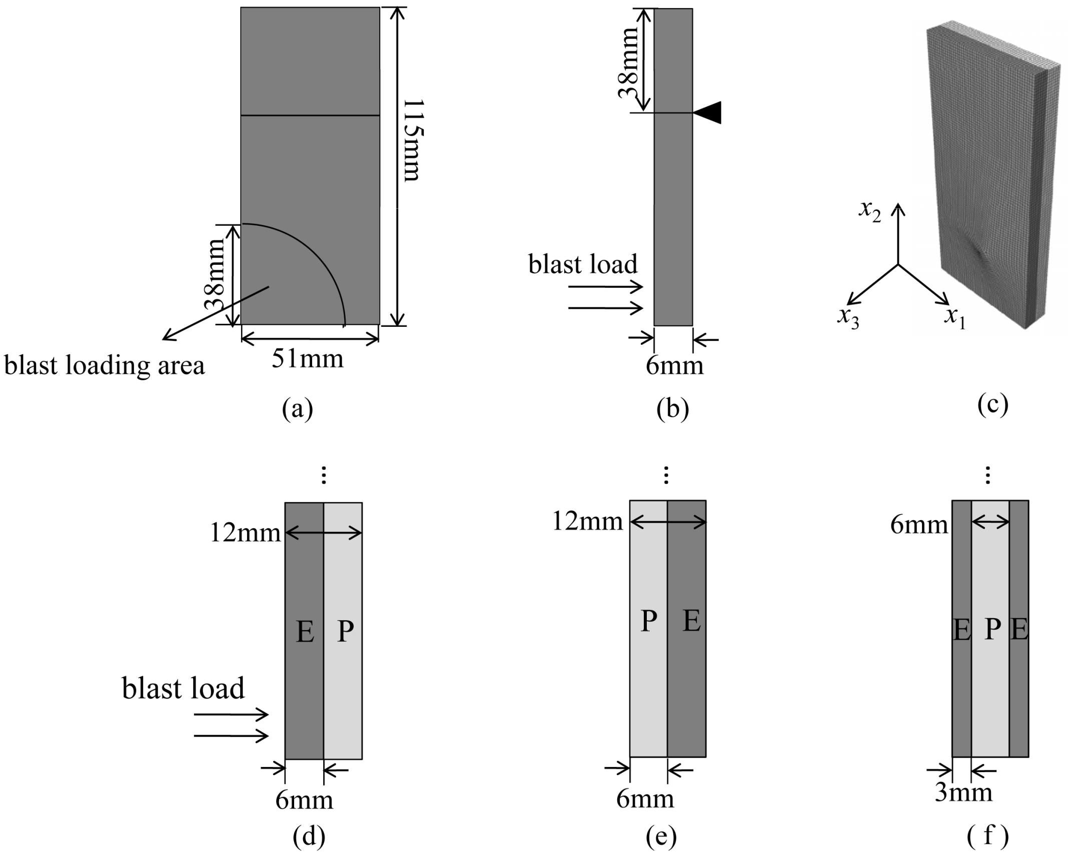

Figure 1: Setup of EVE and Polyurea layered EVE panels: (a) front view of EVE composite panel, (b) side view of EVE composite panel, (c) representative finite element model of polyurea layered EVE composite panel, (d) EP-conuration model, (e) PE-configuration model, (f) EPE-configuration model.

is generated by the expression:

$$P = \frac{\lambda P_{\text{inc}} P_{\text{ref}}}{P_{\text{inc}}\lambda + (P_{\text{ref}} - P_{\text{inc}})t} \tag{25}$$

5.1 Calibration of EVE Constituent Properties

The proposed multiscale computational model is applied to idealize the response of EVE composite employed in the experimental study provided in Ref. [72]. The elastic and failure properties are calibrated using available experimental data on quasi-

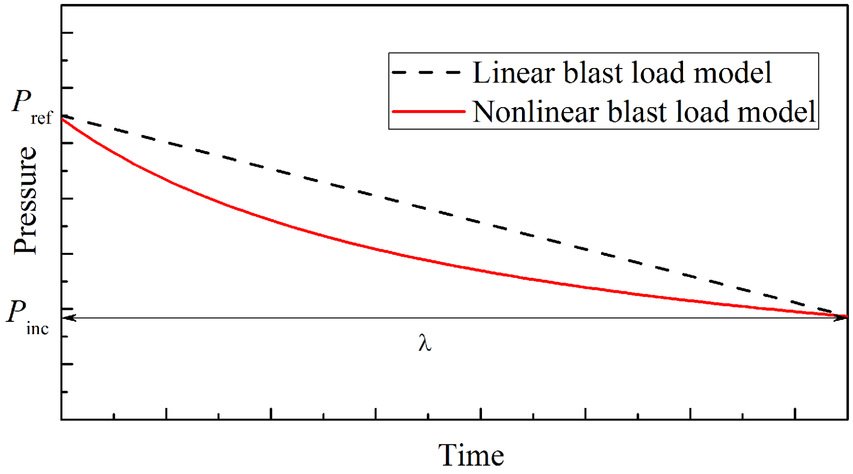

Figure 2: Blast profiles.

static and dynamic response of EVE composite specimens provided in references [52, 71]. The representative volume element (RVE) is idealized as a composition of three constituents: the vinyl ester matrix, fiber tows along the fill- and warp directions. The RVE of the woven composite material employed in the simulations is shown in Fig. 3. The microstructure of the composite contains 60.5% fiber by volume, with an unbalanced construction having 59% and 41% of fibers oriented along the warp and fill directions, respectively. The size of the RVE is 10mm × 12.5mm × 0.625mm along the fill, warp and thickness directions, respectively. Density, specific heat, and coefficient of thermal expansion for matrix and fiber phases employed in our investigations are obtained from Committee [21]. The experimentally determined quasi-static elastic properties of matrix and fiber are [63, 71]: $E_0^{(m)} = 3.4$ GPa, $E^{(f)} = 70$ GPa, and $\nu^{(m)} = \nu^{(f)} = 0.15$. At high strain rates the elastic modulus of overall composite is higher than those at quasi-static conditions [51, 52]. Within the blast rates and temperature considered in this study, E-glass fibers do not display significant strain rate effects. The elastic modulus of vinyl-ester matrix is taken to be a function of

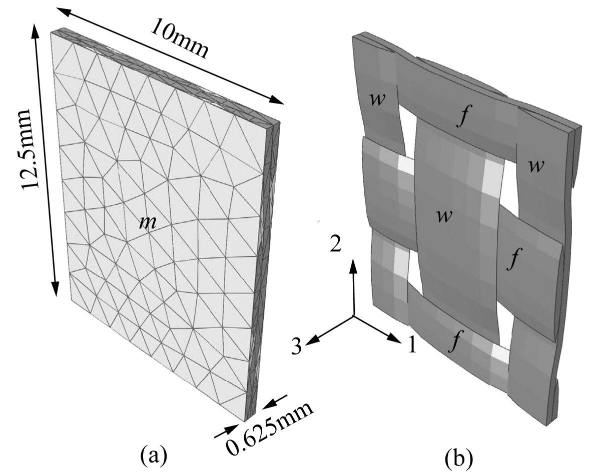

(a) (b)

Figure 3: (a) The representative volume for the woven composite material, (b) reduced order model for the RVE with three constituents: fill (horizontal) and warp (vertical) fibers and the matrix (transparent).

strain-rate based on a power law [52]:

$$E^{(m)} = E_0^{(m)} \left(1 + \left(\frac{\dot{\epsilon}^{(m)}}{\dot{\epsilon}_0^{(m)}} \right)^N \right) \tag{26}$$

where, $\dot{\epsilon}_0^{(m)} = 2060/\text{s}$ is the reference strain rate; and, $N = 0.73$. The quasi-static uniaxial compression and tension experiments conducted by Tekalur *et al.* [71], as well as the dynamic testing by Oguni and Ravichandran [52] are employed to calibrate the failure properties of the constituent phases. The fiber phase response is taken to be rate-independent [52] within the loading rates and temperature range considered in this study. The calibrated material parameters for each phase are summarized in

Table 2: Properties and calibrated parameters of EVE composite.

	E [GPa]	K [GPa]	ρ [kg/ m^3]	α [1/°C]	C_p [J/gK]	T_{ref} [K]
fiber	70	33.3	2620	5.4×10^{-6}	0.810	298
matrix	3.4	1.62	1230	45×10^{-6}	1.05	298
	a	b	c_1	q	p	
warp	0.17	6	-22	10^{-8}	2	
fill	0.32	6	0	10^{-8}	2	
matrix	1.4	2	0	2×10^{-6}	2	

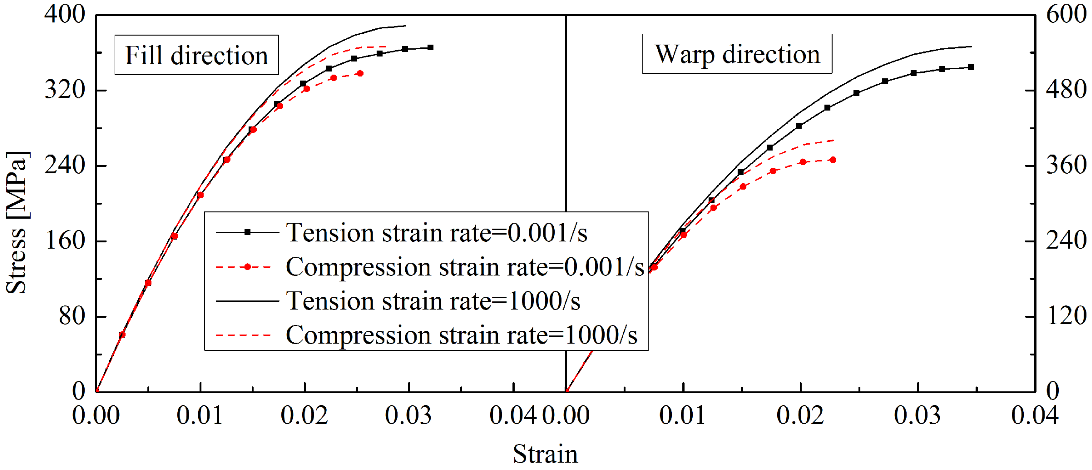

Figure 4: Simulated stress-strain curves of EVE composite for quasi-static and high strain loading in compression and tension directions.

Table 2 and the stress-strain curves at high and low strain rate are plotted in Fig. 4. The experimentally observed strength of the overall composite and the calibrated model predictions are compared in Table 3, which are in reasonable agreement.

5.2 Blast Response of EVE Panels

Table 3: EVE composite properties under quasi-static loading.

		Modulus [GPa]		Strength [MPa]		Poisson's ratio
		T[1]	C[2]	T	C	
warp	Experiment [71]	29.2	31.9	512.5	363.4	0.16
	Simulation	29.0	29.0	516.7 (0.82%)[3]	369.7 (1.7%)	0.15
fill	Experiment [71]	23.9	26.9	350.9	336.4	0.14
	Simulation	24.5	24.5	363.6 (3.6%)	337.9 (0.45%)	0.15

[1]Tension; [2]Compression; [3]difference between simulated and experimental results

The E-configuration panel is subjected to three loading profiles to assess the capability of the proposed model and investigate the effect of loading rate and damage induced adiabatic heating on structural response against blast. The loading profiles are parameterized as: $P_{\text{inc}} = 0.62$ MPa and $P_{\text{ref}} = 1.57$ MPa for the linear and nonlinear blast models; and $P_{\text{inc}} = 0.45$ MPa and $P_{\text{ref}} = 1.28$ MPa for the nonlinear blast model only. Figure 5a compares the numerical predictions of the linear and nonlinear blast profiles with the incident wave amplitude of 0.62 MPa, and the experimental measurement. The predicted displacement histories along the thickness direction at the center of the plate (center-point displacement, u_c) are in reasonable agreement with the experimental observation. The discrepancy between the predictions of the linear and nonlinear blast models illustrates the sensitivity of blast profiles on the structural response. The more realistic non-linear blast model provides a better fit with the experimental results especially at the later stages of deformation. In the remainder of the simulations, only the nonlinear blast profile is employed. The center-point displacement comparison between numerical simulation and experiment for incident wave amplitude of 0.45 MPa is plotted in Fig. 5b. In contrast to high incident wave amplitude simulation, the specimen does not completely fail and the displacement rebounds back after 1.1 ms. In all numerical investigations, the maximum observed strain rate throughout the specimen and loading history does not exceed 20/s. The rate effects, which are pronounced in the matrix material at high strain rate (i.e. > 1000/s [52]), therefore, do not significantly affect the blast response. In adiabatic heating process, maximum damage-induced temperature rise is achieved by setting Υ equal to 1 signifying that all of the damage work is converted into heat. The thermal profile of the composite specimen computed based on Eq. 11 throughout the loading history indicates that maximum temperature rise due to damage induced adiabatic heating is confined to less than 10 K. The burn observed along the surface of the specimens revealed in experimental studies is therefore unlikely to be due to damage induced heating.

5.3 Blast Response of Polyurea-Layered EVE Composites

We conducted a series of simulations to numerically investigate the mitigative effect of polyurea layer on the blast survivability of EVE composite panels. Three polyurea-EVE composite configurations illustrated in Figs. 1d-f are subjected to blast profiles.

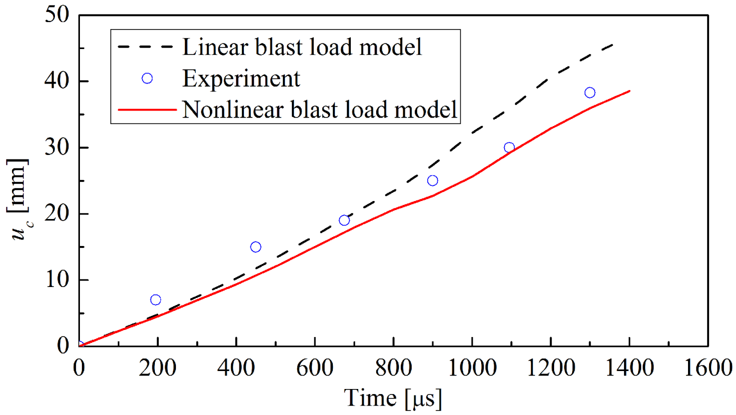

(a)

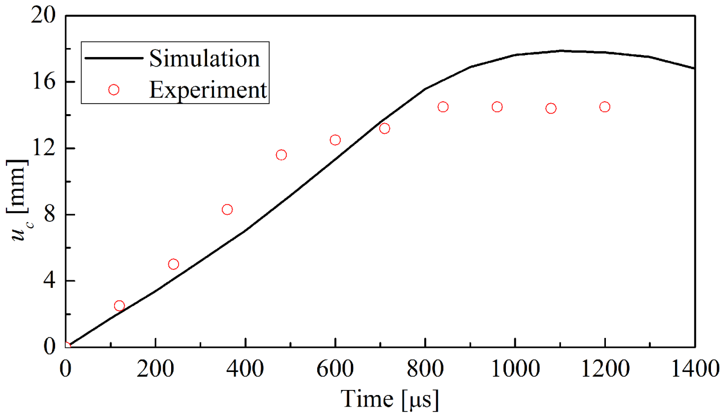

(b)

Figure 5: Comparison of experimental [72] and numerically predicted center-point displacements of E-configuration panels subjected to input pressure of (a) 0.62 MPa, and, (b) 0.45 MPa.

The incident pressure and reflected pressure are 0.75 MPa and 2.2 MPa, respectively, for EP- and PE-configurations; and, 0.75 MPa and 2.01 MPa, respectively, for EPE configuration. Figure 6 illustrates the simulated and experimentally observed center-point displacement (normalized by the combined thickness of the polyurea layer and EVE composite panel, d_t) histories for PE, EP and EPE configurations, respectively. For all three configurations, the numerical predictions display reasonable agreement with the experimental observations **[72]**, pointing to the adequacy of the proposed models in capturing the failure response of composite specimens.

The PE and EPE configurations resist the blast with only partial damage under the applied incident wave amplitude of 0.75 MPa, that is illustrated in Figs. 6a and 6c as the curve-down of center-point displacements. In contrast, the EP configuration fails under the applied blast magnitude. The highest mitigation effect is observed in the EPE configuration, in which the center-point displacement completely rebounds. The superior performance of PE configuration (compared to the EP configuration) is attributed to its higher resistance against compressive and shear failure of the substrate, which are predominant failure mechanisms [72], as well as dissipation of blast pressure within polyurea layer prior to reaching the composite substrate. All three simulations indicate that the presence of polyuea layer significantly mitigates blast response as evidenced by the reduction of the center-point displacement magnitude compared to the E-configuration despite higher applied blast pressure magnitudes for the polyurea-layered configurations. Figure 7 illustrates the snapshots of simulated matrix damage and deformation profiles during the blast of E and EP configurations in comparison with the experimental observation [72]. In all the simulations, the maximum rise in temperature within polyurea layers is 2 K. The highest strain-rates within the polyurea layers throughout the loading history are 150/s, 800/s and 50/s for the PE, EP and EPE configurations, respectively. The center-point displacement at the front face of the specimens are reported in all figures. The displacements at the center-point on the back face of the panel are nearly identical to the front face and no significant change of plate thickness was observed in the simulations.

The effects of debonding along the fiber-matrix interface within the EVE layers are also considered in this investigation. Numerical simulations by considering full-debonding along the fiber-matrix interfaces revealed that the state of damage along the these interfaces make little contribution to the deformation of the plate against blast. In addition, the experimental investigations [72] reveal no significant debonding between polyurea and EVE layers for the loading cases considered in this study. We

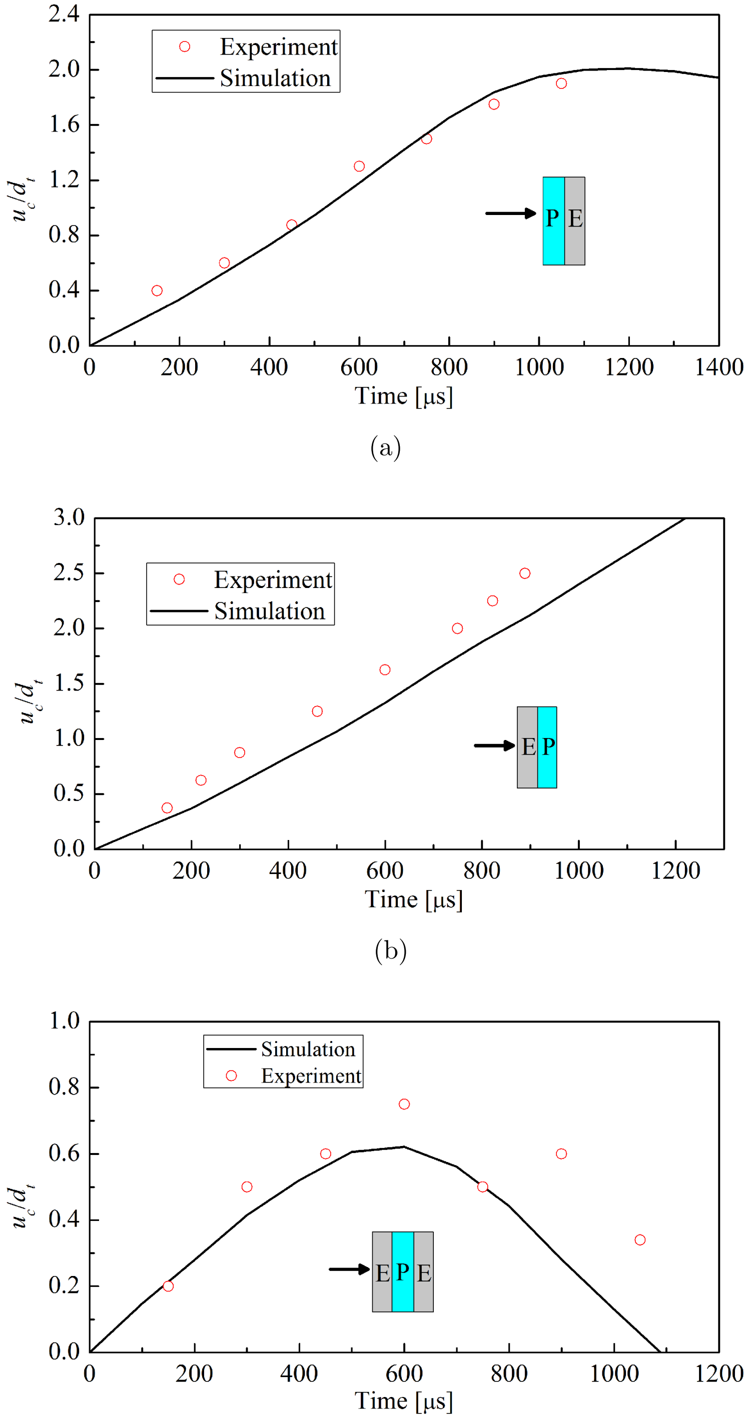

(a)

(b)

(c)

Figure 6: Comparison of experimental and numerically predicted normalized center-point displacements of (a) PE-configuration, (b) EP-configuration, and, (c) EPE-configuration panels subjected to input pressure of 0.75MPa.

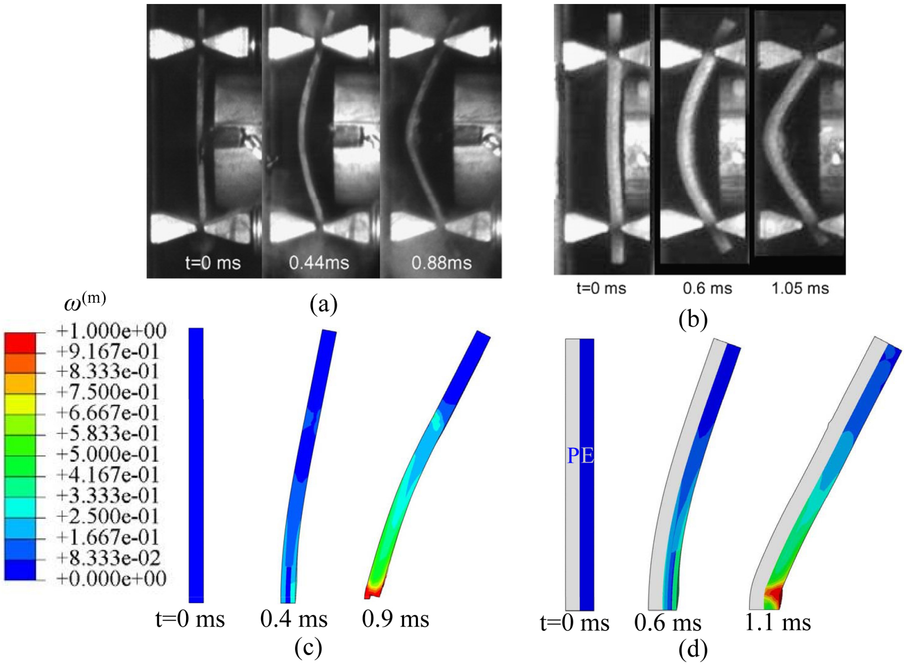

Figure 7: Displacement profiles of (a) experimentally observed [72] E-panel when P_{inc}=0.62MPa; (b) experimentally observed EP-panel when P_{inc}=0.75MPa; [72] (c) simulated E-panel when P_{inc}=0.62MPa; (d) simulated EP-panel when P_{inc}=0.75MPa.

therefore assume that the interfaces remain intact throughout the simulations.

The polyurea is a nearly incompressible material. We investigated the effect of confinement of the polyurea layers on the blast response and mitigation characteristics. The confinement effect is presented only for the EPE configuration, since the confinement effect is independent of the composite layup. The confinement effect is achieved by constraining the boundary displacement of the polyurea layer along its perimeter. Figure 8 compares the center-point displacements of the confined and unconfined EPE configurations. The center-point displacements at the initial stages of the loading are similar. In contrast, the peak displacement for the confined configuration is approximately 30% smaller compared to the unconfined configuration. The deformation for the unconfined configuration is significantly smaller throughout the rest of the loading history.

The thickness effect of polyurea layer are investigated as well. The PE, EP and

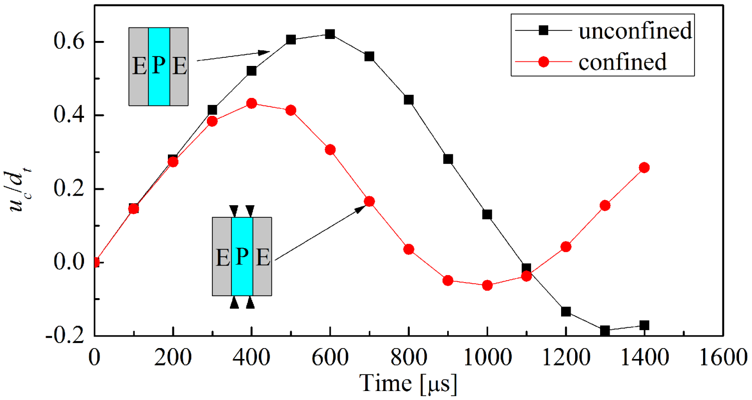

Figure 8: Effect of confinement on the evolution of center-point displacement in EPE-configuration.

EPE configurations are revisited by imposing 3mm, 6mm and 12mm thick polyurea layers with the same blast profile as before. Figure 9 shows the center-point displacement histories for the PE, EP and EPE configurations, respectively. For all the configurations, the increasing thickness of polyurea monotonically reduces the blast induced damage and the deformation of the composite panels. In the case of PE configuration, a 3mm thick polyurea layer fails to mitigate the blast response, and complete failure of the EVE composite layer is observed. In the case of EP configuration, the 12mm thick polyurea layer mitigates complete failure of the EVE composite layer, in contrast with the 3mm and 6mm thick polyurea layer configurations. All EPE panels with 3mm, 6mm and 12mm thick polyurea layers survive the blast, with no significant damage accumulation within the EVE composite layer in the case of 12mm thick polyurea configuration.

6 Conclusions

In the numerical modeling: a new failure model for EVE composites that accounts for strain-rate effects as well as the damage induced localized adiabatic heating was proposed to accurately model the response of EVE composites subjected to blast.

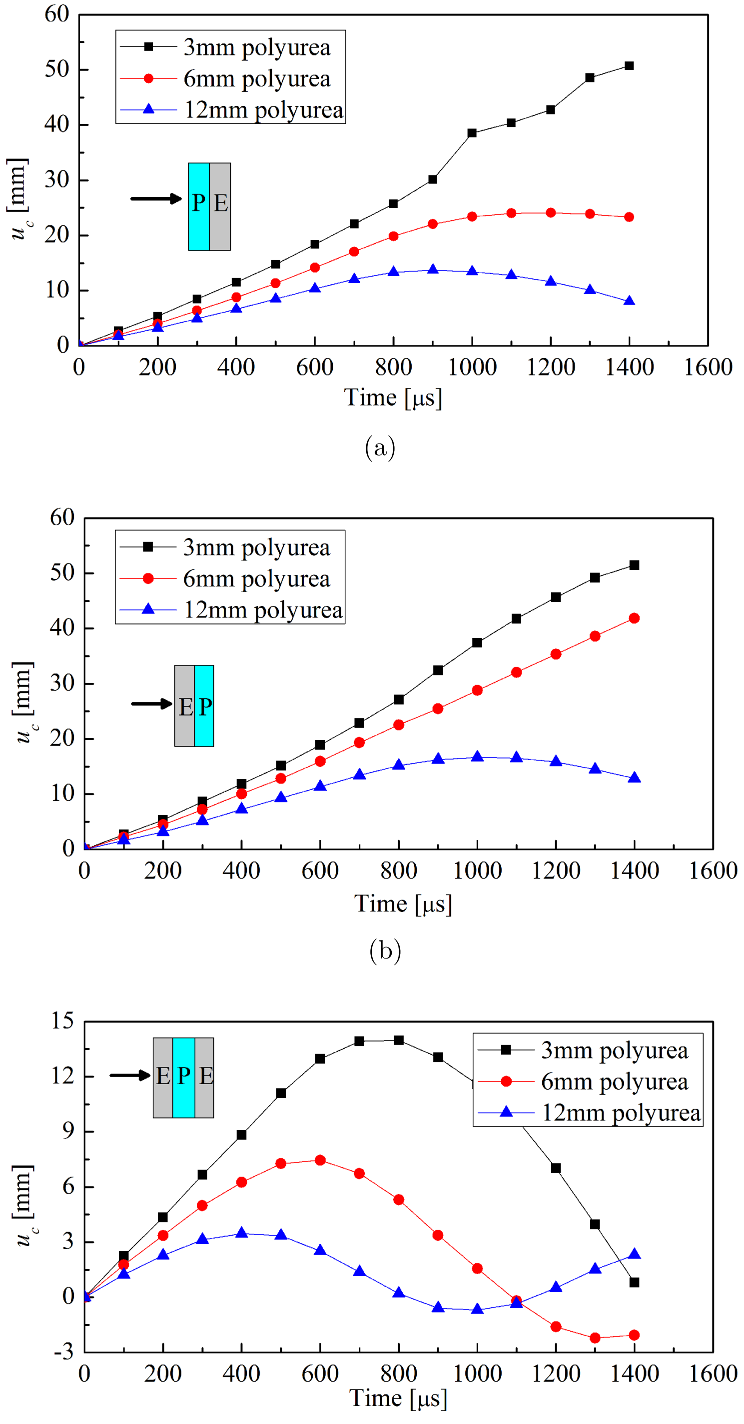

(a)

(b)

(c)

Figure 9: Effect of polyurea thickness on the evolution of center-point displacement in (a) PE-configuration, (b) EP-configuration, and, (c) EPE-configuration.

Polyurea was modeled using a temperature and pressure dependent viscoelastic constitutive model.

In the simulation findings: Strain rate hardening and temperature had limited influence on the structural deformation and the damage accumulation of the EVE composite panels subjected to blast at the amplitudes investigated in this study. Among the tree configurations, the numerical results confirmed that the sandwich configuration (EPE) exhibited better blast mitigation effect compared to the other two configurations (i.e., EP and PE). The blast mitigation effect of polyurea was enhanced by increasing the thickness and through confinement of the polyurea layer.

In this study, we focused our attention to relatively low blast amplitudes, in which through thickness Hugoniot effects and the wave reflection due to microstructural heterogeneities played a negligible role in the overall dynamic and failure responses. When the rate and the amplitude of applied loads are high enough, the effect wave dispersion becomes significant, and the structural dynamics and failure therefore may not be accurately captured by the explicit finite element model with Eq. 1. This sheds light on the research in the next chapters focusing on the wave propagation with strong wave dispersions in composite structures.

CHAPTER 3

MULTISCALE MODELING OF ONE DIMENSIONAL WAVE PROPAGATION IN VISCOELASTIC COMPOSITE STRUCTURES

1 Introduction

In the previous chapter, we have concluded that viscoelastic material (e.g. polyurea) exhibits a good mitigation effect on blast. The wave interaction and dispersion within viscoelastic composites is of great interest especially under high frequency waves. When wave is propagating in viscoelastic composite structures, the micro-heterogeneity induced wave dispersion and the viscoelasticity induced material dissipation coexist in the same domain, and both of the two effects are able to attenuate wave propagation. Furthermore, by taking advantage of the two *attenuating mechanisms*, it is possible to design a viscoelastic material based composite material with favorable mitigation effects against blast and other acoustic loadings. In this chapter, we start our investigation with the one-dimensional wave propagation in a viscoelastic-elastic composite bar structure. This analysis would elucidate our thoughts, and more complicated problems are going to be addressed in the next few chapters.

There is some, but still scarce, literature on modeling the dynamic behavior of dispersive viscoelastic composites. Chin-Teh [20] investigated the propagation of transient cylindrical shear waves in functionally graded viscoelastic bodies, in which the creep function varies along the radial direction. Wave propagation was modeled using the theory of propagating surfaces of discontinuities. Nayfeh [49] used a discrete lattice model to simulate the transient response of periodic, semi-infinite, elasto-viscoelastic composites. The dispersive solution was obtained by resolving the characteristic equations for the lattice model in the Laplace domain and subsequently transforming the solution to the time domain. Ting [73] carried out an investigation of a semi-infinite periodic layered composite where two viscoelastic materials are alternately positioned. The Laplace transform and asymptotic expansion of the relaxation modulus are used to achieve the dispersive solution. Mukherjee and Lee [47] conducted an analysis of the dispersion and mode shapes for free vibrations in infinite laminated media. The complex modulus formulation was employed to linearize the governing differential equations. A finite difference discretization and quasi periodic boundary conditions were used to solve the complex eigenvalue problem. More recently, plane harmonic waves in unbounded periodic viscoelastic composite materials were investigated by Naciri et al. [48]. The complex modulus function based governing equations were solved using the finite element method to investigate the relationship between damping and dispersion. Abu-Alshaikh et al. [2] considered two dimensional transient waves propagating in an N-layer viscoelastic medium idealized by a two-term Prony series. The governing hyperbolic equations in the Fourier domain were transformed to canonical equations by the method of characteristics and the solutions were obtained using step-by-step integration. Tsai and Prakash [74] investigated the decay in the elastic precursor and late time dispersion of weak shock waves in layered composites based on the Laplace transform associated with Floquet's theorem. Jiangong [40] idealized the response of shear waves with the Kelvin-Voigt model in functionally graded viscoelastic plates. The dispersive solution was obtained by approximating the response fields using a Legendre orthogonal polynomial series.

Despite the seminal contributions on modeling and characterization of the dynamic response of viscoelastic heterogeneous materials, modeling the effect of microstructure induced dispersion on the dissipative characteristics of viscous composites, a key fundamental knowledge for devising tailored microstructures for impact and blast mitigation, remains to be identified. In this chapter, we propose a one-dimensional nonlocal homogenization model for the wave dispersion in a bi-material structure. The semi-analytical solution is sought in the Laplace domain where com-

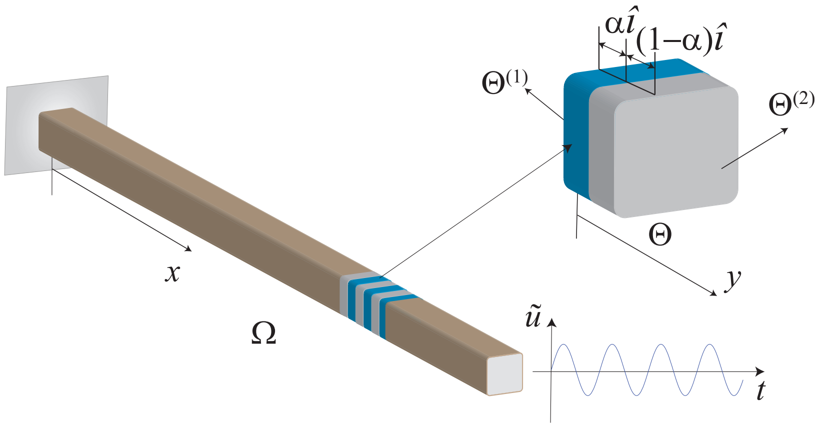

Figure 10: Problems at macroscale and microscale.

plex wave fields are solved.

2 Problem Setting

Consider a one-dimensional bimaterial heterogeneous body as illustrated in Fig. 10. The domain of the body, $\Omega = [0, L]$ is formed by the repetition of a locally periodic microstructure, Θ. The size of the material microstructure is taken to be small compared to the overall size of the macroscopic domain. Denoting x and y as the position coordinates at the scales of the macro- and microstructures, respectively, the two scales are related by a small scaling parameter: $y = x/\zeta$; where, $0 < \zeta \ll 1$ is the ratio between the characteristic size of the microstructure and the length of the traveling waves along the heterogeneous body.

Let $f^\zeta(x,t)$ be an arbitrary response field, which oscillates in space due to fluctuations induced by the material heterogeneity. We consider the following two scale decomposition of the original single position coordinate:

$$f^\zeta(x,t) = f(x, y(x), t) \tag{27}$$

where, superscript ζ indicates the dependence of the response field on the microstructural heterogeneity; and, t denotes time. The spatial derivative of f^{ζ} is computed by the chain rule as:

$$f^{\zeta}{}_{,x}(x,t) = f_{,x}(x,y,t) + \frac{1}{\zeta} f_{,y}(x,y,t) \tag{28}$$

where, a subscript followed by a comma denotes differentiation, repeated subscripts denotes higher order differentiation. The response fields are taken to be spatially periodic throughout the deformation process:

$$f(x,y,t) = f(x,y+\hat{l},t); \quad \forall x \in \Omega \tag{29}$$

in which, $\hat{l}$ denotes the period of the microstructure in the stretched coordinate system, y (Fig. 10).

2.1 Governing Equations in the Time Domain

In the time domain, the deformation response of the heterogeneous body subjected to dynamic loading conditions is governed by the momentum balance equation in the form:

$$\sigma^{\zeta}_{,x}(x,t) = \rho^{\zeta}(x) u^{\zeta}_{,tt}(x,t) \tag{30}$$

in which, σ^{ζ} and u^{ζ} are the stress and displacement fields, respectively; and, ρ^{ζ} denotes density. A generalized viscoelastic model described by the Duhamel's integral is employed to provide the constitutive response of the material constituents:

$$\sigma^{\zeta}(x,t) = \int_0^t g^{\zeta}(x,t-\tau)\epsilon^{\zeta}_{,\tau}(x,\tau)d\tau \tag{31}$$

where, g^{ζ} is the modulus function; and, ϵ^{ζ} denotes the strain field, assuming small strain kinematics:

$$\epsilon^{\zeta}(x,t) = u^{\zeta}_{,x}(x,t) \tag{32}$$

The dynamic loads are imparted on the heterogeneous body based on prescribed displacements along the boundaries of the domain. We consider the following initial and boundary conditions:

$$u^\zeta(x,0) = u^0(x); \qquad v^\zeta(x,0) = v^0(x) \tag{33}$$

$$u^\zeta(0,t) = 0; \qquad u^\zeta(L,t) = \tilde{u}(t) \tag{34}$$

in which, L is the length of the heterogeneous body; $v^\zeta = u^\zeta_{,t}$ the velocity field; and, u^0 , v^0 and $\tilde{u}$ are prescribed initial and boundary data.

2.2 Governing Equations in the Laplace Domain

The particular forms of the generalized viscoelastic constitutive model and the momentum balance equation permit a simpler description of the governing boundary value problem in the Laplace domain. In this section, we introduce the key characteristics of the Laplace transform employed in the formulation and recast the governing equations in the Laplace domain.

The Laplace transform of an arbitrary, real valued, time varying function, $f \in \mathbb{R}$, is defined as:

$$\bar{f}(s) \equiv \mathscr{L}(f(t)) = \int_0^\infty e^{-st} f(t) dt \tag{35}$$

where, the Laplace argument, s and the Laplace transform, $\bar{f}$, are complex valued (i.e., $s \in \mathbb{C}$ and $\bar{f} := \mathbb{C} \to \mathbb{C}$). Overbar on a response function indicates the Laplace transform, and the representation of a function or an equation in the Laplace domain is referred to as *associated* function or equation throughout the remainder of this chapter. The derivative rule for the Laplace transform is given as:

$$\mathscr{L}(f\underbrace{_{,tt\ldots t}}_{n \text{ times}}(t)) = s^n \bar{f}(s) - s^{n-1} f(0) - \ldots - f\underbrace{_{,tt\ldots t}}_{n-1 \text{ times}}(0) \tag{36}$$

and the convolution integral rule is given as:

$$\mathscr{L}\left(\int_0^t f_1(t-\xi)f_2(\xi)d\xi\right) = \mathscr{L}\left(\int_0^t f_1(\xi)f_2(t-\xi)d\xi\right) = \mathscr{L}(f_1)\mathscr{L}(f_2) \tag{37}$$

Considering a statically undeformed initial condition (i.e., $u^0(x) = v^0(x) = 0$), taking the Laplace transform of the momentum balance equation (Eq. 111) and employing the derivative rule for the Laplace transform (Eq. 198) yield the associated momentum balance equation:

$$\bar{\sigma}^{\zeta}_{,x}(x,s) = \rho^{\zeta}(x)s^2\bar{u}^{\zeta}(x,s) \tag{38}$$

Applying the convolution integral rule (Eq. 37) to the constitutive equation of the viscoelastic constituents (Eq. 31) and using Eq. 198 yield the associated constitutive law:

$$\bar{\sigma}^{\zeta}(x,s) = E^{\zeta}(x,s)\bar{\epsilon}^{\zeta}(x,s) \tag{39}$$

in which, the associated modulus function in the Laplace domain, E^{ζ}, is related to the modulus function, g^{ζ} as:

$$E^{\zeta}(x,s) = s\mathscr{L}\left(g^{\zeta}(x,t)\right) \tag{40}$$

Taking the Laplace transform of the boundary conditions yields the associated boundary conditions:

$$\bar{u}^{\zeta}(0,s) = 0; \quad \bar{u}^{\zeta}(L,s) = \hat{u}(s) \tag{41}$$

in which, $\hat{u}$ is the Laplace transform of the known boundary data, $\tilde{u}$. The governing equations of the dynamic response of the heterogeneous body defined in the Laplace domain is summarized in Box 1.

Given ρ^{ζ}, E^{ζ}, and $\hat{u}$; find $\bar{u}^{\zeta} \in \mathbb{C}$ such that in $x \in \Omega$ and $s \in \mathbb{C}$

Momentum balance: $\bar{\sigma}^{\zeta}_{,x}(x,s) = \rho^{\zeta}(x) s^2 \bar{u}^{\zeta}(x,s)$

Kinematics equation: $\bar{\epsilon}^{\zeta}(x,s) = \bar{u}^{\zeta}_{,x}(x,s)$

Constitutive equation: $\bar{\sigma}^{\zeta}(x,s) = E^{\zeta}(x,s)\bar{u}^{\zeta}_{,x}(x,s); \quad E^{\zeta}(x,s) = s\mathscr{L}\left(g^{\zeta}(x,t)\right)$

Boundary conditions $\bar{u}^{\zeta}(0,s) = 0; \quad \bar{u}^{\zeta}(L,s) = \hat{u}(s)$

Box 1: Governing boundary value problem in the Laplace domain.

The density and modulus are taken to vary as a function of the microscale coordinates only. For a bimaterial microstructure:

$$E^{\zeta} = E(y,s) \quad = \quad \begin{cases} E_1(s) \text{ if } y \in \Theta^{(1)} \\ E_2(s) \text{ if } y \in \Theta^{(2)} \end{cases} \tag{42}$$

$$\rho^{\zeta} = \rho(y) \quad = \quad \begin{cases} \rho_1 \text{ if } y \in \Theta^{(1)} \\ \rho_2 \text{ if } y \in \Theta^{(2)} \end{cases} \tag{43}$$

where, $\Theta^{(1)}$ and $\Theta^{(2)}$ are the domains of phases 1 and 2, respectively, such that $\Theta = \Theta^{(1)} \cup \Theta^{(2)}$; and, $\{E_1, \rho_1\}$ and $\{E_2, \rho_2\}$ are the material parameters defining the corresponding phases.

3 Nonlocal Homogenization

In this section, a nonlocal homogenization model is devised for the dynamic response of viscoelastic bimaterial composites by applying the mathematical homogenization theory with multiple spatial scales on the governing equations defined in the Laplace domain. The derivation follows the procedure originally proposed by Fish et al. [31], who devised a nonlocal homogenization model for linear elastic bimaterial composites by employing the mathematical homogenization theory in the time domain.

We start by approximating displacement based on the asymptotic expansion of the form:

$$u^{\zeta}(x,t) \equiv u(x,y,t) = u_0(x,t) + \zeta u_1(x,y,t) + \zeta^2 u_2(x,y,t) + \zeta^3 u_3(x,y,t) + O(\zeta^4) \quad (44)$$

where, u_0 denotes the macroscopic displacement field and is independent of the microstructure; and, u_i are spatially oscillatory high-order displacement fields. By linearity of the Laplace transform, the associated displacement field is also expressed in terms of the asymptotic series:

$$\bar{u}(x,y,s) = \bar{u}_0(x,s) + \zeta \bar{u}_1(x,y,s) + \zeta^2 \bar{u}_2(x,y,s) + \zeta^3 \bar{u}_3(x,y,s) + O(\zeta^4) \qquad (45)$$

Substituting Eq. 45 into the associated constitutive law (Eq. 39), the stress-strain relationships at any order are obtained as:

$$O(\zeta^i): \quad \bar{\sigma}_i\,(x,y,s) = E(y,s)(\bar{u}_{i,x} + \bar{u}_{i+1,y}); \quad i = 0, 1, \ldots \qquad (46)$$

Substituting Eq. (45) and the constitutive equations at various orders (Eq. 46) into the associated momentum balance equation (Eq. 38), the momentum balance equations of orders $O(\zeta^{-1})$ to $O(\zeta^2)$ are expressed as:

$$O(\zeta^{-1}): \qquad [E(y,s)(\bar{u}_{0,x} + \bar{u}_{1,y})]_{,y} = 0 \qquad (47)$$

$$O(1): \quad \rho(y)\bar{u}_0 s^2 - [E(y,s)(\bar{u}_{0,x} + \bar{u}_{1,y})]_{,x} - [E(y,s)(\bar{u}_{1,x} + \bar{u}_{2,y})]_{,y} = 0 \qquad (48)$$

$$O(\zeta): \quad \rho(y)\bar{u}_1 s^2 - [E(y,s)(\bar{u}_{1,x} + \bar{u}_{2,y})]_{,x} - [E(y,s)(\bar{u}_{2,x} + \bar{u}_{3,y})]_{,y} = 0 \qquad (49)$$

$$O(\zeta^2): \quad \rho(y)\bar{u}_2 s^2 - [E(y,s)(\bar{u}_{2,x} + \bar{u}_{3,y})]_{,x} - [E(y,s)(\bar{u}_{3,x} + \bar{u}_{4,y})]_{,y} = 0 \qquad (50)$$

Considering the balance equations at the lower two orders (Eqs. 47 and 48) leads to the classical homogenization model [e.g. 54]. The classical homogenization model is local in character and valid only when displacement wavelengths are large enough that the wave reflections along the bimaterial interfaces are negligible. The $O(\zeta)$ and $O(\zeta^2)$ balance equations introduce high order terms in the resulting homogenized equations, leading to a nonlocal homogenization model that can account for the dispersion induced by wave reflections at material microstructure boundaries.

Consider the $\mathrm{O}(\zeta^{-1})$ associated boundary value problem (Eq. 47). By linearity, the first order microscale associated displacement field, $\bar{u}_1$, is expressed using the following decomposition:

$$\bar{u}_1(x, y, s) = \bar{U}_1(x, s) + H(y, s)\bar{u}_{0,x}(x, s) \tag{51}$$

where, H denotes the first order microscopic influence function providing the oscillatory component of $\bar{u}_1$, whereas $\bar{U}_1$ denotes the macroscopic contribution of $\bar{u}_1$. Applying Eq. 51 to Eq. 47, a linear equilibrium equation for the first order microscopic influence function is obtained:

$$\left\{E(y, s)(1 + H_{,y})\right\}_{,y} = 0 \tag{52}$$

Equation 52 is evaluated by imposing the periodicity, continuity and normality conditions. The periodicity of the influence function follows from the periodicity of the displacement field:

$$H(y = 0, s) = H(y = \hat{l}, s); \quad \bar{\sigma}_0(x, y = 0, s) = \bar{\sigma}_0(x, y = \hat{l}, s) \tag{53}$$

in which, $\hat{l} = l/\zeta$; and, l is the physical length of the microstructure. The continuity of the microscale response fields across the bimaterial interfaces are ensured by imposing the following constraints:

$$\lim_{\nu\to 0} H(y=\alpha\hat{l}+\nu^+,s)-H(y=\alpha\hat{l}-\nu^-,s)=0 \tag{54}$$

$$\lim_{\nu\to 0} \bar{\sigma}_0(x,y=\alpha\hat{l}+\nu^+,s)-\bar{\sigma}_0(x,y=\alpha\hat{l}-\nu^-,s)=0 \tag{55}$$

where, $0\leq\alpha\leq 1$ is the volume fraction of phase 1 in the bimaterial microstructure as shown in Fig. 10. The uniqueness of the influence function is ensured by imposing the normality condition on the microscale associated displacement field, $\bar{u}_1$:

$$\langle \bar{u}_1(x,y,s)\rangle = \bar{U}_1(x,s)\rightarrow\langle H(y,s)\rangle = 0 \tag{56}$$

where, MacCauley brackets, $\langle\cdot\rangle$, denote the spatial averaging over the microstructure:

$$\langle f\rangle = \frac{1}{|\Theta|}\int_{\Theta} f(x,y,s)dy \tag{57}$$

where, $|\cdot|$ is the size of the microstructural domain (i.e., $|\Theta|=\hat{l}$). Considering the constraints in Eqs. 53-56, the influence function is evaluated in a closed form as follows,

$$H(y,s)=\begin{cases}\dfrac{(1-\alpha)(E_2(s)-E_1(s))}{(1-\alpha)E_1(s)+\alpha E_2(s)}\left(y-\dfrac{\alpha\hat{l}}{2}\right); & y\in\Theta^{(1)}\\[2ex] \dfrac{\alpha(E_1(s)-E_2(s))}{(1-\alpha)E_1(s)+\alpha E_2(s)}\left(y-\dfrac{(1+\alpha)\hat{l}}{2}\right); & y\in\Theta^{(2)}\end{cases} \tag{58}$$

The $O(1)$ homogenized equilibrium equation is obtained by applying the averaging operator (Eq. 57) to the associated balance equation (Eq. 48) . Considering the periodicity of the first order associated microscopic stress, $\bar{\sigma}_1$ yields:

$$\rho_0\bar{u}_0 s^2 - E_0(s)\bar{u}_{0,xx}=0 \tag{59}$$

where, ρ_0 and $E_0(s)$ denote the homogenized density and homogenized associated modulus function, respectively:

$$\rho_0 \equiv \langle \rho \rangle = \alpha\rho_1 + (1-\alpha)\rho_2 \tag{60}$$

$$E_0(s) = \langle E(y,s)(1 + H_{,y}) \rangle = \frac{E_1(s)E_2(s)}{(1-\alpha)E_1(s) + \alpha E_2(s)} \tag{61}$$

Next, we consider the $O(1)$ associated momentum balance equation (Eq. 48). Substituting Eqs. 51 and 59 into Eq. 48 yields:

$$\left\{E(y,s)(\bar{u}_{2,y} + \bar{U}_{1,x} + H\bar{u}_{0,xx})\right\}_{,y} = \left\{(\theta(y) - 1)\, E_0\right\} \bar{u}_{0,xx} \tag{62}$$

where, $\theta(y) = \rho(y)/\rho_0$. By linearity, the second order microscale associated displacement field, $\bar{u}_2$ is expressed as:

$$\bar{u}_2(x,y,s) = \bar{U}_2(x,s) + H(y,s)\bar{U}_{1,x}(x,s) + P(y,s)\bar{u}_{0,xx}(x,s) \tag{63}$$

in which, $P(y,s)$ is the second order microscale influence function. Considering the periodicity, continuity and normality constraints, P is uniquely evaluated by Eq. 62 in closed form. Employing the closed form expression for the second order microscale influence function and considering the periodicity of the second order stress field, $\bar{\sigma}_2$, the $O(\zeta)$ homogenized momentum balance equation is obtained by applying the averaging operator to Eq. 49:

$$\rho_0 \bar{U}_1 s^2 - E_0 \bar{U}_{1,xx} = 0 \tag{64}$$

The third order associated microscale displacement field, $\bar{u}_3$ is determined using the $O(\zeta)$ momentum balance equation (Eq. 49). Decompositions of the lower order microscale displacement fields (Eqs. 51 and 63) and the homogenized balance equations (Eqs. 59 and 64) at $O(1)$ and $O(\zeta)$ are substituted into Eq. 49 to yield:

$$\begin{aligned}&\left\{E(y,s)(\bar{u}_{3,y}+\bar{U}_{2,x}+H(y,s)\bar{U}_{1,xx}+P(y,s)\bar{u}_{0,xxx})\right\}_{,y}\\&\quad=\left\{\theta(y)E_0(s)H(y,s)-E(y,s)(H+P_{,y})\right\}\bar{u}_{0,xxx}+\left\{(\theta(y)-1)E_0(s)\right\}\bar{U}_{1,xx}\end{aligned} \tag{65}$$

We consider the following form for the third order associated microscale displacement field:

$$\bar{u}_3(x,y,s)=\bar{U}_3(x,s)+H(y,s)\bar{U}_{2,x}+P(y,s)\bar{U}_{1,xx}+Q(y,s)\bar{u}_{0,xxx} \tag{66}$$

where, $Q(y,s)$ is the third order microscale influence function. Analogous to the evaluation of the lower order influence functions, Q is uniquely determined from the $O(\zeta)$ momentum balance equation provided that the periodicity, continuity and normality conditions are imposed.

The $O(\zeta^2)$ homogenized momentum balance equation is obtained by applying the averaging operator to Eq. 50 and utilizing the expressions of $P(y,s)$ and $Q(y,s)$:

$$\rho_0\bar{U}_2s^2-E_0\bar{U}_{2,xx}=\frac{1}{\zeta^2}E_d\bar{u}_{0,xxxx} \tag{67}$$

where,

$$E_d(s)=\frac{[\alpha(1-\alpha)]^2(E_1\rho_1-E_2\rho_2)^2E_0l^2}{12\rho_0^2[(1-\alpha)E_1+\alpha E_2]^2} \tag{68}$$

Consider the average associated displacement field up to $O(\zeta^3)$:

$$\bar{U}(x,s)=\langle\bar{u}(x,y,s)\rangle=\bar{u}_0(x,s)+\zeta\bar{U}_1(x,s)+\zeta^2\bar{U}_2(x,s)+O(\zeta^3) \tag{69}$$

Summing the homogenized momentum balance equations at orders $O(1)$, $O(\zeta)$, and $O(\zeta^2)$ (Eqs. 59, 64 and 67), a governing homogenized balance equation for $\bar{U}$ is obtained in the following form:

$$\rho_0 s^2 \bar{U} - E_0 \bar{U}_{,xx} - E_d \bar{U}_{,xxxx} = 0 \tag{70}$$

It is important to note that the dispersive behavior is captured due to the presence of the last term in Eq. 70. The coefficient E_d introduces a characteristic length term (proportional to l^2). Introducing the dispersive term in the governing equation leads to a fourth order ordinary differential equation for the evaluation of associated homogenized displacement field, $\bar{U}(x, s)$ in the Laplace domain. This is in contrast to the time domain analysis by Fish et al. [31], which leads to a partial differential equation for the evaluation of the homogenized displacement field in the time domain. Since the governing equation is of the fourth order, the boundary conditions of the original initial boundary value problem provided in Eq. 41 is not sufficient to uniquely determine $\bar{U}$. We therefore consider two additional artificial boundary conditions:

$$\bar{U}_{,xx}(0, s) = 0, \quad \bar{U}_{,xxx}(L, s) = 0 \tag{71}$$

The resulting boundary value problem for the homogenized nonlocal response of the heterogeneous body subjected to the dynamic loads is summarized in Box 2.

Given ρ^ζ, E^ζ, and $\hat{u}$; find $\bar{U} \in \mathbb{C}$ such that in $x \in \Omega$ and $s \in \mathbb{C}$

Macro-homogenized equilibrium equation: $\rho_0 s^2 \bar{U} - E_0 \bar{U}_{,xx} - E_d \bar{U}_{,xxxx} = 0$

Essential boundary conditions: $\bar{U}(0, s) = 0 \quad \bar{U}(L, s) = \hat{u}(s)$

Additional boundary conditions: $\bar{U}_{,xx}(0, s) = 0 \quad \bar{U}_{,xxx}(L, s) = 0$

Box 2: Governing boundary value problem for the nonlocal homogenization model.

4 Solution Procedures

This section provides the analytical solutions of the nonlocal homogenization model, the classical homogenization model and the direct single scale boundary value problem. The computation of the dissipated energy density at a material point in the Laplace domain and the discrete Laplace transform method employed to describe the computed response fields in the time domain are presented.

4.1 Homogenization Models

The fourth order ordinary differential equation for the nonlocal homogenization model provided in Box 2 is analytically evaluated by considering the following form for the homogenized displacement field:

$$\bar{U}(x,s) = A(s)\sinh(\xi x) + B(s)\sinh(\eta x) \tag{72}$$

in which, the coefficients, A, B, ξ and η are obtained using the boundary conditions as:

$$A(s) = \frac{\hat{u}(s)\ \eta^3}{(\eta^3-\xi^3)\sinh(\xi L)}; \quad B(s) = \frac{\hat{u}(s)\ \xi^3}{(\xi^3-\eta^3)\sinh(\eta L)} \tag{73a}$$

$$\xi = \sqrt{\frac{-E_0 + \sqrt{E_0^2 + 4\rho_0 E_d s^2}}{2E_d}}; \quad \eta = \sqrt{\frac{-E_0 - \sqrt{E_0^2 + 4\rho_0 E_d s^2}}{2E_d}} \tag{73b}$$

When the homogenization is conducted up to order $O(\zeta)$, the formulation described in Section 3 leads to the classical homogenization model governed by the following second order ordinary differential equation:

$$\rho_0 s^2 \bar{u}_0 - E_0 \bar{u}_{0,xx} = 0 \tag{74}$$

Equation 74 is evaluated analytically using the following form:

$$\bar{u}_0(x,s) = C(s)\sinh(\varphi x) \tag{75}$$

The coefficients C and φ are obtained using the boundary conditions as follows:

$$C(s) = \frac{\hat{u}(s)}{\sinh(\varphi L)}; \quad \varphi = \frac{\operatorname{sign}(\operatorname{Re}(s))}{V_0}s; \quad V_0 = \sqrt{\frac{E_0}{\rho_0}} \tag{76}$$

where, V_0 is the frequency dependent homogenized velocity.

4.2 Original Governing Equations

Given ρ_i, E_i and $\hat{u}$; find $\bar{u}_i^n \in \mathbb{C}$ such that in $x \in \Omega$ and $s \in \mathbb{C}$

Equilibrium equation: $E_i \bar{u}_i^n{}_{,x_i x_i}(x_i,s) = \rho_i s^2 \bar{u}_i^n(x_i,s)$

Constitutive equation: $\bar{\sigma}_i^n(x_i,s) = E_i \bar{u}_i^n{}_{,x_i}(x_i,s)$

Interface continuities: $\bar{u}_1^n(\alpha l,s) = \bar{u}_2^n(0,s) \quad \bar{u}_2^n((1-\alpha)l,s) = \bar{u}_1^{n+1}(0,s)$

$\bar{\sigma}_1^n(\alpha l,s) = \bar{\sigma}_2^n(0,s) \quad \bar{\sigma}_2^n((1-\alpha)l,s) = \bar{\sigma}_1^{n+1}(0,s)$

Boundary conditions: $\bar{u}_1^1(0,s) = 0 \quad \bar{u}_2^N((1-\alpha)l,s) = \hat{u}(s)$

Box 3: Summary of the boundary value problem for the n^{th} microstructure

In this section, we derive the analytical solution of the original governing boundary value problem summarized in Box 3. The analytical solution derived in this section is employed as the reference solution in the numerical simulations that are discussed in the subsequent sections. The analytical solution is obtained by exploiting the governing equation in each microstructural phase along the heterogeneous body and enforcing continuity across each bimaterial interface.

We start by numbering microstructures along the bar. At the n^{th} microstructure ($n = 1, \ldots, N$, where N denotes total number of microstructures). We define two position coordinates x_1 and x_2 to parameterize the phase domains $\Omega_1^n = [0, \alpha l]$ and $\Omega_2^n = [0, (1-\alpha)l]$, respectively. The boundary value problem for each phase of the n^{th} microstructure including the continuity conditions for the displacements, $\bar{u}_i^n$ and stresses, $\bar{\sigma}_i^n$ at the interfaces are summarized in Box 3.

The general solution for the equilibrium equation in the boundary value problem is:

$$\bar{u}_i^n(x, s) = A_i^n \exp(\gamma_i x) + B_i^n \exp(-\gamma_i x) \tag{77}$$

with,

$$\gamma_i = \frac{\text{sign}(\text{Re}(s))}{V_i}; \quad V_i = \sqrt{\frac{E_i}{\rho_i}} \tag{78}$$

where, V_i is the complex wave velocity of phase i. The displacement and stress fields at the boundaries of each phase of the n^{th} microstructure read:

$$\bar{u}_1^n(0, s) = A_1^n + B_1^n, \qquad \bar{\sigma}_1^n(0, s) = A_1^n \eta_1 - B_1^n \eta_1 \tag{79}$$

$$\bar{u}_1^n(\alpha l, s) = A_1^n \xi_1 + B_1^n / \xi_1, \qquad \bar{\sigma}_1^n(\alpha l, s) = A_1^n \eta_1 \xi_1 - B_1^n \eta_1 / \xi_1 \tag{80}$$

$$\bar{u}_2^n(0, s) = A_2^n + B_2^n, \qquad \bar{\sigma}_2^n(0, s) = A_2^n \eta_2 - B_2^n \eta_2 \tag{81}$$

$$\bar{u}_2^n((1-\alpha)l, s) = A_2^n \xi_2 + B_2^n / \xi_2, \quad \bar{\sigma}_2^n((1-\alpha)l, s) = A_2^n \eta_2 \xi_2 - B_2^n \eta_2 / \xi_2 \tag{82}$$

where

$$\xi_1 = \exp\left(\gamma_1 \alpha l\right), \quad \xi_2 = \exp\left(\gamma_2 (1-\alpha) l\right) \tag{83}$$

$$\eta_1 = E_1 \gamma_1, \qquad \eta_2 = E_2 \gamma_2 \tag{84}$$

The boundary and continuity conditions of displacement and stress fields are used to determine the unknowns A_i^n and B_i^n:

Boundary conditions:

$$A_1^1 + B_1^1 = 0 \tag{85}$$

$$A_2^N \xi_2 + B_2^N / \xi_2 = \hat{u}(s) \tag{86}$$

Displacement continuities:
$$A_1^n \xi_1 + B_1^n / \xi_1 = A_2^n + B_2^n \tag{87}$$

$$A_2^n \xi_2 + B_2^n / \xi_2 = A_1^{n+1} + B_1^{n+1} \tag{88}$$

Stress continuities:
$$A_1^n \eta_1 \xi_1 - B_1^n \eta_1 / \xi_1 = A_2^n \eta_2 - B_2^n \eta_2 \tag{89}$$

$$A_2^n \eta_2 \xi_2 - B_2^n \eta_2 / \xi_2 = A_1^{n+1} \eta_1 - B_1^{n+1} \eta_1 \tag{90}$$

Equations 85 - 90 are expressed in the following matrix form:

$$\mathbf{M}\mathbf{X} = \mathbf{F} \tag{91}$$

where,

$$\mathbf{M}_{(4N \times 4N)} = \left[\begin{array}{cccccccccc}
1 & 1 & & & & & & & & \\
\xi_1 & 1/\xi_1 & -1 & -1 & & & 0 & & & \\
\eta_1 \xi_1 & -\eta_1/\xi_1 & -\eta_2 & \eta_2 & & & & & & \\
 & & \xi_2 & 1/\xi_2 & -1 & -1 & & & & \\
 & & \eta_2 \xi_2 & -\eta_2/\xi_2 & -\eta_1 & \eta_1 & & & & \\
 & & & & & \ddots & & & & \\
 & & & & & & \xi_1 & 1/\xi_1 & -1 & -1 \\
 & & 0 & & & \eta_1 \xi_1 & -\eta_1/\xi_1 & -\eta_2 & \eta_2 & \\
 & & & & & & & & \xi_2 & 1/\xi_2
\end{array} \right] \tag{92}$$

and,

$$\mathbf{F}_{(4N \times 1)} = [0, 0, \ldots, 0, \hat{u}(s)]^T \tag{93}$$

$$\mathbf{X}_{(4N \times 1)} = \left[A_1^1, B_1^1, A_2^1, B_2^1 \ldots, A_1^N, B_1^N, A_2^N, B_2^N \right]^T \tag{94}$$

Evaluating Eq. 91 provides the analytical (reference) solution. To compare the homogenized response computed by the homogenization models described in Section 4.1, we average the computed displacement field over each microstructure:

$$\bar{U}^n(s) = \frac{1}{l}\left(\int_0^{\alpha l} \bar{u}_1^n(x,s)dx + \int_0^{(1-\alpha)l} \bar{u}_2^n(x,s)dx\right) \tag{95}$$

Substituting equation 77 into 95:

$$\bar{U}^n(s) = \frac{1}{l}\left\{\left[A_1^n(\xi_1 - 1) - B_1^n\left(\frac{1}{\xi_1} - 1\right)\right]\frac{1}{\gamma_1} + \left[A_2^n(\xi_2 - 1) - B_2^n\left(\frac{1}{\xi_2} - 1\right)\right]\frac{1}{\gamma_2}\right\} \tag{96}$$

The dimension of the matrix $\mathbf{M}$ is $4N \times 4N$, which indicates that the computational cost of the reference solution increases as a function of the number of microstructures along the heterogeneous body. Computational time could therefore prohibit the evaluation of problems with a large number of microstructures. The analytical solution is only employed for the verification of the nonlocal homogenization model.

4.3 Inverse Laplace Transform

Since all the associated fields are derived in the Laplace domain, it is necessary to transform the response fields into the time domain. The numerical inverse Laplace Transform Method [17] based on Fast Fourier Transform and the ϵ-error algorithm [43] is used for transforming the response fields to the time domain. The inverse Laplace Transform is defined as,

$$f(t) = \frac{1}{2\pi i}\int_{c-i\infty}^{c+i\infty} F(s)e^{st}ds \tag{97}$$

with the assumptions that, $|f(t)| \leq Ke^{\beta t}$, where, K is real and positive; $t > 0$; and $\text{Re}(s) > \beta$. The numerical inverse Laplace transform is computed by N_v-term truncation, $\mathbf{F}_{(N_v)}$ of the transformed function values of $F(s)$, with the subscript N_v

denoting the dimension of the vector:

$$\mathbf{f}_{(M_v)} = \mathbf{C}_{(M_v)} \circ \left\{ 2\mathrm{Re} \left[\mathscr{E}(\mathrm{FFT}(\mathbf{F}_{(N_v)})) \right] - \mathbf{F}_{0(M_v)} \right\} \tag{98}$$

where, $\circ$ denotes the Hadamard product of matrices, e.g. the element-by-element product; $\mathscr{E}(\cdot)$ represents the ϵ-error algorithm, and $\mathbf{F}_{0(M_v)}$ is a M_v-element constant vector of c which can be computed as,

$$c = \beta - \frac{\Omega}{2\pi} \ln E_r \tag{99}$$

$$\Omega = \pi(1 - 1/M_v)/t_m \tag{100}$$

where $t_m = (M_v - 1)T_s$ and $M_v = N_v/2$. T_s is the sampling period in the time domain, E_r the desired relative error, and:

$$\mathbf{C}_{(M_v)}(k) = \frac{\Omega}{2\pi} \exp(ckT_s) \tag{101}$$

$$\mathbf{F}_{(N_v)}(n) = F(c - in\Omega) \quad n = 0, 1, \ldots, N_v - 1 \tag{102}$$

A more detailed description of the inverse Laplace transform method is presented by Brancik [17].

4.4 Dissipated Energy

The rate of dissipated energy density for the viscoelastic material model using the Duhamel's integral takes the following form [34]:

$$\dot{W}_d(x, y, t) = \int_0^t \int_0^t -\dot{g}(x, y, 2t - \tau_1 - \tau_2)\epsilon_{,\tau_1}(x, y, \tau_1)\epsilon_{,\tau_2}(x, y, \tau_2) d\tau_1 d\tau_2 \tag{103}$$

Equation 103 requires the computation of strain field in the time domain. In the Laplace domain, the associated macroscopic strain, $\bar{\epsilon}$ is related to the associated displacement field as follows,

$$\bar{\epsilon}(x, y, s) = \bar{u}_{,x} \tag{104}$$

Substituting Eq. 45 and the linearizions of $\bar{u}_1$, $\bar{u}_2$, and, $\bar{u}_3$ (i.e. Eqs. 51, 63) and 66, into Eq. 104, we can simplify the expression for associated strain:

$$\bar{\epsilon}(x, y, s) = (1 + H_{,y})\bar{U}_{,x} + \zeta(H + P_{,y})\bar{U}_{,xx} + \zeta^2(P + Q_{,y})\bar{U}_{,xxx} + O(\zeta^3) \tag{105}$$

in which, the localization functions, $(1 + H_{,y})$, $(H + P_{,y})$ and $(P + Q_{,y})$ are readily available through differentiation of the influence functions and provided in Appendix A. The reference solution provides the associated strain of phase i in microstructure Ω_i^n as:

$$\bar{\epsilon}_i^n(x_i, y, s) = A_i^n \gamma_i \exp(\gamma_i x_i) - B_i^n \gamma_i \exp(-\gamma_i x_i) \quad i = 1, 2 \text{ and } n = 1, 2, ..., N \tag{106}$$

The rate of dissipated energy density is evaluated by inverting the associated strain and substituting it into the real time domain using the numerical inverse Laplace transform.

5 Numerical Examples

A series of simulations have been conducted to assess the validity of the proposed nonlocal homogenization model and investigate the energy dissipation characteristics of a one-dimensional bi-material viscoelastic-elastic structure. The capabilities of the model is verified against the analytical solution of the original single scale boundary value problem and the classical local homogenization model.

The material moduli function that represents the material properties at the scale

Table 4: Viscoelastic material parameters for polyurea [5].

k_1 [MPa]	k_2 [MPa]	k_3 [MPa]	k_4 [MPa]	k_e [MPa]
37.8918	75.5328	161.0112	194.5216	44.8
q_1 [ms]	q_2 [ms]	q_3 [ms]	q_4 [ms]	ρ [kg/m^3]
463.4	0.06407	1.163×10^{-4}	7.321×10^{-7}	1070

of microstructure is modeled as:

$$g(y,t) = \begin{cases} E_1 & \text{if } y \in \Theta^{(1)} \\ k_e + \sum_{i=1}^{n} k_i e^{-t/q_i} & \text{if } y \in \Theta^{(2)} \end{cases} \tag{107}$$

where n is number of Prony series. In all cases below, the first phase is taken to be elastic, whereas the second phase is viscoelastic, modeled by a Prony series approximation. The viscoelastic material idealizes the response of the polyurea material. The material properties of polyurea is provided by Amirkhizi et al. [5] and summarized in Table 4. Applying the Laplace transform to the modulus function yields:

$$E(y,s) = \begin{cases} E_1 & \text{if } y \in \Theta^{(1)} \\ E_2(s) = k_e + \sum_{i=1}^{n} \frac{k_i s}{s + \frac{1}{q_i}} & \text{if } y \in \Theta^{(2)} \end{cases} \tag{108}$$

The dissipated energy computations are conducted by taking advantage of the Prony series approximation. The rate of dissipated energy at the viscoelastic phase is expressed as:

$$\dot{W}_d(x,t) = \sum_{i=1}^{\mathrm{n}} \frac{k_i}{q_i} \epsilon_d^i(x,t) \epsilon_d^i(x,t) \tag{109}$$

where,

$$\epsilon_d^i(x,t) = \int_0^t \exp\left(-(t-\tau)/q_i\right) \dot{\epsilon}\, d\tau \tag{110}$$

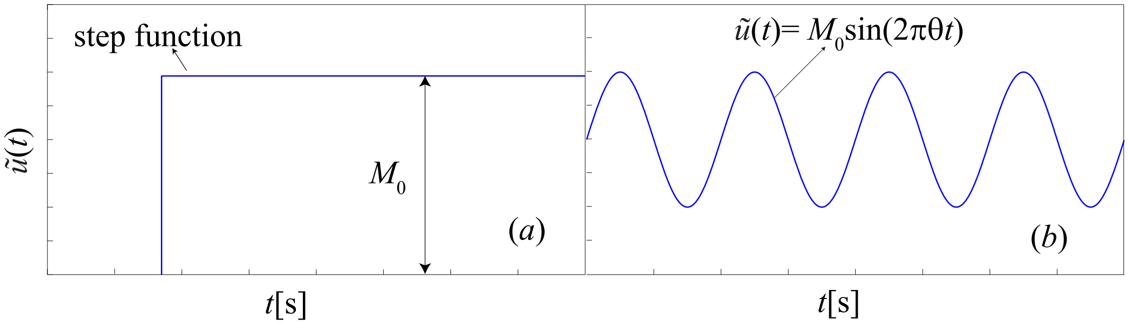

Figure 11: Applied boundary conditions.

5.1 Model Verification: Dispersion and Dissipation

In this section, we verify the capability of the nonlocal homogenization model (NHM) in capturing wave dispersion and dissipation in the underlying structure. The response of NHM is compared to the classical homogenization model (CHM) and the analytical solution of the reference model (AS). The ratio of the macroscopic and microscopic domain sizes (i.e., N) is set as 40. The modulus of the elastic phase (phase 1) is taken as 1 GPa, and the two phases have equal volume fractions (i.e., $\alpha = 0.5$).

First, we consider the response when the end of the bar is subjected to step loading with magnitude M_0 as illustrated Fig. 114a. We evaluate the response of the bars with four different density contrast in the microstructure (i.e., $\phi = \rho_1/\rho_2 = 1, 2, 5, 10$). The normalized displacement histories as a function of the normalized time (i.e., t/T where, T denotes the observation duration) are shown in Fig. 12 for the four density ratios as computed using NHM, CHM and the reference solutions. The displacement histories are recorded at $0.82L$ distance from the fixed end of the bar. The "cycles" observed in Fig. 12 are due to the repeated reflections of the wave at the fixed and loaded boundaries of the domain. In Figs. 12a-d, the distance between the displacement peak and trough at each cycle reduces, indicating progressive attenuation of the wave. At the asymptote of complete attenuation, the normalized displacement at the control point approaches 0.82. This corresponds to the uniform strain state induced by a quasi-statically applied unit displacement at the loaded end. At all density ratios, the results indicate good agreement between the nonlocal homogenization approach and the reference solution. Figures 12a-d illustrate that the wave dispersion increases with the density ratio in the microstructure. While the nonlocal model accurately accounts for the wave dispersion at high density ratios, the classical homogenization model fails to capture the wave dispersions. Yet, the dissipation patterns are accurately captured by CHM, which indicates that the attenuation induced by wave dispersion is relatively small. In other words, the dispersion induced attenuation can only be captured by taking account of the higher order derivative term in NHM, however the viscoelastic dissipation resulting from the viscoelastic modulus is included in both the NHM and CHM.

In the simulations displayed in Fig. 12, the density ratios of (i.e., $\phi = 1, 2, 5, 10$) are set by increasing the density of the elastic constituent, ρ_1, while keeping the density of the viscoelastic constituent, ρ_2, constant. The density of the homogenized constituent, ρ_0, in Eq. 60 therefore increases as ϕ is increased, leading to lower wave velocity of the homogenized domain and slower propagation. The effect of dispersion induced internal scattering on the propagation rate at high density ratios is relatively minor. This is because the CHM model is able to capture the slower propagation of the wave at high density ratios accurately, despite missing the dispersion effects.

Next, we investigate the response of the bar when subjected to sinusoidal loading as illustrated in Fig. 114b. The applied loadings is parameterized by the magnitude, M_0 and the frequency, θ. The density ratio, ϕ of the heterogeneous bar is set to 10. Figure 13 shows the normalized displacement history for identical heterogeneous bars vibrating at four different frequencies ($\theta = 10, 30, 50,$ and 70 Hz) recorded at $0.82L$ distance from the fixed end of the specimen. At relatively low frequency loading (e.g., $\theta = 10$ Hz), the classical and the nonlocal homogenization models capture the response reasonably accurately, with the exception of the phase shift and

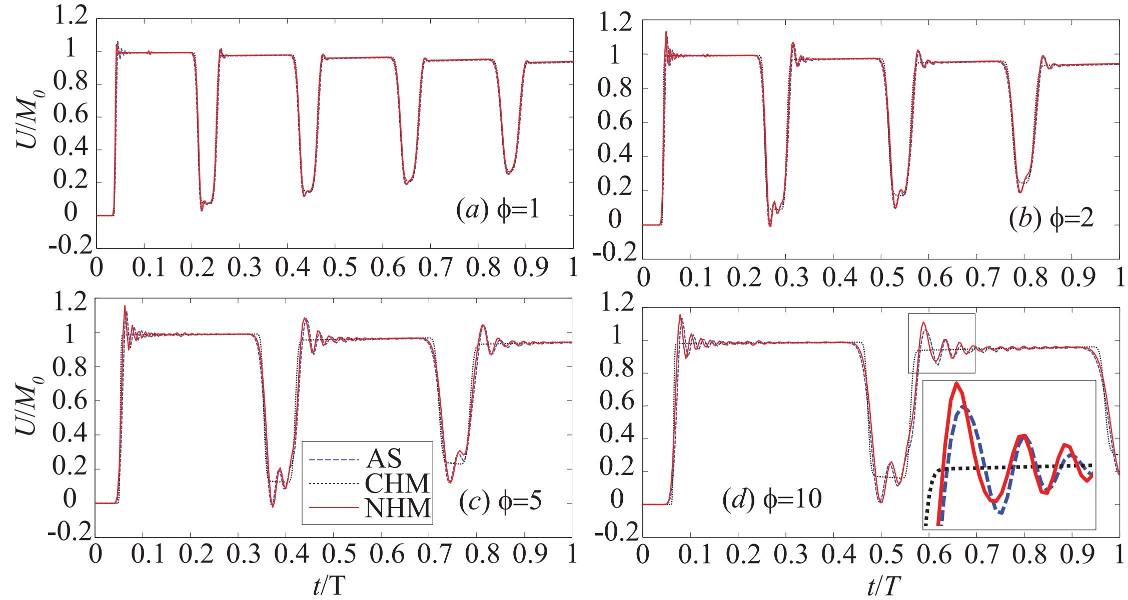

Figure 12: Displacement histories under different density ratios when subjected to step loading.

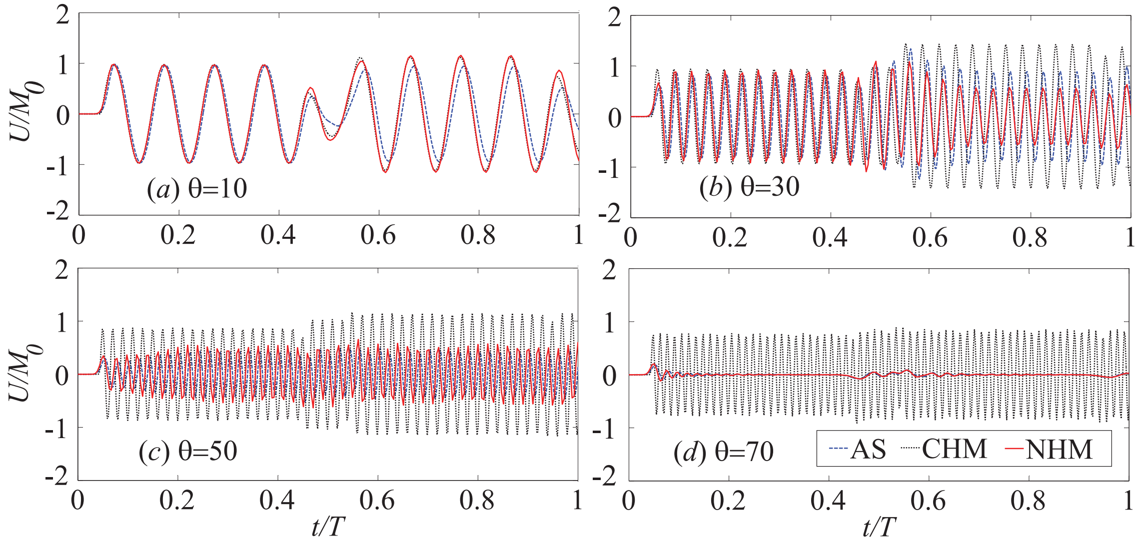

Figure 13: Displacement histories under different loading frequencies when subjected to sinusoidal loading.

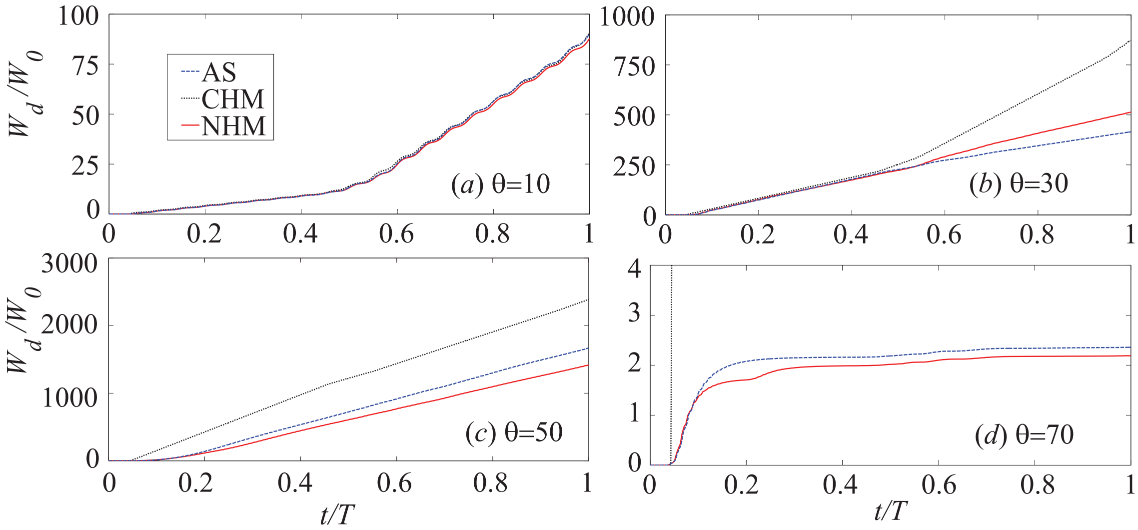

Figure 14: Dissipated energy density histories under different loading frequencies.

accompanying reduction in the peak amplitude originating from the wave reflections at the fixed end. At the higher frequency loadings ($\theta = 30$ and 50Hz), the attenuation due to heterogeneity induced wave dispersions becomes significantly more pronounced since the shorter wavelength events reflect at the bimaterial interfaces, dissipating energy in the viscous phase. At the highest frequency (i.e., $\theta = 70$ Hz), the wave dissipates within a short distance from the applied loading. CHM cannot predict such a attenuation phenomena as apparent in Fig. 13.

The dissipated energy analysis enhances the findings from the displacement results. The dissipated energy density is observed at the same place ($0.82L$ distance from the fixed end). The NHM and reference solutions are in good agreement, however the CHM solution shows discrepancy with the other two solutions, especially at higher loading frequencies. Specifically, the excessive over-prediction of the dissipated energy density when $\theta = 70$ indicates wave propagation at the observation point. In contrast, the other two solutions provide the opposite conclusions, i.e., wave propagation is forbidden since little dissipated energy or displacement is found at the observation point.

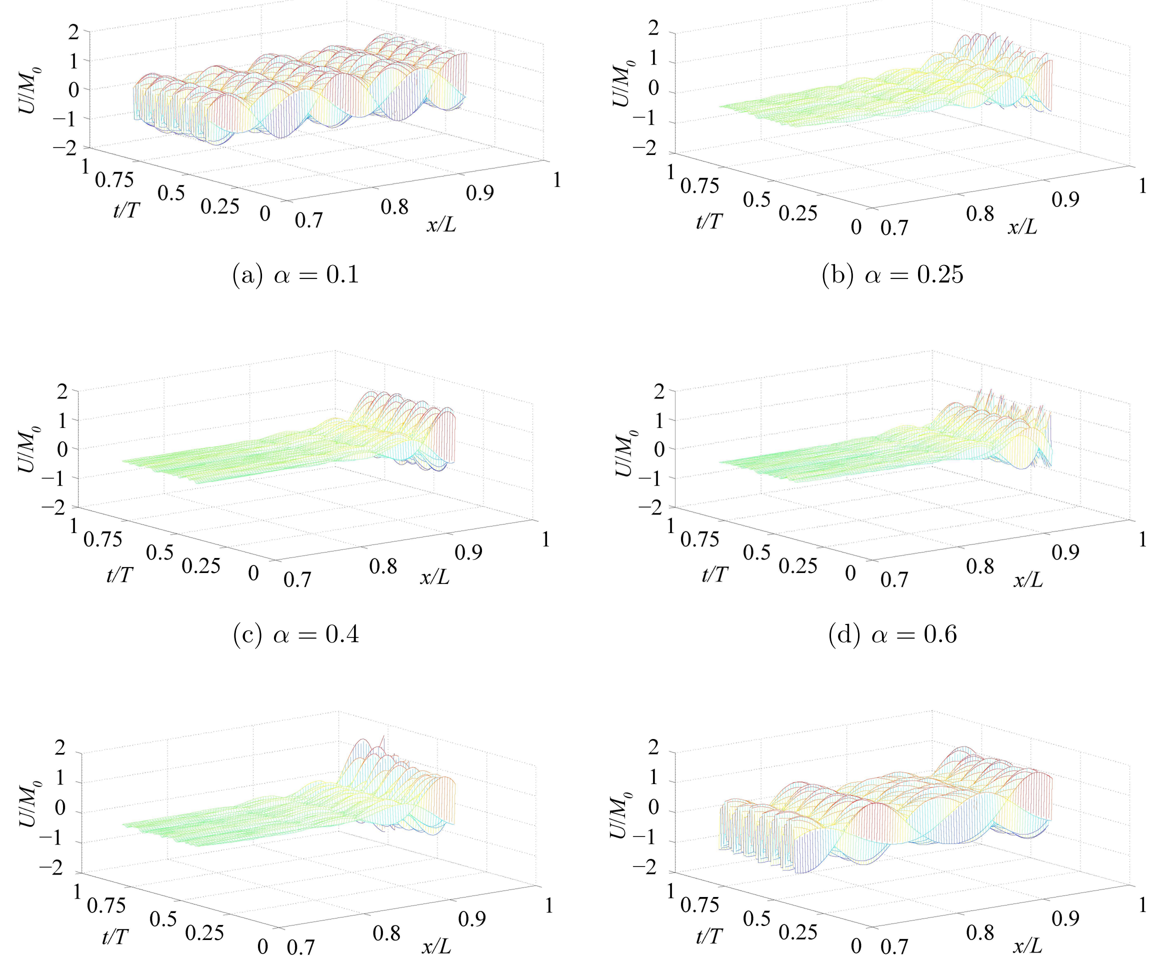

(a) $\alpha = 0.1$ (b) $\alpha = 0.25$

(c) $\alpha = 0.4$ (d) $\alpha = 0.6$

(e) $\alpha = 0.75$ (f) $\alpha = 0.9$

Figure 15: Macrostructural analysis of the displacements for different microstructures.

5.2 Microstructural Effects on Phononic Bands

In the frequency domain, the wave propagation exhibits band structures including passbands and stopbands. Band structures are due to the wave dispersion in heterogeneous microstructures. Wave propagation is active in passbands and prohibited in stopbands. Band structures were found in the electronic structures which exhibit photonic bandgaps (i.e., stopbands)[79, 80] and in the acoustic structures which exhibit phononic bandgaps. Phononic bands have been found in different materials

[41, 67, 75].

The previous results have shown the appearance of phononic bandgap in the current dispersive system. Next, we investigate the microstructural effects on band structures. A steel-polyurea composite bar is considered. The material properties of the viscoelastic polyurea phase are summarized in Table 4. The density and modulus of the elastic steel phase are set to $\rho_1 = 7847$ kg/m^3 and $E_1 = 200$ GPa, respectively. The bar is subjected to a sinusoidal loading with the loading frequency of $\theta = 80$ Hz. The ratio of the macroscopic and microscopic domain sizes is set as $N = 20$. The dynamic response of the composite is investigated for six microstructural configurations (α=0.1, 0.25, 0.4, 0.6, 0.75 and 0.9). The proposed nonlocal homogenization model is employed to predict structural responses.

Figure 15 displays the normalized displacement profiles as a function of time and position for the duration of the dynamic loading. When the microstructure consists largely of the polyurea or the steel phase (i.e., $\alpha = 0.1$ and $\alpha = 0.9$, respectively), wave propagation extends throughout the length of the bar. For intermediate configurations with comparable polyurea and steel volume fractions (i.e., $\alpha = 0.25, 0.4, 0.6$ and 0.7), the propagation attenuates within approximately a tenth of the bar, pointing to the occurrence of bandgap. Based on this observation, we can confirm that, band structures are able to be altered by changing microstructural properties.

6 Computational Efficiency

In addition to the favorable accuracy of the nonlocal homogenization model demonstrated above, it is computationally significantly more efficient compared to the reference simulation. While NHM employs a single equilibrium equation in the evaluation of the dynamics response, the reference model requires the solution of a $4N \times 4N$ system of equations leading to significant computational cost. For instance, when 500 microstructures are included in the problem (i.e., $N = 500$), the computational time required to solve the reference problem is three orders of magnitude larger than the nonlocal model. Such an analysis required approximately two minutes computation time for the nonlocal homogenization model using a single workstation, whereas several days were required to complete the same analysis based on the reference solution. This drawback makes using the analytical solution for simulating responses in structures having a large number of microstructures intractable, and the nonlocal homogenization is favorable compared to the CHM and the reference solution by providing accurate predictions at both scales while maintaining satisfactory time efficiency.

7 Conclusions

A nonlocal homogenization model is derived to account for the one-dimensional wave dispersion in bi-material viscoelastic-elastic structures. The homogenization model is based on the mathematical homogenization theory with multiple spatial scales applied in the Laplace domain. The high order equilibrium terms in the asymptotic expansion is incorporated to reveal the micro-heterogeneity induced wave dispersion.

An important finding in this chapter is that the viscoelastic-elastic bar exhibits the passband and stopband under different loading frequencies. This finding demonstrates the capability of microstructures on wave attenuation. In addition, this capability can be enhanced by optimizing microstructural properties. Since the numerical examples in this chapter are limited to one-dimensional wave propagation, and the nonlocal homogenization solution is of a semi-analytical form, the generality of microstructural influence on wave attenuation cannot be achieved. In the next chapters, attention will be focused on developing a numerical solution for wave propagation in multi-dimensional composite structures. In addition, microstructural influence on wave attenuation will be demonstrated with general problem definitions.

CHAPTER 4

MULTISCALE MODELING OF MULTI-DIMENSIONAL WAVE PROPAGATION IN ELASTIC COMPOSITE STRUCTURES

1 Introduction

Wave propagation exhibits much more complex dispersion patterns in multi-dimensional composite structures where analytical solutions usually cannot be derived due to the complexity of problem definitions. A computational model is therefore necessary for multi-dimensional wave propagation in composite structures.

The effects of micro-inertia and dispersion have been recently modeled using gradient enhancement [14], time-harmonic Bloch expansions [66], scale bridging through Hamilton's principle [77], and models based on Mindlin's theory [28, 35]. These approaches require the incorporation of high order strain and inertia gradient terms to the macroscopic equations of motion. The work in Chapter 3 provides us with the multiscale homogenization theory [10, 15, 38] applied in wave dispersion problems. In order to capture the dispersion effects, it is necessary to include higher order terms in the asymptotic expansions. Chen and Fish [19] recognized the presence of numerical instability for large time windows and proposed a space-time homogenization model that regularizes the long-time behavior in the presence of dispersion. A stable homogenization model that does not require multiple time scales was devised by Fish et al. [30], where higher order equilibrium terms were included in the formulation. This rigorous homogenization model is only valid for the dispersion due to modulus disparities in microstructures, and only in the presence of displacement boundary conditions. Bakhvalov and Eglit [12] applied the mathematical homogenization theory to study wave propagation in thin heterogeneous plates. Andrianov et al. [6] provided analytical solutions by incorporating the high order homogenization modeling to investigate the wave dispersion in composite rods and square lattice of cylindrical inclusions. The two latter investigations focused on specific microstructural topologies. Recently, Fish et al. [32] proposed a new dispersion formulation, where the micro-inertia effects are introduced based on an eigenstrain formulation. This formulation was generalized to account for nonlinear behavior. Andrianov et al. [7, 8] also addressed micro-inertia effects in nonlinear heterogeneous media using the homogenization method.

All the aforementioned models are able to capture the microstructural heterogeneity induced wave dispersion within the corresponding problem definitions. However, the revelation of band structures is also one of the requirements for the underlying computational model. This is because phononic band structures have been found in both simulations and experiments [41, 67, 75], and stopband is able to attenuate wave propagation effectively as discussed in Chapter 3. On the other hand, complex wavenumber needs to be incorporated in the acoustic wave equations to reveal bandgaps (i.e., stopbands) in phononic bands. A few computational models have been proposed to capture phononic bands. Suzuki and Yu [70] and Andrianov et al. [6] incorporated complex wavenumber in the Bloch-Floquet's wave theorem, and the calculated dispersion relation for certain periodic elastic structures indicated the appearance of stopband. However, the wave propagations are limited to certain strict problem definitions, e.g., one-dimensional wave, and with analytical solutions.

Based on the above discussion, there is not a computational model capable of accounting wave dispersion, phononic bands and multi-dimensional wave propagation altogether. Therefore, in this chapter, we focus on deriving a new computational model considering all these factors. We extend the high order homogenization model proposed by Fish et al. [30] to include complete microstructural disparities and traction boundary conditions. In addition, we solve the macroscopic problem using the hybrid Laplace transform-finite element method [18, 61] in order to involve complex wavenumber which is necessary for capturing phononic bands.

2 Problem Setting

Let $\Omega \in \mathbb{R}^{n_{\text{sd}}}$ denote the domain of a heterogeneous body subjected to dynamic loads as illustrated in Fig. 16 and n_{sd} is the number of space dimensions. The equation of motion for the body occupying Ω is:

$$\sigma^{\zeta}_{ij,j}(\mathbf{x},t) = \rho^{\zeta}(\mathbf{x})\ddot{u}^{\zeta}_{i}(\mathbf{x},t) \tag{111}$$

where $\boldsymbol{\sigma}^{\zeta}$ denotes the stress tensor, ρ^{ζ} the density, and $\mathbf{u}^{\zeta}$ the displacement. ζ represents the dependency of response fields on microstructural heterogeneities, i.e. response fields oscillate at wavelengths of the order of characteristic volume size. $\mathbf{x}$ denotes the position coordinate, and $t \in [0, t_0]$ the time variable, and t_0 is the end of observation period. Comma in the subscript denotes spatial derivative and overhead dot represents temporal derivative. The problem is formulated in Cartesian coordinate system using index notation following the Einstein convention (repeated indices indicate summation). Bold fonts are reserved for tensor and matrix/vector representations. The constitutive response of the heterogeneous body with elastic constituents is expressed as:

$$\sigma^{\zeta}_{ij}(\mathbf{x},t) = C^{\zeta}_{ijkl}(\mathbf{x})\epsilon^{\zeta}_{kl}(\mathbf{x},t) \tag{112}$$

where $\mathbf{C}^{\zeta}$ is the elastic modulus tensor, which is strongly elliptic and possesses major and minor symmetries, and $\boldsymbol{\epsilon}^{\zeta}$ the strain tensor. Under the assumption of small deformation:

$$\epsilon^{\zeta}_{ij}(\mathbf{x},t) = \frac{1}{2}\left(u^{\zeta}_{i,j}(\mathbf{x},t) + u^{\zeta}_{j,i}(\mathbf{x},t)\right) \tag{113}$$

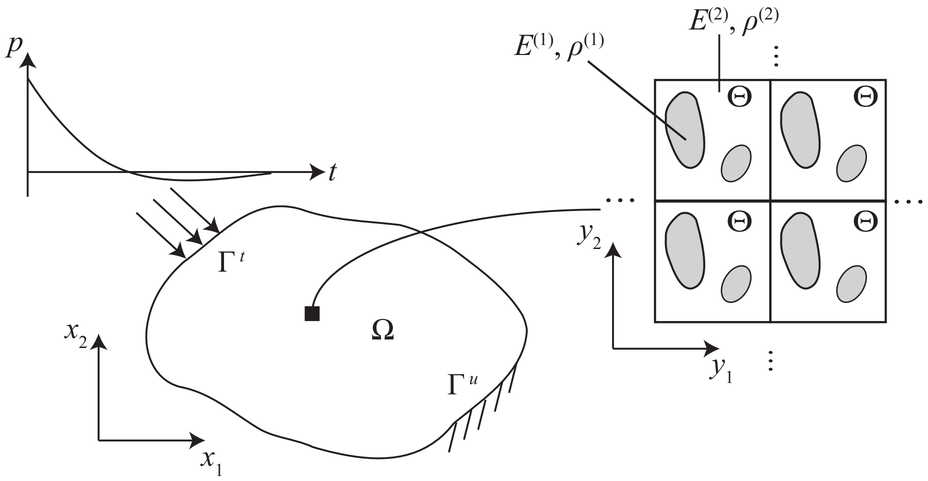

Figure 16: Schematic representation of the problem setting.

The oscillation of response fields due to microstructural heterogeneities is induced by the contrast of elastic moduli and densities of micro-constituents. Equations 111-113 are considered together with the following boundary conditions:

$$u_i^{\zeta}(\mathbf{x},t) = \bar{u}_i(\mathbf{x},t); \quad \mathbf{x} \in \Gamma^u \tag{114a}$$

$$\sigma_{ij}^{\zeta}(\mathbf{x},t)n_j = \bar{t}_i(\mathbf{x},t); \quad \mathbf{x} \in \Gamma^t \tag{114b}$$

in which $\mathbf{n}$ is the outward unit normal vector along the traction boundaries. $\bar{\mathbf{u}}$ and $\bar{\mathbf{t}}$ denote the prescribed displacement and traction data on Γ^u and Γ^t, respectively. The boundary conditions are defined such that $\Gamma \equiv \partial\Omega = \Gamma^u \cup \Gamma^t$; $\Gamma^u \cap \Gamma^t = \emptyset$. The initial conditions are:

$$u_i^{\zeta}(\mathbf{x},0) = \hat{u}_i(\mathbf{x}); \quad \mathbf{x} \in \Omega \tag{115a}$$

$$\dot{u}_i^{\zeta}(\mathbf{x},0) = \hat{v}_i(\mathbf{x}); \quad \mathbf{x} \in \Omega \tag{115b}$$

where $\hat{\mathbf{u}}$ and $\hat{\mathbf{v}}$ denote the initial displacement and velocity data, respectively.

In this work, the initial boundary value problem (IBVP) defined using Eqs. 111-115 is evaluated using the computational homogenization method with multiple spatial scales. The macroscale coordinate vector, $\mathbf{x}$, parameterizes the macroscopic domain, Ω, and the microscale (stretched) coordinate vector, $\mathbf{y}$, parameterizes the characteristic volume (e.g. representative volume or unit cell) denoted as Θ. $\mathbf{y}$ is related to the macroscale coordinate system, $\mathbf{x}$ as $\mathbf{y} = \mathbf{x}/\zeta$, where ζ is the scaling factor ($0 < \zeta < 1$) defined as the ratio between the size of the characteristic volume, Θ and the relevant shortest wavelength describing the homogenized response. An arbitrary response function, f^{ζ}, is expressed using the micro- and macroscopic coordinate vectors:

$$f^{\zeta}(\mathbf{x}) = f(\mathbf{x}, \mathbf{y}(\mathbf{x})) \tag{116}$$

The derivative of the response field is computed using the chain rule:

$$f^{\zeta}_{,x_i}(\mathbf{x}) = f_{,x_i}(\mathbf{x}, \mathbf{y}) + \frac{1}{\zeta} f_{,y_i}(\mathbf{x}, \mathbf{y}) \tag{117}$$

All response fields are assumed to be locally periodic over the characteristic volume throughout the deformation process:

$$f(\mathbf{x}, \mathbf{y}) = f(\mathbf{x}, \mathbf{y} + \mathbf{k}\hat{\mathbf{y}}) \tag{118}$$

where $\hat{\mathbf{y}}$ denotes the period of the microstructure; and $\mathbf{k}$ is a $n_{\mathrm{sd}} \times n_{\mathrm{sd}}$ diagonal matrix with integer components.

3 Mathematical Homogenization

In this section, the multiscale representations of the response functions are used along with the asymptotic analysis of the original IBVP defined by Eqs. 111–115 to formulate a high order computational homogenization model. The displacement field is approximated using an asymptotic expansion with respect to the scaling factor, ζ:

$$u_i^{\zeta}(\mathbf{x},t) = u_i(\mathbf{x},\mathbf{y},t) = u_i^0(\mathbf{x},t) + \zeta u_i^1(\mathbf{x},\mathbf{y},t) + \zeta^2 u_i^2(\mathbf{x},\mathbf{y},t) + \zeta^3 u_i^3(\mathbf{x},\mathbf{y},t) + O(\zeta^4) \tag{119}$$

where the leading order displacement $\mathbf{u}^0$ is a function of macroscopic coordinate only, while the high order displacements, $\mathbf{u}^{\alpha}$ ($\alpha = 1,2,3\ldots$), are functions of both the macro- and microscopic coordinates. Substituting Eq. 119 to Eq. 113, the strain tensor is expressed as:

$$\epsilon_{ij}(\mathbf{x},\mathbf{y},t) = \epsilon_{ij}^0(\mathbf{x},\mathbf{y},t) + \zeta\epsilon_{ij}^1(\mathbf{x},\mathbf{y},t) + \zeta^2\epsilon_{ij}^2(\mathbf{x},\mathbf{y},t) + O(\zeta^3) \tag{120}$$

where,

$$\epsilon_{ij}^{\alpha}(\mathbf{x},\mathbf{y},t) = e_{xij}(\mathbf{u}^{\alpha}) + e_{yij}(\mathbf{u}^{\alpha+1}); \quad \alpha = 0,1,2\ldots \tag{121}$$

$$e_{\xi ij}(\mathbf{u}^{\alpha}) = u^{\alpha}_{(i,\xi_j)} = 1/2\left(u^{\alpha}_{i,\xi_j} + u^{\alpha}_{j,\xi_i}\right); \quad \xi = x, y \tag{122}$$

Substituting Eq. 120 into Eq. 112, the stresses are expressed as:

$$\sigma_{ij}(\mathbf{x},\mathbf{y},t) = \sigma_{ij}^0(\mathbf{x},\mathbf{y},t) + \zeta\sigma_{ij}^1(\mathbf{x},\mathbf{y},t) + \zeta^2\sigma_{ij}^2(\mathbf{x},\mathbf{y},t) + O(\zeta^3) \tag{123}$$

where the stress components at each order of ζ are given as:

$$\sigma_{ij}^{\alpha}(\mathbf{x},\mathbf{y},t) = C_{ijkl}(\mathbf{y})\epsilon_{kl}^{\alpha}(\mathbf{x},\mathbf{y},t); \quad \alpha = 0,1,2,\ldots \tag{124}$$

Since microstructure is assumed to be periodic across the problem domain, the tensor of elastic moduli and the density depend on $\mathbf{y}$ only (i.e. $\mathbf{C}^{\zeta}(\mathbf{x}) = \mathbf{C}(\mathbf{y})$ and $\rho^{\zeta}(\mathbf{x}) = \rho(\mathbf{y})$). Substituting Eq. 123 into Eq. 111, the equations of motion at each order of ζ

are obtained:

$$O(\zeta^{-1}): \quad \sigma^0_{ij,y_j}(\mathbf{x},\mathbf{y},t) = 0 \tag{125a}$$

$$O(1): \quad \sigma^0_{ij,x_j}(\mathbf{x},\mathbf{y},t) + \sigma^1_{ij,y_j}(\mathbf{x},\mathbf{y},t) = \rho(\mathbf{y})\ddot{u}^0_i(\mathbf{x},t) \tag{125b}$$

$$O(\zeta): \quad \sigma^1_{ij,x_j}(\mathbf{x},\mathbf{y},t) + \sigma^2_{ij,y_j}(\mathbf{x},\mathbf{y},t) = \rho(\mathbf{y})\ddot{u}^1_i(\mathbf{x},\mathbf{y},t) \tag{125c}$$

$$O(\zeta^2): \quad \sigma^2_{ij,x_j}(\mathbf{x},\mathbf{y},t) + \sigma^3_{ij,y_j}(\mathbf{x},\mathbf{y},t) = \rho(\mathbf{y})\ddot{u}^2_i(\mathbf{x},\mathbf{y},t) \tag{125d}$$

The classical computational homogenization is based on the evaluation of the lower order equations of motion (i.e. Eqs. 125a and 125b). This practice leads to a non-dispersive model, in which microstructural inertia effects on the system response are ignored. It is necessary to include the equations of motion at $O(\zeta)$ and $O(\zeta^2)$ to devise a computational model that captures the micro-inertia effects. We note that the inclusion of even higher order equations of motion may lead to capturing higher order dynamics induced by heterogeneous microstructures. The inclusion of additional orders also leads to increased computational cost since higher order microstructure problems need to be evaluated.

3.1 O(1) Homogenization

Substituting Eqs. 121 and 124 into Eq. 125a, the balance equation at $O(\zeta^{-1})$ becomes:

$$\left\{C_{ijkl}(\mathbf{y})\left[e_{xkl}(\mathbf{u}^0) + e_{ykl}(\mathbf{u}^1)\right]\right\}_{,y_j} = 0 \tag{126}$$

which is defined over the characteristic volume. Taking advantage of the linearity of Eq. 126 and using the separation of variables, the displacement, $\mathbf{u}^1$, is expressed as:

$$u^1_i(\mathbf{x},\mathbf{y},t) = U^1_i(\mathbf{x},t) + H_{ikl}(\mathbf{y})e_{xkl}(\mathbf{u}^0(\mathbf{x},t)) \tag{127}$$

where $\mathbf{H}(\mathbf{y})$ is the first order microstructure influence function. $\mathbf{H}$ is a 3$^{\text{rd}}$ rank tensor with symmetry on the second and third indices (i.e. $H_{ikl} = H_{ilk}$). Substituting Eq. 127 into Eq. 126, the equation of motion at $O(\zeta^{-1})$ is written in terms of the influence function:

$$\{C_{ijkl}(\mathbf{y})(h_{klmn}(\mathbf{y}) + I_{klmn})\}_{,y_j} = 0; \quad \mathbf{y} \in \Theta \tag{128}$$

in which $h_{ijmn}(\mathbf{y}) = H_{(i,y_j)mn}(\mathbf{y})$ is the polarization function. When furnished with appropriate boundary conditions, Eq. 128 can be solved for the first order influence function, $\mathbf{H}$. The local periodicity of the first order displacement field, $\mathbf{u}^1$, leads to the periodicity of the first order influence function. $\mathbf{H}$ is normalized to ensure uniqueness:

$$\langle H_{ikl}(\mathbf{y})\rangle = \frac{1}{|\Theta|}\int_{\Theta} H_{ikl}(\mathbf{y})d\mathbf{y} = 0 \tag{129}$$

Given : The tensor of elastic moduli, $\mathbf{C}(\mathbf{y})$.

Find : The first order influence function, $\mathbf{H} : \Theta \to \mathbb{R}^{n_{\text{sd}} \times n_{\text{sd}} \times n_{\text{sd}}}$, such that:

- Equilibrium:

$$\{C_{ijkl}(\mathbf{y})\,[h_{klmn}(\mathbf{y}) + I_{klmn}]\}_{,y_j} = 0; \quad \mathbf{y} \in \Theta$$

$$h_{ijmn}(\mathbf{y}) = 1/2\left(H_{imn,y_j}(\mathbf{y}) + H_{jmn,y_i}(\mathbf{y})\right); \quad \mathbf{y} \in \Theta$$

- Periodicity condition at the microscale:

$$H_{ikl}(\mathbf{y}) = H_{ikl}(\mathbf{y} + \mathbf{k}\hat{\mathbf{y}}); \quad \mathbf{y} \in \Gamma_\Theta = \partial\Theta$$

- Normalization condition:

$$\langle H_{ikl}(\mathbf{y})\rangle = 0; \quad \mathbf{y} \in \Theta$$

Box 4: Summary of the boundary value problem for $\mathbf{H}(\mathbf{y})$.

in which $\langle\cdot\rangle = \frac{1}{|\Theta|}\int_{\Theta} \cdot\, d\mathbf{y}$ denotes the averaging operator, and $|\Theta|$ is the volume of Θ. Eq. 129 is necessary to ensure that the influence function problem has a unique solution. By ensuring that the average of the influence function vanishes, the rigid body modes are eliminated from the solution. The boundary value problem for $\mathbf{H}$ is summarized in Box 4.

Applying the averaging operator to Eq. 125b and exploiting the local periodicity of $\boldsymbol{\sigma}^1$, the homogenized equation of motion at $O(1)$ is written as:

$$\rho_0 \ddot{u}_i^0(\mathbf{x}, t) = D_{ijmn}^0 e_{xmn}(\mathbf{u}^0)_{,x_j}; \quad \mathbf{x} \in \Omega \tag{130}$$

where $\rho_0 = \langle \rho \rangle$ is the volume-averaged density; and

$$D_{ijmn}^0 = \langle C_{ijmn}^0(\mathbf{y}) \rangle \tag{131}$$

$$C_{ijmn}^0(\mathbf{y}) = C_{ijkl}(\mathbf{y})(h_{klmn}(\mathbf{y}) + I_{klmn}) \tag{132}$$

Given: The homogenized elastic modulus tensor, $\mathbf{D}^0$, the volume-averaged density ρ_0, and the initial and boundary data, $\bar{\mathbf{u}}(\mathbf{x}, t)$, $\bar{t}(\mathbf{x}, t)$, $\hat{\mathbf{u}}(\mathbf{x})$, $\hat{\mathbf{v}}(\mathbf{x})$.

Find: The macroscopic deformation, $\mathbf{u}^0 : \Theta \times [0, t_0] \to \mathbb{R}^{n_{\text{sd}}}$ such that:

- Equation of motion:

  $\rho_0 \ddot{u}_i^0(\mathbf{x}, t) = D_{ijmn}^0 e_{xmn}(\mathbf{u}^0)_{,x_j}; \quad \mathbf{x} \in \Omega$
- Boundary conditions:

  $u_i^0(\mathbf{x}, t) = \bar{u}_i(\mathbf{x}, t); \quad \mathbf{x} \in \Gamma^u;$

  $D_{ijmn}^0(e_{xmn}(\mathbf{u}^0))n_j = \bar{t}_i(\mathbf{x}, t); \quad \mathbf{x} \in \Gamma^t$
- Initial conditions:

  $u_i^0(\mathbf{x}, 0) = \hat{u}_i(\mathbf{x}); \quad \mathbf{x} \in \Omega$

  $\dot{u}_i^0(\mathbf{x}, 0) = \hat{v}_i(\mathbf{x}); \quad \mathbf{x} \in \Omega$

Box 5: Summary of the initial boundary value problem for $\mathbf{u}^0$.

in which, $\mathbf{D}^0$ is the zeroth homogenized elastic modulus tensor and $\mathbf{I}$ is the fourth rank identity tensor. The homogenized equation of motion at $O(1)$, along with the initial and boundary conditions, can be evaluated for $\mathbf{u}^0$. The IBVP for evaluating

$\mathbf{u}^0$ is summarized in Box 5. This model cannot account for micro-inertia effects as illustrated by the numerical examples below.

3.2 $O(\zeta)$ Homogenization

Substituting Eq. 130 to Eq. 125b and considering Eqs. 121 and 124, the equation of motion at $O(1)$ is expressed as:

$$\begin{aligned}\left\{C_{ijkl}(\mathbf{y})\left[e_{ykl}(\mathbf{u}^2)+e_{xkl}(\mathbf{U}^1)+H_{kmn}(\mathbf{y})e_{xmn}(\mathbf{u}^0)_{,x_l}\right]\right\}_{,y_j}&\\ =\left\{\left[\theta(\mathbf{y})D^0_{ijmn}-C^0_{ijmn}(\mathbf{y})\right]e_{xmn}(\mathbf{u}^0)\right\}_{,x_j}&\end{aligned} \tag{133}$$

where $\theta(\mathbf{y})=\rho(\mathbf{y})/\rho_0$. The second order displacement, $\mathbf{u}^2$, is approximated by introducing the second order influence function, $\mathbf{P}(\mathbf{y})$. Exploiting the linearity of Eq. 133:

$$u_i^2(\mathbf{x},\mathbf{y},t)=U_i^2(\mathbf{x},t)+H_{ikl}(\mathbf{y})e_{xkl}(\mathbf{U}^1)+P_{ijkl}(\mathbf{y})e_{xkl}(\mathbf{u}^0)_{,x_j} \tag{134}$$

in which $\mathbf{P}$ is a fourth rank tensor and symmetric with respect to the last two indices, but not necessarily with respect to the first two indices (i.e., $P_{ijkl}\neq P_{jikl}$ and $P_{ijkl}\neq P_{klij}$) for arbitrary microstructural configurations. Substituting Eq. 134 into Eq. 133, the equation of motion at $O(\zeta^0)$ is derived as:

$$C^1_{ijpmn,y_j}=\theta(\mathbf{y})D^0_{ipmn}-C^0_{ipmn}(\mathbf{y});\quad \mathbf{y}\in\Theta \tag{135}$$

and

$$C^1_{ijpmn}(\mathbf{y})=C_{ijkl}\left\{p_{klpmn}(\mathbf{y})+H_{kmn}(\mathbf{y})\delta_{lp}\right\} \tag{136}$$

in which $p_{klpmn}(\mathbf{y})=P_{(k,y_l)pmn}/2$ and $\boldsymbol{\delta}$ is the Kronecker delta. The periodicity and the normalization conditions are employed similarly to the BVP for the first order influence function, $\mathbf{H}$. The summary of the boundary value problem for the second order influence function is summarized in Box 6.

Given: The material properties, $\mathbf{C}$ and $\mathbf{D}^0$, and the first order influence function, $\mathbf{H}(\mathbf{y})$.

Find: The second order influence function, $\mathbf{P}(\mathbf{y}) : \Theta \rightarrow \mathbb{R}^{n_{sd} \times n_{sd} \times n_{sd} \times n_{sd}}$ such that:

- Equilibrium:

$$C_{ijkl}(\mathbf{y}) \left\{ p_{klpmn}(\mathbf{y}) + H_{kmn}(\mathbf{y})\delta_{lp} \right\}_{y_j} = \theta(\mathbf{y}) D^0_{ipmn} - C^0_{ipmn}(\mathbf{y}); \quad \mathbf{y} \in \Theta$$

$$p_{klpmn} = \frac{1}{2}(P_{kpmn,y_l} + P_{lpmn,y_k}); \quad \mathbf{y} \in \Theta$$

- Periodicity condition at the microscale:

$$P_{ijkl}(\mathbf{y}) = P_{ijkl}(\mathbf{y} + \mathbf{k}\hat{\mathbf{y}}); \quad \mathbf{y} \in \Gamma_\Theta$$

- Normalization condition:

$$\langle P_{ijkl}(\mathbf{y}) \rangle = 0; \quad \mathbf{y} \in \Theta$$

Box 6: Summary of the boundary value problem for $\mathbf{P}(\mathbf{y})$.

Substituting Eqs. 127 and 134 into Eq. 124, the first order stress tensor is expressed as:

$$\sigma^1_{ij}\left(\mathbf{x}, \mathbf{y}, t\right) = C^0_{ijmn}(\mathbf{y}) e_{xmn}(\mathbf{U}^1) + C^1_{ijpmn}(\mathbf{y}) e_{xmn}(\mathbf{u}^0)_{,x_p} \tag{137}$$

Applying the averaging operator to Eq. 125c, using Eq. 137 and the local periodicity of $\boldsymbol{\sigma}^2$, the homogenized equation of motion at $O(\zeta)$ takes the form:

$$\rho_0 \ddot{U}^1_i + \langle \rho(\mathbf{y}) H_{ikl}(\mathbf{y}) \rangle e_{xkl}(\ddot{\mathbf{u}}^0) = D^0_{ijmn} e_{xmn}(\mathbf{U}^1)_{,x_j} + D^1_{ijkmn} e_{xmn}(\mathbf{u}^0)_{,x_k x_j}; \quad \mathbf{x} \in \Omega \tag{138}$$

where the first order homogenized stiffness tensor, $\mathbf{D}^1$, is defined as:

$$D^1_{ijpmn} = \langle C^1_{ijpmn}(\mathbf{y}) \rangle \tag{139}$$

3.3 $O(\zeta^2)$ Homogenization

The homogenization at $O(\zeta^2)$ follows a similar procedure to $O(\zeta)$ homogenization. Substituting Eq. 138 to Eq. 125c, and exploiting Eqs. 124, 127, 130, and 134 yield:

$$\begin{aligned}&\left\{C_{ijkl}(\mathbf{y})\left[e_{ykl}(\mathbf{u}^3)+e_{xkl}(\mathbf{U}^2)+H_{kmn}(\mathbf{y})e_{xmn}(\mathbf{U}^1)_{,x_l}+P_{krmn}(\mathbf{y})e_{xmn}(\mathbf{u}^0)_{,x_rx_l}\right]\right\}\\&=\left\{\left[\theta(\mathbf{y})D^1_{ijlmn}-C^1_{ijlmn}(\mathbf{y})\right]+\theta(\mathbf{y})\left[H_{ikl}(\mathbf{y})-\rho_0^{-1}\langle\rho(\mathbf{y})H_{ikl}(\mathbf{y})\rangle\right]D^0_{kjmn}\right\}e_{xmn}(\mathbf{u}^0)_{,x_jx_l}\\&\qquad+\left\{\theta(\mathbf{y})D^0_{ijmn}-C^0_{ijmn}(\mathbf{y})\right\}e_{xmn}(\mathbf{U}^1)_{,x_j}\end{aligned}\tag{140}$$

Due to the linearity of Eq. 140, the third order displacement, $\mathbf{u}^3$, is approximated by introducing the third order influence function, $\mathbf{Q}(\mathbf{y})$:

$$u_i^3(\mathbf{x},\mathbf{y},t)=U_i^3(\mathbf{x},t)+H_{ikl}(\mathbf{y})e_{xkl}(\mathbf{U}^2)+P_{ijkl}(\mathbf{y})e_{xkl}(\mathbf{U}^1)_{,x_j}+Q_{ijkmn}(\mathbf{y})e_{xmn}(\mathbf{u}^0)_{,x_kx_j}\tag{141}$$

Substituting Eq. 141 to Eq. 140, the governing equation for the third order influence function, after some algebra, becomes:

$$C^2_{ijprmn,y_j}=\theta(\mathbf{y})D^1_{irpmn}-C^1_{irpmn}(\mathbf{y})+\theta(\mathbf{y})\left\{H_{ikp}(\mathbf{y})-\rho_0^{-1}\langle\rho H_{ikp}\rangle\right\}D^0_{krmn};\quad \mathbf{y}\in\Theta\tag{142}$$

where

$$C^2_{ijprmn}(\mathbf{y})=C_{ijkl}(\mathbf{y})\left\{q_{klprmn}(\mathbf{y})+P_{krmn}(\mathbf{y})\delta_{lp}\right\}\tag{143}$$

in which $q_{klprmn}=Q_{(k,y_l)prmn}$. The third order influence function, $\mathbf{Q}$, is a fifth rank tensor with minor symmetry only on the last two indices (i.e. $Q_{ijkmn}=Q_{ijknm}$). Since the explicit computation of $\mathbf{Q}$ is not necessary in the high order homogenization model described below, the BVP for $\mathbf{Q}$ is not discussed further. Substituting Eqs. 134 and

141 to Eq. 124 yields:

$$\sigma^2_{ij}(\mathbf{x},\mathbf{y},t) = C^0_{ijmn}(\mathbf{y})e_{xmn}(\mathbf{U}^2) + C^1_{ijrmn}(\mathbf{y})e_{xmn}(\mathbf{U}^1)_{,x_r} + C^2_{ijprmn}(\mathbf{y})e_{xmn}(\mathbf{u}^0)_{,x_r x_p} \tag{144}$$

Applying the averaging operator to Eq. 125d, exploiting Eq. 144 and considering that $\boldsymbol{\sigma}^3$ is locally periodic, the homogenized equation of motion at $O(\zeta^2)$ is then derived as:

$$\begin{aligned}&\rho_0 \ddot{U}^2_i(\mathbf{x},t) + \langle \rho(\mathbf{y}) H_{ikl}(\mathbf{y})\rangle e_{xkl}(\ddot{\mathbf{U}}^1) + \langle \rho(\mathbf{y}) P_{ijkl}(\mathbf{y})\rangle e_{xkl}(\ddot{\mathbf{u}}^0)_{,y_j}\\ &\quad = D^0_{ijmn} e_{xmn}(\mathbf{U}^2)_{,x_j} + D^1_{ijrmn} e_{xmn}(\mathbf{U}^1)_{,x_r x_j} + D^2_{ijprmn} e_{xmn}(\mathbf{u})^0_{,x_r x_p x_j}; \quad \mathbf{x}\in\Omega\end{aligned} \tag{145}$$

where the second order homogenized stiffness tensor, $\mathbf{D}^2$, is expressed as:

$$D^2_{ijprmn} = \langle C^2_{ijprmn}(\mathbf{y})\rangle \tag{146}$$

It is possible to express the second order homogenized stiffness tensor, $\mathbf{D}^2$, as a function of the first and second influence functions, eliminating the dependence on $\mathbf{Q}$ [30]:

$$\begin{aligned}D^2_{ijprmn} &= \rho_0^{-1}\langle \rho(\mathbf{y}) P_{qrmn}(\mathbf{y})\rangle D^0_{pqij} + \rho_0^{-1}\langle \rho(\mathbf{y}) H_{sij}(\mathbf{y})\rangle D^1_{srpmn}\\ &+ \langle p_{klrmn}(\mathbf{y}) C^1_{klpij}(\mathbf{y})\rangle - \langle H_{sij}(\mathbf{y}) C^1_{srpmn}(\mathbf{y})\rangle + \rho_0^{-1}\langle \rho(\mathbf{y}) H_{sij}(\mathbf{y}) H_{spq}(\mathbf{y})\rangle D^0_{qrmn}\\ &- \rho_0^2 \langle \rho(\mathbf{y}) H_{sij}(\mathbf{y})\rangle \langle \rho(\mathbf{y}) H_{spq}(\mathbf{y})\rangle D^0_{qrmn}\end{aligned} \tag{147}$$

Considering a homogenized displacement field by including the first two orders of the displacement decomposition and averaging over the characteristic volume:

$$U_i(\mathbf{x},t) = \langle u_i(\mathbf{x},\mathbf{y},t)\rangle = u^0_i + \zeta U^1_i + \zeta^2 U^2_i + O(\zeta^3) \tag{148}$$

The summation of Eqs. 130, 138 and 145 leads to a high order homogenized equation of motion in terms of the mean displacement, $\mathbf{U}$. Neglecting $O(\zeta^3)$ and the higher order terms:

$$\begin{aligned}\rho_0\ddot{U}_i(\mathbf{x},t) + \zeta\langle\rho(\mathbf{y})H_{ikl}(\mathbf{y})\rangle e_{xkl}(\ddot{\mathbf{U}}) + \zeta^2\langle\rho(\mathbf{y})P_{ijmn}(\mathbf{y})\rangle e_{xmn}(\ddot{\mathbf{U}})_{,x_j} = \\ D^0_{ijmn}e_{xmn}(\mathbf{U})_{,x_j} + \zeta D^1_{ijkmn}e_{xmn}(\mathbf{U})_{,x_kx_j} + \zeta^2 D^2_{ijprmn}e_{xmn}(\mathbf{U})_{,x_rx_px_j}; \quad \mathbf{x}\in\Omega \quad (149)\end{aligned}$$

The terms inducing micro-inertia effects in the macroscopic equation of motion defined in Eq. 149 are scaled by orders of ζ, which leads to zero at the asymptotic limit. This appears to indicate that the contribution of the high order terms are trivial. This apparent contradiction is resolved by observing that the coefficients in these terms themselves are size dependent. It can be shown that $\mathbf{D}^1$ and $\langle\rho\mathbf{H}\rangle$ are proportional to $\hat{l}$, and $\mathbf{D}^2$ and $\langle\rho\mathbf{P}\rangle$ are proportional to $\hat{l}^2$ [16]:

$$\mathbf{D}^1 = O(\mathbf{C}\hat{l}); \quad \langle\rho\mathbf{H}\rangle = O(\rho\hat{l}) \quad (150a)$$

$$\mathbf{D}^2 = O(\mathbf{C}\hat{l}^2); \quad \langle\rho\mathbf{P}\rangle = O(\rho\hat{l}^2) \quad (150b)$$

where $\hat{l} = l/\zeta$ is the characteristic length of the microstructure in the stretched coordinate system $\mathbf{y}$, and l the characteristic length of microstructure in the macroscopic coordinate system $\mathbf{x}$. $\mathbf{D}^1$, $\mathbf{D}^2$, $\langle\rho\mathbf{H}\rangle$ and $\langle\rho\mathbf{P}\rangle$ are homogeneous functions of degree 1. Consequently,

$$\zeta\mathbf{D}^1 = O(\mathbf{C}l); \quad \zeta\langle\rho\mathbf{H}\rangle = O(\rho l) \quad (151a)$$

$$\zeta^2\mathbf{D}^2 = O(\mathbf{C}l^2); \quad \zeta^2\langle\rho\mathbf{P}\rangle = O(\rho l^2) \quad (151b)$$

In this study, $\zeta\mathbf{D}^1$, $\zeta^2\mathbf{D}^2$, $\zeta\langle\rho\mathbf{H}\rangle$ and $\zeta^2\langle\rho\mathbf{P}\rangle$ which are directly calculated using the physical geometric size as opposed to stretched configurations. The coefficients are therefore expressed at order $O(1)$.

4 A Simplified High Order Homogenization Model

Numerical evaluation of the equation of motion for the homogenized response as defined in Eq. 149 is complicated and non-standard. The presence of the fourth order spatial derivative of the homogeneous displacement precludes the use of the finite element method with C^0-continuous shape functions. Alternative numerical schemes such as isogeometric analysis which possesses basis functions with higher continuity [23], finite element analysis with C^1-continuous shape functions [56], or mixed-finite element method [13] are possible paths for directly evaluating this system.

We propose a high order homogenization model derived based on certain observations and simplifications on the material microstructures. The following conditions are assumed: (1) the homogenized material must exhibit orthotropy or higher symmetry; and (2) within a microstructural constituent domain, the elastic modulus tensor and constituent density are assumed to be constant, but the properties are allowed to vary from constituent to constituent and generate micro-inertia under dynamic conditions. Using the first simplification, the first order stiffness tensor vanishes: $\mathbf{D}^1 = 0$ [30]. Substituting Eqs. 127, 134 and 141 into Eq. 119, taking the temporal derivative twice, premultiplying by density and averaging over the characteristic volume yield the following expression:

$$\langle \rho \ddot{u}_i \rangle = \rho_0 \ddot{U}_i(\mathbf{x}, t) + \zeta \langle \rho H_{ikl} \rangle e_{xkl}(\ddot{\mathbf{U}}) + \zeta^2 \langle \rho P_{ijkl} \rangle e_{xkl}(\ddot{\mathbf{U}})_{,x_j} + O(\zeta^3) \tag{152}$$

Comparing the differential orders in Eq. 152 to classical dispersion theories, (e.g. Mindlin's theory [45]), the second term on the right hand side is non-standard. When the assumption of piecewise constant material parameters mentioned above is considered, it has been demonstrated in [39] that the coefficient of this term is identically zero for 1-D cases. In Appendix B, it is shown that this term vanishes for high dimensional cases as well:

$$\langle \rho H_{ikl} \rangle = 0 \tag{153}$$

Next, we turn our attention to the term in Eq. 149 that involves the fourth order derivative of the homogenized displacement field. We consider the following approximation for the homogenized stiffness tensor, $\mathbf{D}^2$:

$$D^2_{ijprmn} \approx A_{ijpq} D^0_{qrmn} \tag{154}$$

in which, $\mathbf{D}^2$ is taken to be proportional to $\mathbf{D}^0$. Note that the approximation cannot be exactly satisfied for any $\mathbf{A}$. Further, since the multiplication only permutes over the fourth index, inversion of $\mathbf{D}^0$ for identifying $\mathbf{A}$ is not possible. Alternatively, we employ the Moore-Penrose pseudo-inverse for identifying $\mathbf{A}$. Define:

$$A^*_{ijpq} = D^2_{ijprmn} D^{0\text{ -mp}}_{qrmn} \tag{155}$$

where '-mp' denotes the Moore-Penrose pseudo-inverse. The pseudo-inverse provides the solution, $\mathbf{A}^*$, that minimizes the discrepancy between $\mathbf{D}^2$ and its approximation, $\mathbf{D}^{2*}$, computed as $D^{2*}_{ijprmn} = A^*_{ijpq} D^0_{qrmn}$ with respect to the Frobenius norm. The pseudo-inverse is well defined and unique for all matrices including non-square matrices whose entries are real or complex. Additional details on the properties of Moore-Penrose pseudo-inverse are provided in Appendix C

$\mathbf{A}^*$ possesses minor symmetry with respect to the first two indices (i.e. $A^*_{ijpq} = A^*_{jipq}$). The fourth order term in Eq. 149 is expressed as:

$$\zeta^2 D^2_{ijprmn} e_{xmn}(\mathbf{U})_{,x_r x_p x_j} = \zeta^2 A^*_{ijpq} D^0_{qrmn} e_{xmn}(\mathbf{U})_{,x_r x_p x_j} \tag{156}$$

Using Eq. 130 and neglecting $O(\zeta^3)$ and higher order terms:

$$\zeta^2 A^*_{ijpq} D^0_{qrmn} (e_{xmn}(\mathbf{U}))_{,x_r x_p x_j} = \zeta^2 \rho_0 A^*_{ijmn} e_{xmn}(\ddot{\mathbf{U}})_{,x_j} \tag{157}$$

Substituting Eq. 157 to Eq. 149, the macroscale high order equation of motion becomes:

$$\rho_0 \ddot{U}_i(\mathbf{x}, t) + \zeta^2 \langle \rho P_{ijmn} \rangle (e_{xmn}(\ddot{\mathbf{U}}))_{,x_j} = D^0_{ijmn}(e_{xmn}(\mathbf{U}))_{,x_j} + \zeta^2 \rho_0 A^*_{ijmn} e_{xmn}(\ddot{\mathbf{U}})_{,x_j} \tag{158}$$

By employing the relationship in Eq. 157, the fourth order derivative term in the equation of motion over the homogenized domain is eliminated without loss of generality. The second order influence function, **P**, exhibits minor symmetry with respect to the first two indices only for geometrically symmetric microstructures, but is non-symmetric for arbitrary microstructures. In order to conserve angular momentum, we consider only the symmetric part of **P**. Let:

$$J_{ijmn} = \frac{1}{2} \left(\langle \rho P_{ijmn} \rangle + \langle \rho P_{jimn} \rangle \right) \tag{159}$$

$\mathbf{A}^*$ is decomposed into its symmetric and antisymmetric components as:

$$A_{ijkl} = \frac{1}{2} \left(A^*_{ijkl} + A^*_{ijlk} \right) \tag{160a}$$

$$B_{ijkl} = \frac{1}{2} \left(A^*_{ijkl} - A^*_{ijlk} \right) \tag{160b}$$

Using the symmetry of the strain tensor along with Eq. 160, the equation of motion for the high order homogenization model reduces to:

$$\rho_0 \ddot{U}_i = D^0_{ijmn}(e_{xmn}(\mathbf{U}))_{,x_j} - L_{ijmn}(e_{xmn}(\ddot{\mathbf{U}}))_{,x_j}; \quad \mathbf{x} \in \Omega \tag{161}$$

where the micro-inertia induced acceleration modulus tensor, **L**, is defined as:

$$L_{ijmn} = \zeta^2 (J_{ijmn} - \rho_0 A_{ijmn}) \tag{162}$$

The acceleration modulus tensor, **L**, satisfies the minor symmetry for both the first two and the last two indices (i.e. $L_{ijmn} = L_{jimn}$; $L_{ijmn} = L_{ijnm}$). By Eqs. 159 and 160, the antisymmetric components of the micro-inertia terms in the governing equation of motion is discarded. This simplification amounts to the decomposition of the micro-inertia into transitional and rotational components, and eliminating the rotational micro-inertia effects from the formulation.

From Eq. 161, the constitutive equation for the high order model at the macroscale is defined as:

$$\Sigma_{ij}(\mathbf{x}, t) = D^0_{ijmn} e_{xmn}(\mathbf{U}) - L_{ijmn} e_{xmn}(\ddot{\mathbf{U}}); \quad \mathbf{x} \in \Omega \tag{163}$$

where $\boldsymbol{\Sigma}$ is defined as the homogenized stress tensor which is related to the second order spatial derivative of not only the homogenized displacement, **U**, but also the acceleration, $\ddot{\mathbf{U}}$. The second term on the right hand side of Eq. 163 represents the influence of micro-inertia. The IBVP for the high order homogenization model is summarized in Box 7.

Equation 163 is obtained by substituting the fourth order spatial derivative of the displacement field with a second spatial derivative - second temporal derivative term. A one-dimensional numerical example is provided to demonstrate the impact of this substitution. The solution strategy for one-dimensional problems is provided in [39]. Consider a bi-phase one-dimensional structure with elastic moduli and density of $E^{(1)} = 2$ GPa, $\rho^{(1)} = 7900$ kg/m^3 for phase 1 and $E^{(2)} = 22.4$ MPa, $\rho^{(2)} = 1070$ kg/m^3 for phase 2. The volume fraction of phase 1 is 0.4. This structure consists of 20 microstructures and subjected to a step displacement load. Figure 19 illustrates the displacement histories computed using the model, which includes the fourth order spatial derivative and the model, which includes the second spatial - second temporal derivative term. The observation point is $0.1L$ distance (L is the length of the structure) from the boundary of excitation. The displacement histories indicate that the models capture the dispersion in reasonable agreement with some discrepancy in the waves following the main dispersive wave.

Given: The homogenized material properties at the macroscale, $\mathbf{D}^0$; the tensor of the acceleration moduli, $\mathbf{L}$, initial conditions $\hat{\mathbf{u}}(\mathbf{x})$, $\hat{\mathbf{v}}(\mathbf{x})$; and the boundary conditions $\bar{\mathbf{u}}(\mathbf{x}, t)$, $\bar{\mathbf{t}}(\mathbf{x}, t)$.

Find: The macroscale deformation, $\mathbf{U}(\mathbf{x}, t) : \Omega \times [0, t_0] \rightarrow \mathbb{R}^{n_{\mathrm{sd}}}$ such that:

- Equation of motion:

$$\rho_0 \ddot{U}_i = \Sigma_{ij,x_j}; \quad \mathbf{x} \in \Omega$$

- Constitutive relation:

$$\Sigma_{ij}(\mathbf{x}, t) = D^0_{ijmn}(e_{xmn}(\mathbf{U})) - L_{ijmn}(e_{xmn}(\ddot{\mathbf{U}})); \quad \mathbf{x} \in \Omega$$

- Boundary conditions:

$$U_i(\mathbf{x}, t) = \bar{u}_i(\mathbf{x}, t); \quad \mathbf{x} \in \Gamma^u$$

$$\Sigma_{ij} n_j = \bar{t}_i(\mathbf{x}, t); \quad \mathbf{x} \in \Gamma^t$$

- Initial conditions:

$$U_i(\mathbf{x}, 0) = \hat{u}_i(\mathbf{x}); \quad \mathbf{x} \in \Omega$$

$$\dot{U}_i(\mathbf{x}, 0) = \hat{v}_i(\mathbf{x}); \quad \mathbf{x} \in \Omega$$

Box 7: Summary of the initial boundary value problem for evaluation of the macroscale displacement, $\mathbf{U}$.

5 Finite Element Formulation

In this section, the numerical evaluations of the first and second order influence function problems defined in Boxes 4 and 6, respectively, as well as the macroscopic homogenization model defined in Box 7 are presented. The basis of the computations for all the three problems is the standard Bubnov-Galerkin finite element method with

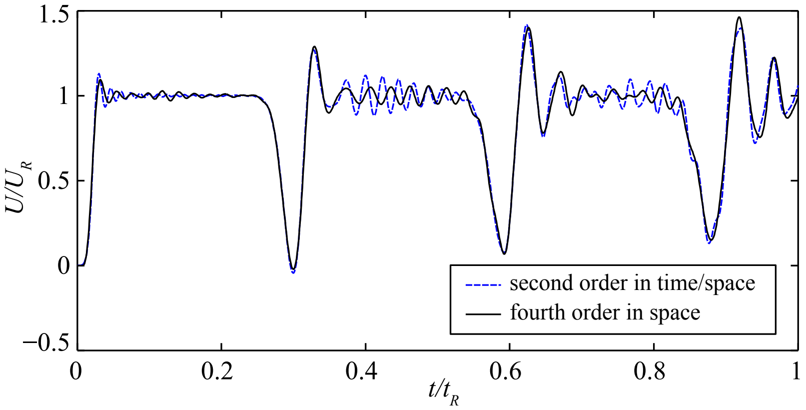

Figure 17: Displacement histories computed using a model with the fourth order spatial derivative term and a model with the second order spatial - second order temporal derivative term.

C^0-continuous shape functions. In the evaluation of the macroscopic problem, a Hybrid Laplace Transform-Finite Element Method is proposed to solve the macroscopic IBVP.

The computation of the first order influence function, $\mathbf{H}$, has been standard practice in the computational homogenization literature [38] and only a brief summary is therefore presented here for completeness. The computation of the second order influence function, $\mathbf{P}$, has not been a part of the traditional computational homogenization method. This section includes the detailed formulation for evaluating the second order influence function, $\mathbf{P}$.

5.1 First Order Influence Function Problem

Equation 128 is expressed in the weak form using the local periodicity boundary condition on $\mathbf{y} \in \Theta$ as:

$$\int_{\Theta} w_{i,y_j}(\mathbf{y}) C_{ijkl}(\mathbf{y}) h_{klmn}(\mathbf{y}) d\mathbf{y} = -\int_{\Theta} w_{i,y_j}(\mathbf{y}) C_{ijmn}(\mathbf{y}) d\mathbf{y} \tag{164}$$

where $\mathbf{w} \in \mathcal{W}_{\text{per}} \subset \left[H^1_{\text{per}}(\Theta)\right]^{n_{\text{sd}}}$; and $H^1_{\text{per}}(\Theta)$ is the subspace of functions in $H^1(\Theta)$ that are periodic along Γ_Θ, and $H^1(\Theta)$ is the Sobolev space of functions with square integrable derivatives. We seek the solution of the first order influence function in the finite dimensional space, $\mathbf{H} \in \mathcal{H}_{\text{per}}(\Theta) \subset \left[H^1_{\text{per}}(\Theta)\right]^{n_{\text{sd}} \times n_{\text{sd}} \times n_{\text{sd}}}$ such that:

$$\mathcal{H}_{\text{per}}(\Theta) := \left\{ \mathbf{H}(\mathbf{y}) \mid H_{ikl}(\mathbf{y}) = \sum_{A=1}^{M} N^{[A]}(\mathbf{y}) H^{[A]}_{ikl};\ H^{[A]}_{ikl} \text{ is } \Theta \text{ -periodic; } \langle H_{ikl} \rangle = 0;\ H^{[A]}_{ikl} = H^{[A]}_{ilk} \right\} \tag{165}$$

with the appropriate continuity and smoothness conditions. $N^{[A]}$ denotes the shape function of node A within the discretization of the characteristic volume; M denotes the total number of nodes, and $H^{[A]}_{ikl}$ the nodal coefficients. Following the standard Bubnov-Galerkin setting, $\mathcal{W}_{\text{per}}$ is defined similarly to Eq. 165.

Substituting the discretizations of the influence function and the weight function into the weak form and expressing the terms in matrix-vector form using the Voigt notation yields the following discrete system:

$$\mathbf{K}_H \mathbf{d}_H = \mathbf{F}_H \tag{166}$$

which is formed by assembling the element matrices:

$$\mathbf{K}_H = \mathop{\mathbf{A}}_{e} \mathbf{K}^e_H; \quad \mathbf{d}_H = \mathop{\mathbf{A}}_{e} \mathbf{d}^e_H; \quad \mathbf{F}_H = \mathop{\mathbf{A}}_{e} \mathbf{F}^e_H \tag{167}$$

$\mathbf{A}$ denotes the assembly operation. The element matrix of unknown coefficients of an arbitrary element e is expressed as:

$$\mathbf{d}^e_H = \begin{bmatrix} \tilde{\mathbf{H}}^{e[1]} & \tilde{\mathbf{H}}^{e[2]} & \dots & \tilde{\mathbf{H}}^{e[M_e]} \end{bmatrix}^T \tag{168}$$

in which T denotes the matrix transpose, M_e denotes the number of nodes in the element, and for 2-D elements, the matrix of unknown coefficients at node A of element e is:

$$\tilde{\mathbf{H}}^{e[A]} = \begin{bmatrix} H_{111}^{e[A]} & H_{122}^{e[A]} & H_{112}^{e[A]} \\ H_{211}^{e[A]} & H_{222}^{e[A]} & H_{212}^{e[A]} \end{bmatrix}^T \tag{169}$$

The element stiffness and force matrices are expressed as:

$$\mathbf{K}_H^e = \int_{\Theta^e} \mathbf{B}^{e^T}(\mathbf{y})\, \hat{\mathbf{C}} \mathbf{B}^e(\mathbf{y})\, d\mathbf{y} \tag{170}$$

$$\mathbf{F}_H^e = \int_{\Theta^e} \mathbf{B}^{e^T}(\mathbf{y})\, \hat{\mathbf{C}} d\mathbf{y} \tag{171}$$

where Θ^e denotes the domain of element e, and

$$\mathbf{B}^e = \begin{bmatrix} \mathbf{B}^{e[1]} & \mathbf{B}^{e[2]} & \dots & \mathbf{B}^{e[M_e]} \end{bmatrix} \tag{172a}$$

$$\mathbf{B}^{e[A]} = \begin{bmatrix} N_{,y_1}^{e[A]}(\mathbf{y}) & 0 & N_{,y_2}^{e[A]}(\mathbf{y}) \\ 0 & N_{,y_2}^{e[A]}(\mathbf{y}) & N_{,y_1}^{e[A]}(\mathbf{y}) \end{bmatrix}^T \tag{172b}$$

and $\hat{\mathbf{C}}$ is the tensor of elastic moduli expressed in contracted Voigt notation.

5.2 Second Order Influence Function Problem

The weak form of Eq. 135, using the local periodicity condition, is expressed as:

$$\int_{\Theta} w_{i,y_j}(\mathbf{y}) \left(C_{ijkl}(p_{klpmn}(\mathbf{y}) + H_{kmn}(\mathbf{y})\delta_{lp}) \right) d\mathbf{y} = \\ - \int_{\Theta} w_i(\mathbf{y}) \left(\theta(\mathbf{y}) D_{ipmn}^0 - C_{ipmn}^0(\mathbf{y}) \right) d\mathbf{y} \tag{173}$$

for any weight function, $\mathbf{w} \in \mathcal{W}_{\text{per}}(\Theta)$. The solution approximation for the second order influence function belongs to the following finite dimensional space, $\mathbf{P} \in$

$\mathcal{P}_{\mathrm{per}}(\Theta) \subset \left[H^1_{\mathrm{per}}(\Theta)\right]^{n_{\mathrm{sd}} \times n_{\mathrm{sd}} \times n_{\mathrm{sd}} \times n_{\mathrm{sd}}}$:

$$\mathcal{P}_{\mathrm{per}}(\Theta) := \Bigg\{ \mathbf{P}(\mathbf{y}) \mid P_{ijmn}(\mathbf{y}) = \sum_{A=1}^{M} N^{[A]}(\mathbf{y}) P_{ijmn}^{[A]};\ P_{ijmn}^{[A]} \text{ is } \Theta \text{ -periodic; } \langle P_{ijmn} \rangle = 0;\ P_{ijmn}^{[A]} = P_{ijnm}^{[A]} \Bigg\} \tag{174}$$

where $P_{ijmn}^{[A]}$ denotes the nodal coefficient of $\mathbf{P}$ at node, A. Employing the discretization of the second order influence function in Eq. 174 and the weight function, the weak form of the influence function leads to the following discrete system:

$$\mathbf{K}_P \mathbf{d}_P = \mathbf{F}_P \tag{175}$$

formed by the assembly of element matrices defined analogous to Eq. 167. $\mathbf{d}_P$ is assembled from element matrices of unknown coefficients:

$$\mathbf{d}_P^e = \left[\tilde{\mathbf{P}}^{e[1]}, \tilde{\mathbf{P}}^{e[2]}, \ldots, \tilde{\mathbf{P}}^{e[M_e]}\right]^T \tag{176}$$

For 2-D elements, the matrix of unknown coefficients at node A of element e is:

$$\tilde{\mathbf{P}}^{e[A]} = \begin{bmatrix} P_{1111}^{e[A]} & P_{1122}^{e[A]} & P_{1112}^{e[A]} & P_{1211}^{e[A]} & P_{1222}^{e[A]} & P_{1212}^{e[A]} \\ P_{2111}^{e[A]} & P_{2122}^{e[A]} & P_{2112}^{e[A]} & P_{2211}^{e[A]} & P_{2222}^{e[A]} & P_{2212}^{e[A]} \end{bmatrix}^T \tag{177}$$

The matrix of unknown nodal coefficients, $\mathbf{d}_P$, has 6 columns for a 2-D problem and 18 columns for a full 3-D characteristic volume. Noting that the stiffness matrix, $\mathbf{K}_P$, defined below does not vary as a function of the components of $\mathbf{P}$, the factorization of $\mathbf{K}_P$ is conducted only once. It is also straightforward to see that the stiffness matrix for the second order influence function is identical to the stiffness matrix for the first order influence function (i.e. $\mathbf{K}_P = \mathbf{K}_H$). This further simplifies the computation of the influence functions since the factorization of only one matrix is necessary for both the first and second order influence function problems. The evaluations for the first and second order influence functions, however, are successive since the force matrix of the second order influence function depends on $\mathbf{H}$, (i.e. $\mathbf{F}_P = \mathbf{F}_P(\mathbf{H})$). The force matrix for element e is written as a sum of three components:

$$\mathbf{F}_P^e = \mathbf{F}_{P_1}^e + \mathbf{F}_{P_2}^e + \mathbf{F}_{P_3}^e \tag{178}$$

The first component of the force matrix is:

$$\mathbf{F}_{P_1}^e = -\int_{\Theta^e} \mathbf{B}^e(\mathbf{y})^T \, \hat{\mathbf{C}} \, \mathbf{G}(\mathbf{y}) d\mathbf{y} \tag{179}$$

where,

$$\mathbf{G} = \begin{bmatrix} H_{111}(\mathbf{y}) & H_{122}(\mathbf{y}) & H_{112}(\mathbf{y}) & 0 & 0 & 0 \\ 0 & 0 & 0 & H_{211}(\mathbf{y}) & H_{222}(\mathbf{y}) & H_{212}(\mathbf{y}) \\ H_{211}(\mathbf{y}) & H_{222}(\mathbf{y}) & H_{212}(\mathbf{y}) & H_{111}(\mathbf{y}) & H_{122}(\mathbf{y}) & H_{112}(\mathbf{y}) \end{bmatrix} \tag{180}$$

The components of $\mathbf{G}$ is computed using the solution of the first order influence function problem within Θ^e:

$$H_{ikl}(\mathbf{y}) = \sum_{B=1}^{M_e} N^{e[B]}(\mathbf{y}) H_{ikl}^{e[B]} \tag{181}$$

The second component of the force matrix is written as:

$$\mathbf{F}_{P_2}^e = -\int_{\Theta^e} \theta \, \mathbf{N}^{eT}(\mathbf{y}) \, d\mathbf{y} \, \tilde{\mathbf{D}}^0 \tag{182}$$

where,

$$\tilde{\mathbf{D}}^0 = \begin{bmatrix} D^0_{1111} & D^0_{1122} & D^0_{1112} & D^0_{1211} & D^0_{1222} & D^0_{1212} \\ D^0_{1211} & D^0_{1222} & D^0_{1212} & D^0_{2211} & D^0_{2222} & D^0_{2212} \end{bmatrix} \tag{183}$$

$$\mathbf{N}^e = \begin{bmatrix} N^{e[1]} & 0 & N^{e[2]} & 0 & \cdots & N^{e[M_e]} & 0 \\ 0 & N^{e[1]} & 0 & N^{e[2]} & \cdots & 0 & N^{e[M_e]} \end{bmatrix} \tag{184}$$

The components of $\tilde{\mathbf{D}}^0$ then are computed after the evaluation of the first order influence function problem. Note that the matrix representation of the tensors differs from the standard Voigt notation. The alternative notation employed here facilitates single index multiplication in the force components.

In order to evaluate the third component of the force term, we define

$$\psi_{ijkl}(\mathbf{y}) = C_{ijmn}(\mathbf{y}) \sum_{B=1}^{M_e} N^{e[B]}_{,y_n}(\mathbf{y}) H^{e[B]}_{mkl}; \quad \mathbf{y} \in \Theta^e \tag{185}$$

and denote $\hat{\boldsymbol{\psi}}$ using the Voigt representation, which is expressed as:

$$\hat{\boldsymbol{\psi}}(\mathbf{y}) = \hat{\mathbf{C}}(\mathbf{y}) \mathbf{B}^e(\mathbf{y}) \mathbf{d}^e_H \tag{186}$$

Employing the alternative notation analogous to those defined in Eqs. 183 and 184, the third component of the force term is written as:

$$\mathbf{F}^e_{P_3} = \int_{\Theta_e} \mathbf{N}^{eT}(\mathbf{y}) \left(\tilde{\boldsymbol{\psi}}(\mathbf{y}) + \tilde{\mathbf{C}}(\mathbf{y}) \right) d\mathbf{y} \tag{187}$$

in which $\tilde{\boldsymbol{\psi}}$ and $\tilde{\mathbf{C}}$ are the alternative matrix representation of $\boldsymbol{\psi}$ and $\mathbf{C}$, respectively:

$$\tilde{\boldsymbol{\psi}} = \begin{bmatrix} \psi_{1111} & \psi_{1122} & \psi_{1112} & \psi_{1211} & \psi_{1222} & \psi_{1212} \\ \psi_{1211} & \psi_{1222} & \psi_{1212} & \psi_{2211} & \psi_{2222} & \psi_{2212} \end{bmatrix} \tag{188}$$

$$\tilde{\mathbf{C}} = \begin{bmatrix} C_{1111} & C_{1122} & C_{1112} & C_{1211} & C_{1222} & C_{1212} \\ C_{1211} & C_{1222} & C_{1212} & C_{2211} & C_{2222} & C_{2212} \end{bmatrix} \tag{189}$$

5.3 Macroscopic Problem

The weak form of Eq. 161 is:

$$\int_\Omega \rho_0 w_i \ddot{U}_i d\mathbf{x} - \int_\Omega w_{i,x_j} L_{ijmn} e_{xmn}(\ddot{\mathbf{U}}) d\mathbf{x} + \int_\Omega w_{i,x_j} D^0_{ijmn} e_{xmn}(\mathbf{U}) d\mathbf{x} = \int_{\Gamma^t} w_i \Sigma_{ij} n_j d\mathbf{x} \tag{190}$$

for any weight function $\mathbf{w}$. The solution approximation for the homogenized displacement field belongs to the following finite dimensional space: $\mathbf{U} \in \mathcal{U}(\Omega)$

$$\mathcal{U}(\Omega) := \left\{ \mathbf{U}(\mathbf{x},t) | U_i(\mathbf{x},t) = \sum_{[C]=1}^{K} N^{[C]}(\mathbf{x}) U_i^{[C]}(t);\ U_i^{[C]}(t) = \bar{u}_i^{[C]}(t) \text{ when } \mathbf{x} \in \Gamma^u \right\} \tag{191}$$

where $N^{[C]}$ denotes the shape function of node C within the discretization of Ω; $U_i^{[C]}$ the nodal displacement and K the total number of nodes. Employing the discretization of the displacement field in Eq. 191 and the weight function, the weak form of the displacement leads to the following discrete system:

$$(\mathbf{M} + \mathbf{K}_L)\, \ddot{\mathbf{d}}_U(t) + \mathbf{K}\mathbf{d}_U(t) = \mathbf{F}(t) \tag{192}$$

which is formed by the assembly of pertinent element matrices:

$$\mathbf{M} = \mathop{\mathbf{A}}_{e} \mathbf{M}^e; \quad \mathbf{K}_L = \mathop{\mathbf{A}}_{e} \mathbf{K}_L^e; \quad \mathbf{K} = \mathop{\mathbf{A}}_{e} \mathbf{K}^e; \quad \mathbf{F}(t) = \mathop{\mathbf{A}}_{e} \mathbf{F}^e(t) \tag{193}$$

$\mathbf{d}_U(t)$ is assembled from the element matrix of unknown coefficients:

$$\mathbf{d}_U^e = \begin{bmatrix} \tilde{\mathbf{U}}^{e[1]}(t) & \tilde{\mathbf{U}}^{e[2]}(t) & \cdots & \tilde{\mathbf{U}}^{e[K_e]}(t) \end{bmatrix}^T \tag{194}$$

where K_e denotes the number of the element nodes. For 2-D elements:

$$\tilde{\mathbf{U}}^{e[C]} = \begin{bmatrix} U_1^{e[C]}(t) & U_2^{e[C]}(t) \end{bmatrix} \tag{195}$$

at node C in Ω^e. The element mass, acceleration, stiffness and force matrices are expressed respectively as:

$$\mathbf{M}^e = \int_{\Omega^e} \rho_0 \mathbf{N}^{eT}(\mathbf{x}) \mathbf{N}^e(\mathbf{x}) d\mathbf{x} \tag{196a}$$

$$\mathbf{K}_L^e = -\int_{\Omega^e} \mathbf{B}^{eT}(\mathbf{x}) \hat{\mathbf{L}} \mathbf{B}^e(\mathbf{x}) d\mathbf{x} \tag{196b}$$

$$\mathbf{K}^e = \int_{\Omega^e} \mathbf{B}^{eT}(\mathbf{x}) \hat{\mathbf{D}}^0 \mathbf{B}^e(\mathbf{x}) d\mathbf{x} \tag{196c}$$

$$\mathbf{F}^e = \int_{\Gamma^{et}} \mathbf{N}^{eT}(\mathbf{x}) \bar{\mathbf{t}}^e(\mathbf{x}, t) d\mathbf{x} \tag{196d}$$

where $\hat{\mathbf{D}}^0$ and $\hat{\mathbf{L}}$ are the tensors of the zeroth homogenized elastic moduli and acceleration moduli in contracted Voigt notation respectively.

The integration of Eq. 192 in the time domain is not straightforward. This is because the mass matrix ($= \mathbf{M} + \mathbf{K}_L$) includes the constitutive response, and mass lumping for explicit time integration would alter the constitutive response. The application of traction boundary conditions is also difficult since the stress is a function of the acceleration gradient, in addition to the strain. In this work, the homogenized balance equations are evaluated in the Laplace domain without resorting to the time integration and applying traction boundary conditions in the time domain. The Hybrid Laplace Transform-Finite Element Method [18, 61] is used to solve the macroscopic IBVP. The governing equations are converted from the time domain to the complex form in the Laplace domain.

The Laplace transform of an arbitrary, real valued, time varying function, $f \in \mathbb{R}$, is defined as:

$$\mathscr{F}(s) \equiv \mathscr{L}(f(t)) = \int_0^\infty e^{-st} f(t) dt \tag{197}$$

where, the Laplace argument, s and the Laplace transform, $\mathscr{F}$, are complex valued (i.e., $s \in \mathbb{C}$ and $\mathscr{F} := \mathbb{C} \to \mathbb{C}$). The representation of a field in the Laplace domain is referred to as the *associated* field. The derivative rule for the Laplace transform is given as:

$$\mathscr{L}(f\underbrace{, tt \ldots t}_{n \text{ times}}(t)) = s^n \mathscr{F}(s) - s^{n-1} f(0) - \ldots - f\underbrace{, tt \ldots t}_{n-1 \text{ times}}(0) \tag{198}$$

Considering statically undeformed initial conditions (i.e., $\hat{u}_i(\mathbf{x}) = \hat{v}_i(\mathbf{x}) = 0$), Eq. 192 is transformed to the complex form in the Laplace domain as:

$$\left(\mathbf{M}s^2 + \mathbf{K}_L s^2 + \mathbf{K}\right) \mathbf{d}_U^{\mathscr{L}}(s) = \mathbf{F}^{\mathscr{L}}(s) \tag{199}$$

where $\mathbf{F}^{\mathscr{L}}$ is the force vector in the Laplace domain, assembled from the element force vectors:

$$\mathbf{F}^{e\mathscr{L}} = \int_{\Gamma^{et}} \mathbf{N}^{eT} \bar{\mathbf{t}}^{e\mathscr{L}}(\mathbf{x}, s) d\mathbf{x} \tag{200}$$

Eq. 199 can be evaluated by the standard solution of linear complex equations. The constitutive relation in the Laplace domain is obtained by applying the Laplace transform to Eq. 163:

$$\Sigma_{ij}^{\mathscr{L}}(\mathbf{x}, s) = \left(D_{ijmn}^0 - L_{ijmn} s^2\right) e_{xmn}(\mathbf{U}^{\mathscr{L}}); \quad \mathbf{x} \in \Omega \tag{201}$$

in which, $\boldsymbol{\Sigma}^{\mathscr{L}}$ is the associated homogenized stress. The complex fields are converted to the time domain using the numerical inverse Laplace transform (NILT) method. The NILT method employed in this work is based on Fast Fourier Transform and the ϵ-error algorithm to transform the associate fields from the complex functions to the real valued functions. Details on the numerical inverse has been discussed in Chapter 3.

6 Numerical Verification

A series of simulations were conducted to assess the validity of the proposed high order model and investigate the wave dispersion phenomena induced by micro-heterogeneities. The capability of the high order model is verified against the direct finite element analysis (direct FEA) solution, in which all heterogeneities are fully resolved throughout the macro-domain. The direct FEA simulations use the explicit time integration with time step sizes significantly smaller than the stability limit to ensure high accuracy. The high order method is also compared to the standard 'local' homogenization solution to determine the effects of micro-inertia on the overall responses. The local homogenization includes a two-term asymptotic expansion of the response fields resulting in the IBVP defined in Box 5. The local homogenization solution requires the computation of only the first order influence function, $\mathbf{H}$, which is used to compute the homogenized moduli tensor, $\mathbf{D}^0$.

The examples described below focus on the investigation of microstructural wave dispersions induced only by the contrast of constituent densities since one of the unique contributions of the proposed high order homogenization model is capturing this effect. Using this model, it is also possible to capture wave dispersion phenomena induced by stiffness contrast, or, in more general terms, micro-constituent impedances.

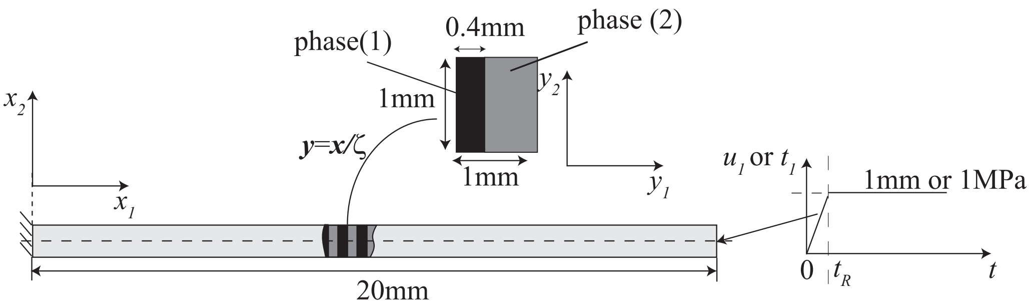

Figure 18: Configuration of the bimaterial bar under ramped step loading.

6.1 Wave Propagation along a Slender Bar

We consider a 2-D bi-material bar subjected to a clamped constraint at its left end and loading at its right end as shown in Fig. 18. The applied loading (displacement or traction) is tensile and along the direction of the bar. The properties of the two constituent phases are chosen as $E^{(1)} = 2$GPa, $\rho^{(1)} = 7090$kg/m^3, $\nu = 0.3$ and $E^{(2)} = 2$GPa, $\rho^{(2)} = 1070$kg/m^3, respectively. The Poisson's ratio of both constituents are set to $\nu = 0.3$.

In the first set of simulations, a displacement controlled ramp loading with the maximum amplitude of 1mm is applied. The time to the maximum displacement is $t_R = 10^{-6}$s. Figure 19 shows the lateral displacement (U_1) versus time from four locations along the center line of the bar at the distance of 2, 5, 10, and 15 mm measured from the fixed end of the bar. The displacement histories for these four points computed using the direct FEA solution and the proposed high order homogenization model are compared. Since the direct FEA solution resolves the microstructure throughout the length of the bar, the reported displacement is the average displacement computed over the microstructure within which the point is located. The large peaks correspond to the traveling macroscopic wave, whereas the oscillations are due to dispersion. The dispersion in the current example (and in many other multi-dimensional problems with a finite domain) is not only due to the microstructural boundaries, but also due to the exterior boundaries. Simulations in the next section attempts to reduce the free boundary effects to isolate the dispersion induced only by density contrast. The displacement recorded closer to the fixed end (e.g. Fig. 19a) remains around the peak applied displacement (i.e. 0.01mm) for a shorter duration than those recorded closer to the free end. This is because the duration for the wave front to travel forth and back (reversing the sign at the fixed end) is shorter when the observation point is closer to the fixed end. All four plots in Fig. 19 demonstrate that

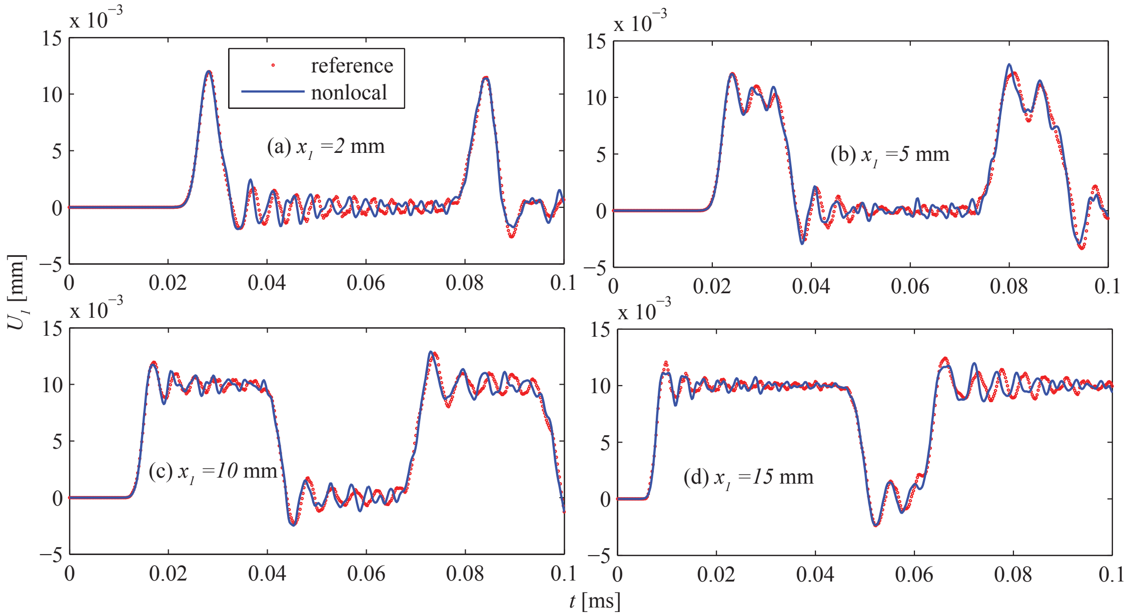

Figure 19: Displacement histories at different positions of the beam.

the proposed high order homogenization model is in very reasonable agreement with the direct FEA solution in capturing the wave dispersions. While the amplitudes of the dispersive waves match very well, a small phase shift is observed particularly in Figs. 19a and 19b. This shift is attributed to a slight error in the propagation velocity change induced by dispersion. Figure 20 illustrates the structural view of the wave propagation through snapshots of the deformed bar at the four different time steps. The propagating wave front indicated by the sharp change in color, the wave dispersion is clearly observed by the changes in an alternating bright and loom pattern immediately following the wavefront.

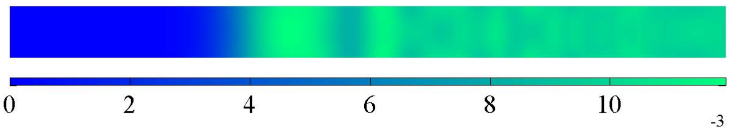

(a) 20μs

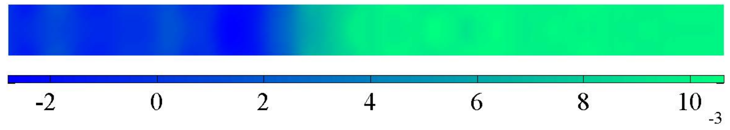

(b) 40μs

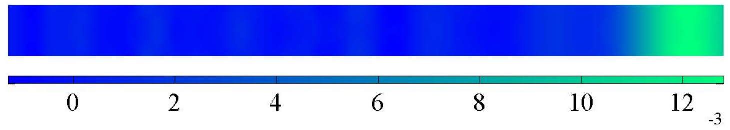

(c) 60μs

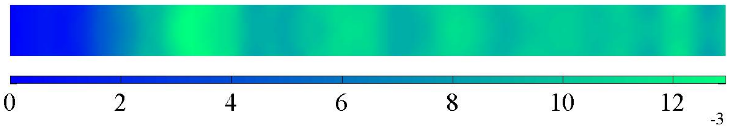

(d) 80μs

Figure 20: Structural view of U_1[mm].

In the second set of simulations, a traction controlled ramp loading with the maximum amplitude of 1MPa is applied. The time to the maximum amplitude loading is $t_R = 10^{-6}$s. The four observation points are the same as the previous set of simulations. Figure 21 shows the lateral displacement (U_1) versus time from the four locations computed by the high order homogenization model and the direct FEA solution. The predictions given by the high order model are very similar to the direct FEA solution, demonstrating that the high order homogenization works well with the traction boundary condition as well.

6.2 Wave Propagation in a Square Composite Medium

The second example considers the dynamic response of a two-dimensional square heterogeneous medium with a layered configuration. In this example, the effect of

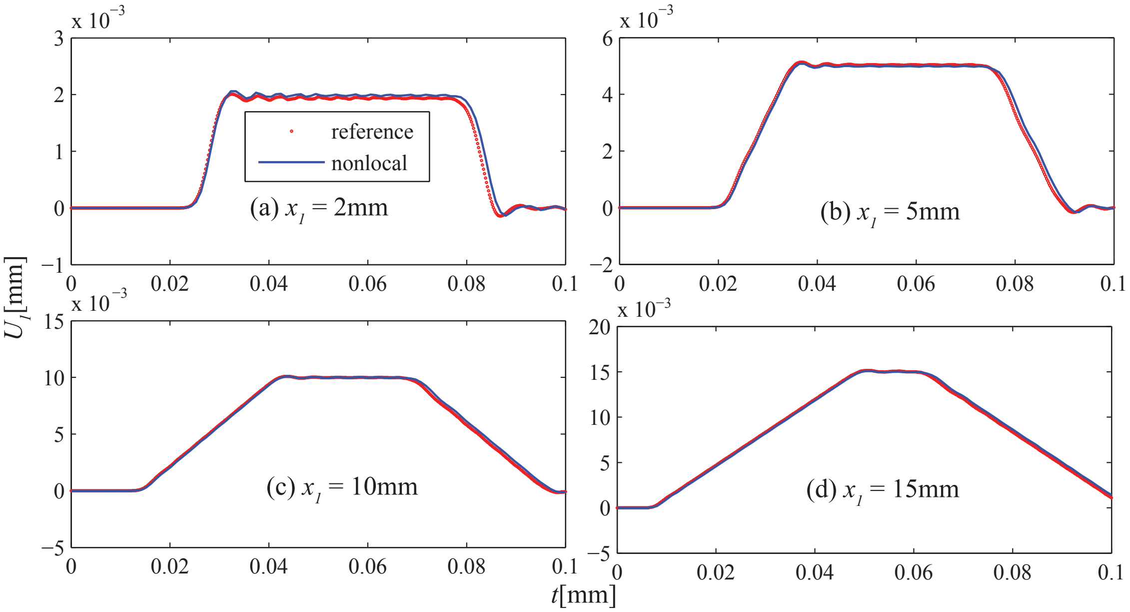

Figure 21: Displacement histories at different positions of the beam.

loading frequency on the wave propagation characteristics is investigated. Two cases of wave propagation are considered as illustrated in Fig. 22. In the first set of simulations, the domain is clamped at the left edge and subjected to the displacement controlled sinusoidal stimulation at the middle of the right edge. The maximum amplitude of the loading is $u_R = 0.01$mm. The shape of the domain is chosen so that the effect of boundary dispersion is relatively small compared to the dispersion induced by the microstructure. The material properties of the layers are identical to those presented in Section 6.1. The time duration of the simulations is $t_0 = 500$ μs. The total number of load cycles within the duration of the simulation is denoted as N ($= t_0/t_R$). For comparison purposes, the wavelength is approximated using the p-wave speed ($= \sqrt{(\lambda_0 + 2\mu_0)/\rho_0}$, where λ_0 and μ_0 are the homogenized Lamé constants respectively and ρ_0 the homogenized density of the microstructure). The approximate wavelengths for N=2, 12, and 38 are 12, 3.5 and 1.1 times the microstructural size (=10 mm) respectively.

The high order homogenization, direct FEA, and the local homogenization solutions are compared in Fig. 23 for $N = 2$. The displacement contours within the

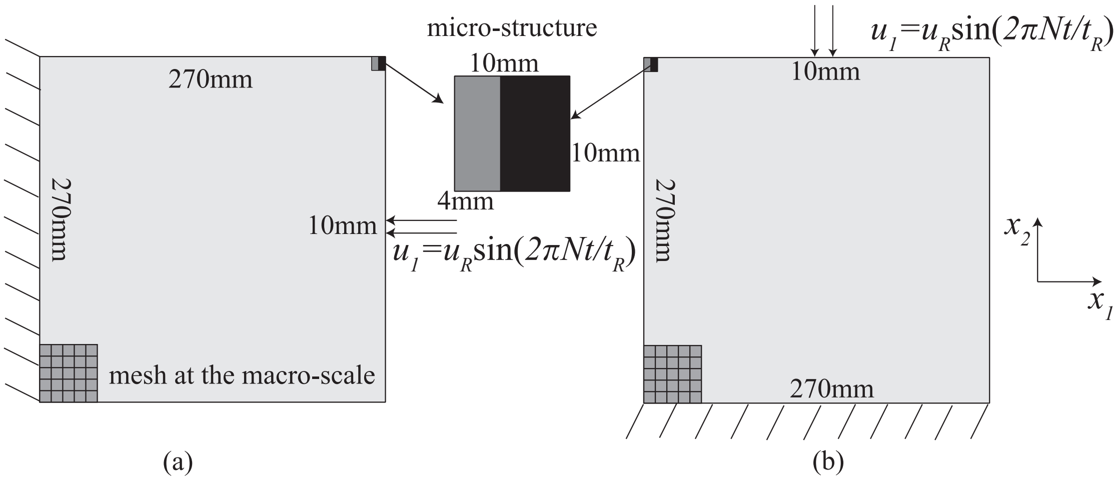

Figure 22: Configuration of the composite square under sinusoidal loading conditions: (a) wave imparted along the direction perpendicular to the layers; (b) wave imparted along the direction parallel to the layers.

problem domain are plotted at four time instances (i.e., $t = 100$, 200, 300 and 400 μs). The high order homogenization, local homogenization and the direct FEA solutions provide near identical displacement profiles throughout the loading history. The similarity between the high order and local homogenization results indicates that the microstructural inhomogeneities have little influence on the structural response. When $N = 2$, the length of the propagating wave is large enough that the dispersion due to micro-heterogeneities (i.e. the density contrast) is negligible.

Figure 24 shows the comparison of the solutions computed by the proposed high order homogenization approach, the local homogenization and the direct FEA when $N = 12$. In these simulations, the wavelength is approximately 3.5 times the size of the microstructure. The displacement profiles of the high order and local homogenization models start to deviate from each other, pointing to the presence of dispersive waves. The displacement profiles computed using the direct FEA show some deviation from the results of the high order homogenization model. While the high order homogenization model point to the localization of the wave propagation towards the center line, the direct FEA model predicts localization of the wave along two angled paths, in addition to the center line. We speculate that the angled paths are due

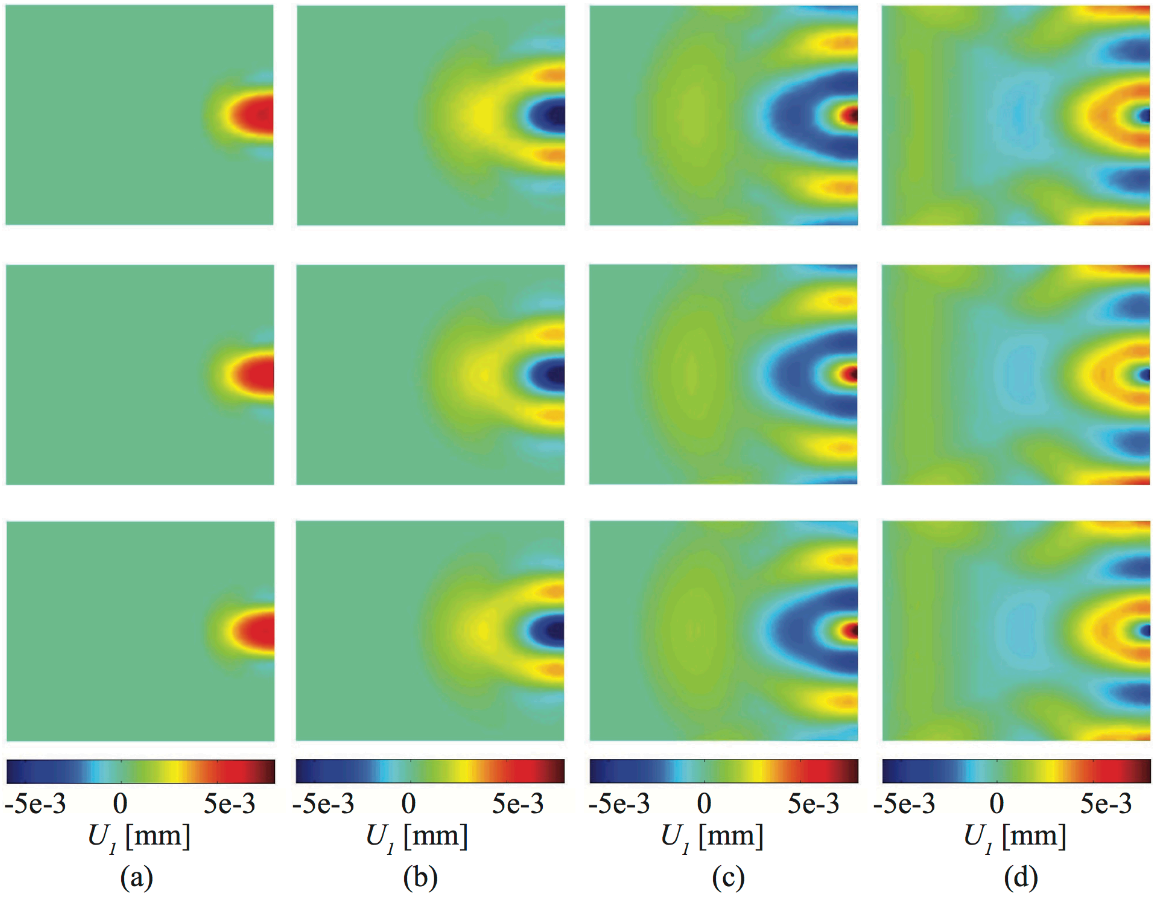

Figure 23: High order homogenization (top row), direct FEA (middle row) and the local homogenization (bottom row) solutions when $N = 2$: (a) $t = 100\mu s$; (b) $t = 200\mu s$; (c) $t = 300\mu s$; and (d) $t = 400\mu s$.

to the interaction effects between the external boundary and the layered microstructure. The discrepancy between the displacement profiles are therefore attributed to difficulty in capturing this interaction effect using the homogenization models.

The high order homogenization, the local homogenization and the direct FEA solutions for $N = 38$ are summarized in Fig. 25. In this case, the wavelength is 1.1 times the microstructure size. The high order homogenization model shows that the wave quickly attenuates, suggesting phononic stop band behavior. In contrast, the direct FEA and the local homogenization solutions display wave propagation in the media. The wave attenuation leading to the stop band behavior is due to the imaginary component of wavenumber [6]. The direct FEA method considers only

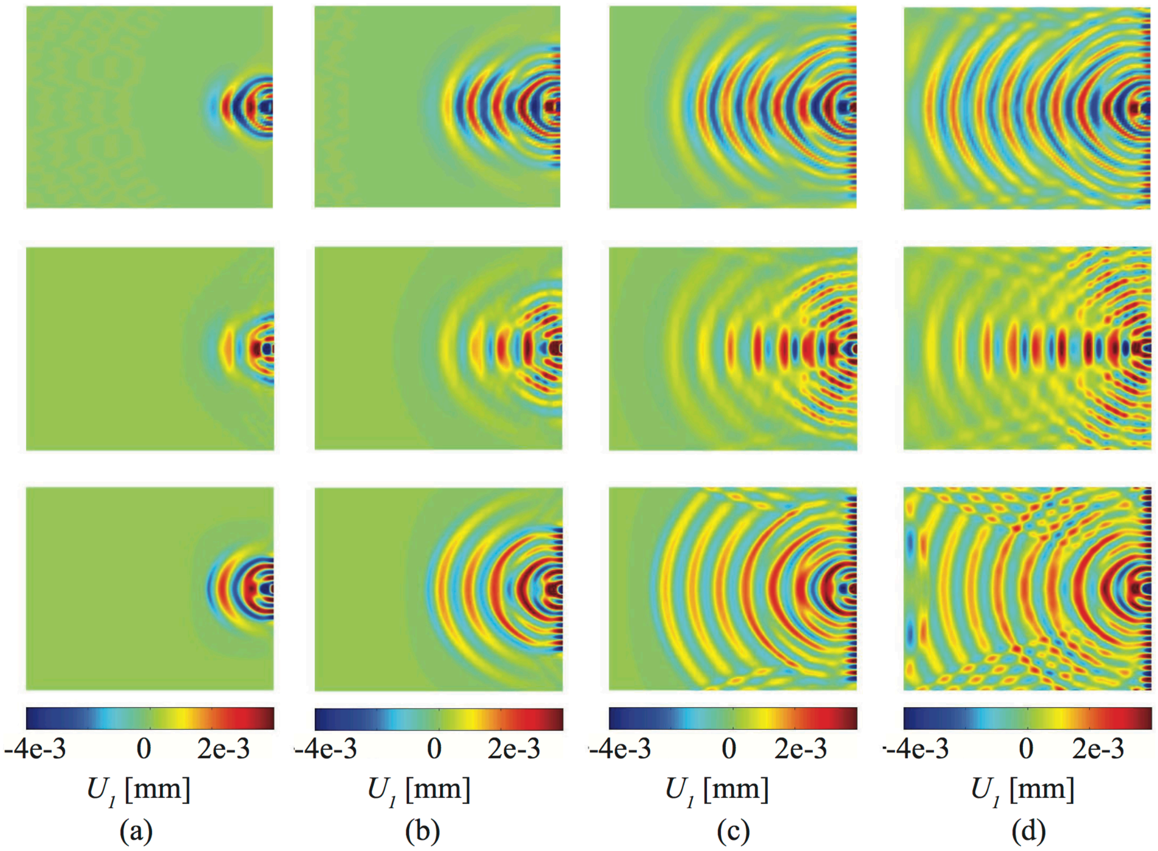

(a) (b) (c) (d)

Figure 24: High order homogenization (top row), direct FEA (middle row) and the local homogenization (bottom row) solutions when $N = 12$: (a) $t = 100\mu$s; (b) $t = 200\mu$s; (c) $t = 300\mu$s; and (d) $t = 400\mu$s.

the real components of the wavenumber, and therefore cannot capture the stop band behavior. The hybrid Laplace Transform-Finite Element method employed in the evaluation of the high order homogenization model retains the imaginary component of the response, and able to simulate the stop band behavior. The wave attenuation due to the complex wave properties is included in the solution in the Laplace domain. The theoretical model proposed by Andrianov et al. [6] was used to estimate the onset of the stop band, computed as the wave frequency that leads to zero group velocity. The theoretical estimate of $N = 38$ verifies that the proposed model is reasonably accurate in predicting the onset of the stop band behavior.

In the second set of simulations, the domain is clamped at the bottom edge and subjected to the displacement controlled sinusoidal stimulation at the middle

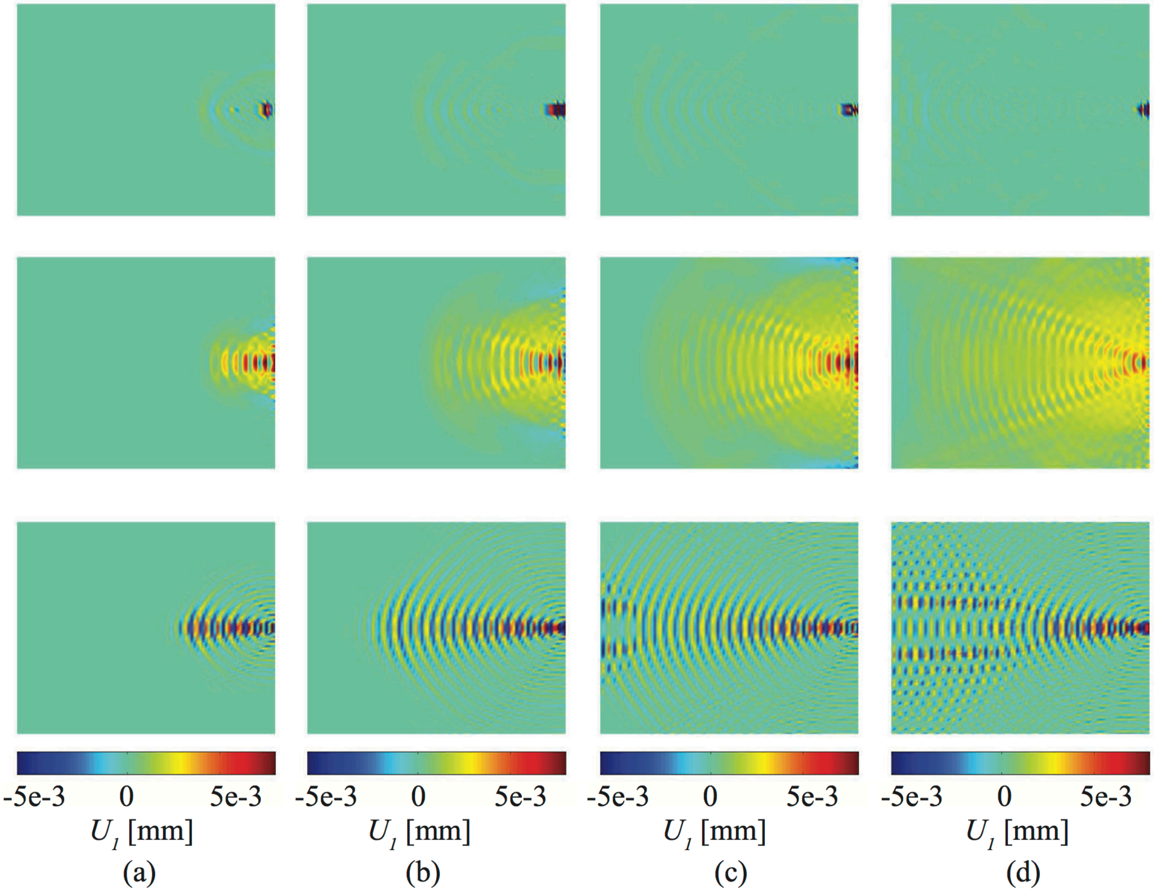

Figure 25: High order homogenization (top row), direct FEA (middle row) and the local homogenization (bottom row) solutions when $N = 38$: (a) $t = 100\mu$s; (b) $t = 200\mu$s; (c) $t = 300\mu$s; and (d) $t = 400\mu$s.

of the top edge as illustrated in Fig. 22b. The maximum amplitude of the loading is $u_R = 0.01$mm. In this example, the wave is imparted along the vertical direction, whereas the microstructure-induced dispersion impart waves along the horizontal direction. The time duration of the simulations is $t_0 = 500\mu s$. For comparison purposes, the wavelength is approximated using the shear wave speed ($= \sqrt{\mu_0/\rho_0}$). The calculated wavelengths are 10, 1.4 and 0.8 times the microstructure size for $N = 2$, 15, and 25 cases, respectively.

Figure 26 compares the displacement contours computed by the high order, the direct FEA and local homogenization models for $N = 2$. Similar to the previous set of simulations (i.e., Fig. 23), the high order homogenization, local homogenization and the direct FEA solutions provide near identical displacement profiles throughout the loading history for long wavelengths.

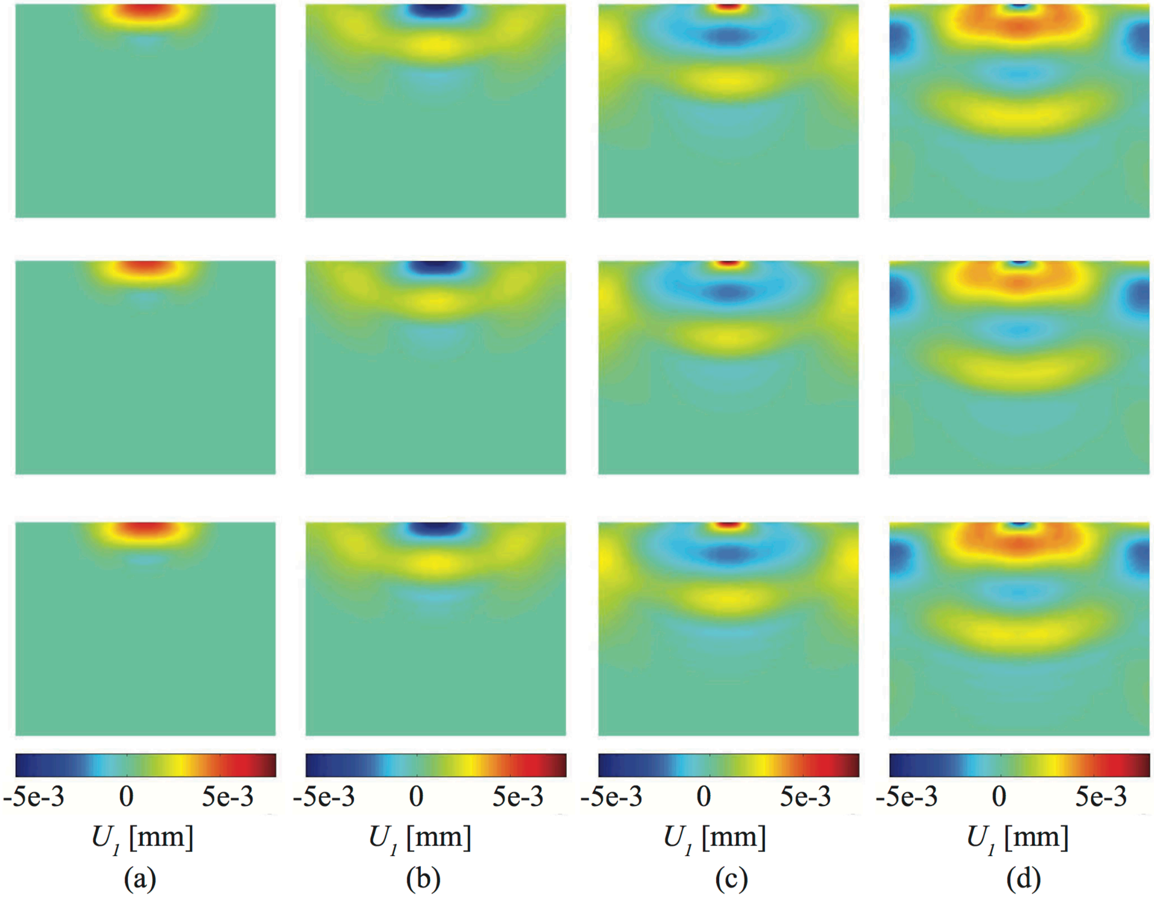

Figure 26: High order homogenization (top row), direct FEA (middle row) and the local homogenization (bottom row) solutions when $N = 2$: (a) $t = 100\mu$s; (b) $t = 200\mu$s; (c) $t = 300\mu$s; and (d) $t = 400\mu$s.

Figure 27 shows the comparison of the solutions computed by the proposed approach, the direct FEA and the local homogenization method when $N = 15$. The displacement profiles suggest that the group velocity computed by the high order homogenization and the direct FEA models is markedly lower than the local homogenization solution, indicating the effect of dispersion induced by micro-inertia. The amount of slowdown computed by the high order homogenization and the direct FEA models are similar notwithstanding some dissimilarities between the wave patterns.

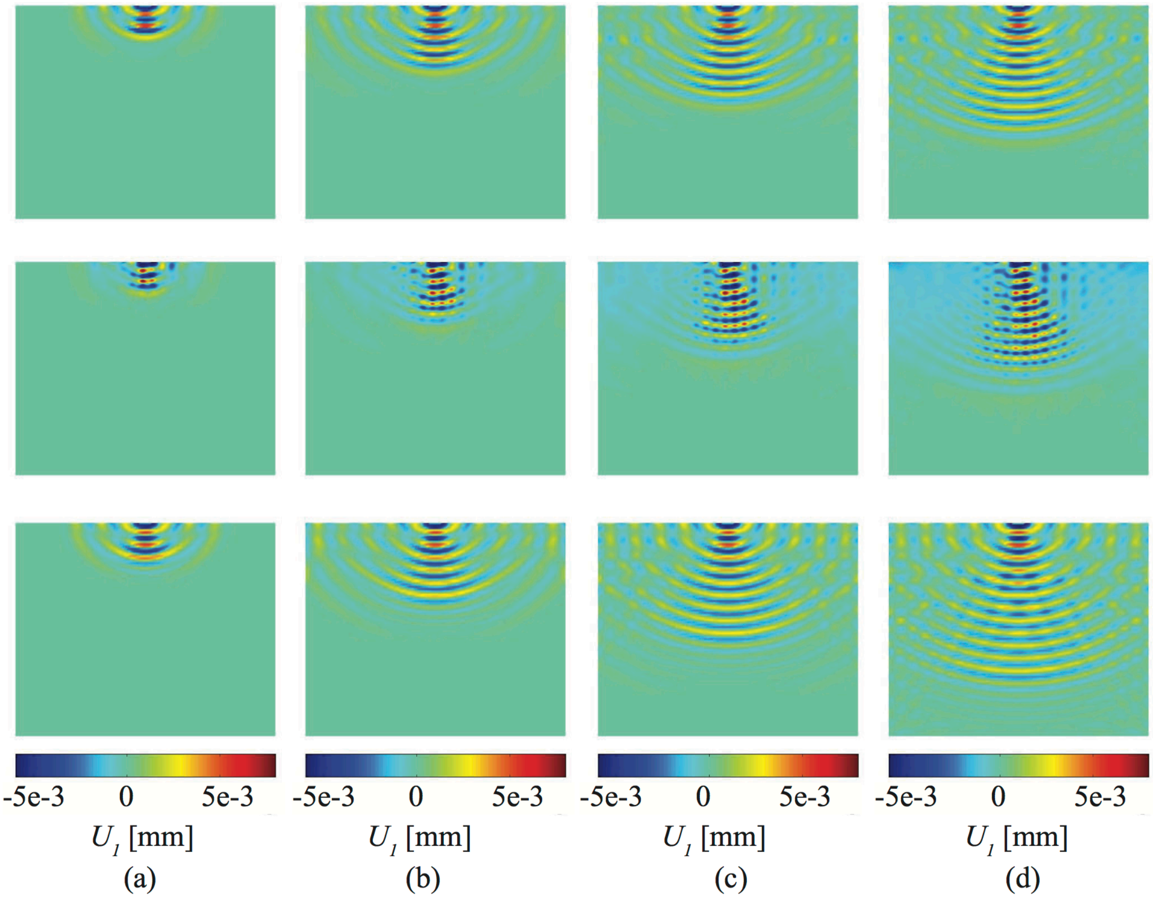

Figure 27: High order homogenization (top row), direct FEA (middle row) and the local homogenization (bottom row) solutions when $N = 15$: (a) $t = 100\mu$s; (b) $t = 200\mu$s; (c) $t = 300\mu$s; and (d) $t = 400\mu$s.

When the applied displacement frequency is further increased ($N = 25$), the high order homogenization model predicts the onset of the phononic stop band and the wave ceases to propagate significantly along the lateral direction. The comparison of the displacement profiles computed by the three models is shown in Fig. 28. The local homogenization model display no effect of dispersion in this case and the wave propagation characteristics are similar to the $N = 15$ case. The direct FEA and the high order homogenization models predict that the displacement wave continues to propagate along the vertical direction within a narrow band of uniform material immediately under the prescribed boundary. The displacement profiles computed using the high order homogenization model and the direct FEA simulations are in

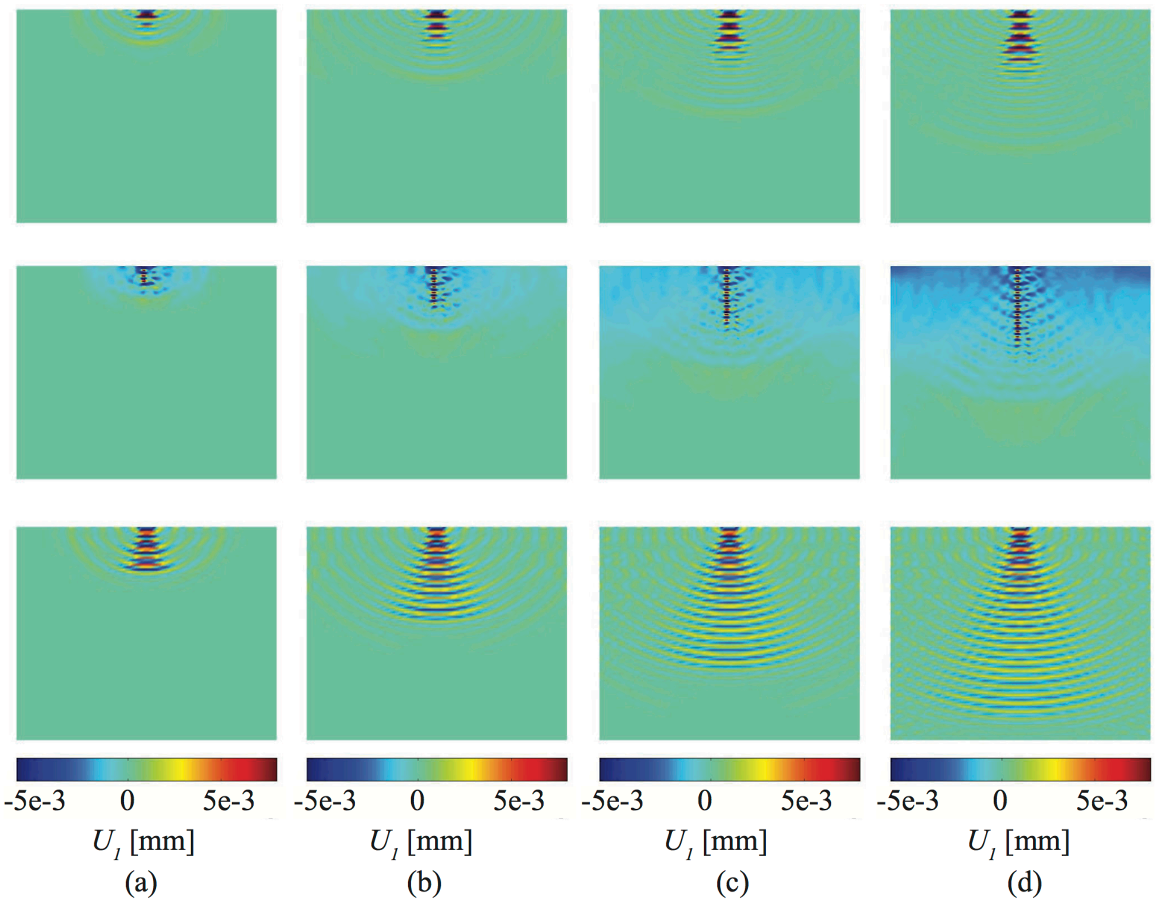

Figure 28: High order homogenization (top row), direct FEA (middle row) and the local homogenization (bottom row) solutions when $N = 25$: (a) $t = 100\mu$s; (b) $t = 200\mu$s; (c) $t = 300\mu$s; and (d) $t = 400\mu$s.

reasonable agreement with each other. The lateral wave propagation (i.e., along the x_1-direction) is almost completely suppressed in the high order homogenization model. In contrast, the direct FEA simulations reveal lateral propagation since this model cannot capture the behavior within the stop bands as described above.

6.3 Computational Efficiency

The computational efficiency is significantly improved using the high order homogenization model compared to the direct finite element simulation. The homogenization contributes to the computational performance. In the second numerical example, 2916 elements are used in the discretization of the macroscopic problem by the high order homogenization model, while 18225 elements are used to discretize the domain using the direct finite element simulation. The direct simulation needs many more elements to mesh the composite microstructures particularly when there is a large discrepancy between the sizes of micro- and macrostructure. Meshing the macroscopic model using the high order homogenization homogenization is independent of microstructures since the macrostructure is solved using a homogenization model. The computation of the microstructural properties is required but only for once and off-line, so that it doesn't contribute to the computational complexity of the structural analysis.

In addition, solving the problem in the Laplace domain took 500 steps of computation by the high order homogenization model while at least 10000 time steps are required to guarantee the computational precision by the direct FEA solution. The Laplace transform converts the problem from the time domain to a complex frequency domain where as long as sufficient frequencies are captured, the solution is solved accurately. The direct FEA solution which uses the finite difference method has to make each time step small enough to remain stable and retain high accuracy. In many problems, the number of frequencies required is much smaller than the number of time steps required for stable computations.

7 Conclusions

A finite element based high order homogenization model was proposed for multi-dimensional wave propagation in elastic composite structures. The proposed model was derived based on the mathematical homogenization with multiple spatial scales. The higher order equilibrium terms in the asymptotic expansion were introduced to capture the micro-inertia effects caused by micro-heterogeneities. The finite element formulation for the evaluation of the microscale influence functions and the homogenized model were provided. In addition, the model is capable of predicting the wave propagation in stopbands due to the complex calculation of the homogenized problem in the Laplace domain where complex wavenumber is calculated.

The generality of problem definitions extends the application of the proposed model. The high order homogenization model is capable of accounting complete microscopic impedances (i.e. due to density and modulus) and arbitrary microstructures and capturing the wave propagation in stopbands. Next, we intend to solve multi-dimensional wave propagation in viscoelastic composites. Recall the one-dimensional wave solution in Chapter 3, the homogenization actually has already been demonstrated in viscoelastic composite structures. The simulation of multi-dimensional wave propagation in viscoelastic composites would be as the similar practice for one-dimensional wave propagation in Chapter 3 where the homogenization is implemented in the Laplace domain.

CHAPTER 5

MULTISCALE MODELING OF MULTI-DIMENSIONAL WAVE PROPAGATION IN VISCOELASTIC COMPOSITE STRUCTURES

1 Introduction

Wave propagation in viscoelastic composite materials is of particular interest since wave can be attenuated by both viscous dissipation and bandgap. The work regarding wave dispersion in viscoelastic composites is scarce compared to elastic problems, and most of them focuses on layered or lattice structures [2, 48, 49, 73, 74] where analytical solutions can be derived. The literature on bandgap in viscoelastic composites is even more limited. Zhao and Wei [83] studied the bandgap of one-dimensional phononic crystal with viscoelastic host material using the Bloch-Floquet wave solution. Moiseyenko and Laude [46] investigated the influence of material loss on the complex band structure of two-dimensional phononic crystals by incorporating viscoelastic constitutive model in the extended plane-wave expansion. Psarobas [59] discussed the effect of viscoelastic losses in a high-density contrast sonic bandgap material of closed packed rubber sphere in air. Merheb et al. [44] provided a theoretical and experimental study of rubber/air acoustic bandgap structures. Oh et al. [53] investigated wave attenuation and dissipation mechanisms in viscoelastic phononic crystals having different inclusion types in a long-wavelength regime. Hui and Oskay [39] showed the bangap in an one-dimensional viscoelastic composite using a semi-analytical solution based on the multiscale homogenization theory. This work helps to elucidate the possibility of the high order homogenization model applied in viscoelastic materials. However, a computational solution needs to be sought to describe multi-dimensional wave propagation in viscoelastic composites due to the complexity of problem definitions.

In this chapter, a complex high order homogenization model defined in the Laplace domain is proposed. This model is based on the high order computational homogenization approach for elastic composites introduced in Chapter 4, and the homogenization procedure is developed in the Laplace domain. In particular, the major contribution of this work is that the proposed approach leads to a numerical model that can capture wave dispersion and bandgap for multi-dimensional wave propagation in viscoelastic composites. The numerical examples are presented and compared to the finite element solution and the analytical solution for verification. The material dissipation and wave dispersion induced wave attenuations are compared by investigating the dissipated energy in the problem domain.

2 Problem Setting

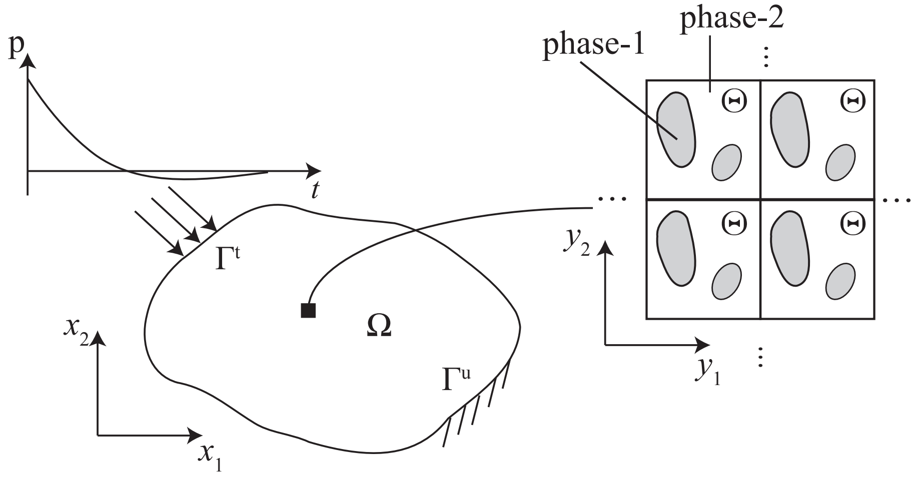

Figure 29: Schematic representation of multiscale problems.

The illustrative description of multiscale problems is provided in Fig. 29. In the time domain, the equation of motion for dynamic problems is defined as:

$$\sigma^{\zeta}_{ij,j}(\mathbf{x},t) = \rho^{\zeta}(\mathbf{x})\ddot{u}^{\zeta}_i(\mathbf{x},t) \tag{202}$$

where $\boldsymbol{\sigma}^{\zeta}$ denotes the stress tensor, ρ^{ζ} the density, and $\mathbf{u}^{\zeta}$ the displacement vector.

The superscript ζ represents the dependency of the response fields on microscopic properties; $\mathbf{x}$ denotes the spatial coordinate vector. The linear viscoelastic model is generalized as a hereditary integral:

$$\sigma_{ij}^{\zeta}(\mathbf{x},t) = \int_0^t g_{ijkl}^{\zeta}(\mathbf{x},t-\tau)\dot{\epsilon}_{kl}^{\zeta}(\mathbf{x},\tau)d\tau \tag{203}$$

where, the superscript ζ denotes the dependency of response fields on microstructural heterogeneities; dot represents the derivative with respect to the time variable. For linear viscoelastic materials, $\mathbf{g}^{\zeta}$ is termed the relaxation moduli and dependent of the time variable. For linear elastic materials, $\mathbf{g}^{\zeta}$ is reduced to be independent of the time variable. $\boldsymbol{\epsilon}^{\zeta}$ is the strain tensor. Under the assumption of small deformation:

$$\epsilon_{ij}^{\zeta}(\mathbf{x},t) = \frac{1}{2}\left(u_{i,j}^{\zeta}(\mathbf{x},t) + u_{j,i}^{\zeta}(\mathbf{x},t)\right) \tag{204}$$

where comma denotes the derivative with respect to $\mathbf{x}$. The boundary conditions are described as:

$$u_i^{\zeta}(\mathbf{x},t) = \bar{u}_i(\mathbf{x},t); \quad \mathbf{x} \in \Gamma^u \tag{205a}$$

$$\sigma_{ij}^{\zeta}(\mathbf{x},t)n_j = \bar{t}_i(\mathbf{x},t); \quad \mathbf{x} \in \Gamma^t \tag{205b}$$

where $\mathbf{n}$ is the outward unit normal vector along the traction boundaries. $\bar{\mathbf{u}}(\mathbf{x},t)$ and $\bar{\mathbf{t}}(\mathbf{x},t)$ denote the prescribed displacement and traction vectors on Γ^u and Γ^t, respectively. The boundary conditions are defined such that $\Gamma \equiv \partial\Omega = \Gamma^u \cup \Gamma^t$; $\Gamma^u \cap \Gamma^t = \emptyset$. Stationary initial conditions are used in this work:

$$u_i^{\zeta}(\mathbf{x},0) \equiv \hat{u}_i(\mathbf{x}) = 0; \quad \mathbf{x} \in \Omega \tag{206a}$$

$$\dot{u_i}^{\zeta}(\mathbf{x},0) \equiv \hat{v}_i(\mathbf{x}) = 0; \quad \mathbf{x} \in \Omega \tag{206b}$$

$\hat{\mathbf{u}}$ and $\hat{\mathbf{v}}$ denote the initial displacement and velocity data, respectively and Ω is the open boundary domain.

The viscoelastic constitutive relation in the time domain is in an integral form, and is transformed to a linear form in the Laplace domain. The Laplace transform of an arbitrary, real valued, time varying function f is defined as:

$$\mathscr{F}(s) \equiv \mathscr{L}(f(t)) = \int_0^\infty e^{-st} f(t)dt \tag{207}$$

where, the Laplace argument s and the transformed function $\mathscr{F}$ are complex valued. The derivative rule for the Laplace transform is given as:

$$\mathscr{L}(f\underbrace{,tt\ldots t}_{n\text{ times}}(t)) = s^n\mathscr{F}(s) - s^{n-1}f(0) - \ldots - f\underbrace{,tt\ldots t}_{n-1\text{ times}}(0) \tag{208}$$

and the convolution integral rule is given as:

$$\mathscr{L}\left(\int_0^t f_1(t-\xi)f_2(\xi)d\xi\right) = \mathscr{L}\left(\int_0^t f_1(\xi)f_2(t-\xi)d\xi\right) = \mathscr{L}(f_1)\mathscr{L}(f_2) \tag{209}$$

Applying Eq. 209 to Eq. 203, the constitutive equation in the time domain is transformed to the linear form in the Laplace domain:

$$\sigma_{ij}^{\zeta}(\mathbf{x}, s) = C_{ijkl}^{\zeta}(\mathbf{x}, s)\epsilon_{kl}^{\zeta}(\mathbf{x}, s) \tag{210}$$

where $\mathbf{C}^{\zeta}$ is the material constant tensor in the Laplace domain depending on the spatial coordinates, $\mathbf{x}$ and the complex argument, s. The equation of motion in the Laplace domain is obtained by applying Eq. 207 to Eq. 202 using Eq. 208 and considering the stationary initial conditions:

$$\sigma_{ij,j}^{\zeta}(\mathbf{x}, s) = \rho^{\zeta}(\mathbf{x})s^2 {u_i}^{\zeta}(\mathbf{x}, s) \tag{211}$$

and the equation of deformation becomes:

$$\epsilon^{\zeta}_{ij}(\mathbf{x}, s) = \frac{1}{2}\left(u^{\zeta}_{i,j}(\mathbf{x}, s) + u^{\zeta}_{j,i}(\mathbf{x}, s)\right) \tag{212}$$

The boundary conditions are:

$$u^{\zeta}_{i}(\mathbf{x}, s) = \bar{u}_i(\mathbf{x}, s); \quad \mathbf{x} \in \Gamma^u \tag{213a}$$

$$\sigma^{\zeta}_{ij}(\mathbf{x}, s)n_j = \bar{t}_i(\mathbf{x}, s); \quad \mathbf{x} \in \Gamma^t \tag{213b}$$

where $\bar{\mathbf{u}}(\mathbf{x}, s)$ and $\bar{\mathbf{t}}(\mathbf{x}, s)$ are the prescribed displacement and traction boundary conditions in the Laplace domain.

3 Mathematical Homogenization

In this section, the mathematical homogenization of the multiscale problem is proposed in the Laplace domain. The two spatial scales, $\mathbf{x}$ and $\mathbf{y}$, are considered in solving the boundary value problem in the Laplace domain as depicted by Eqs. 210-213. $\mathbf{x}$ and $\mathbf{y}$ represent the coordinate vectors at the macro- and microscale, respectively. The two vectors correlate with each other by $\mathbf{y} = \mathbf{x}/\zeta$, where ζ is the scaling factor $(0 < \zeta < 1)$. The physical meaning of the scaling factor is the ratio of the size of microstructures to the wavelength of propagating waves.

Define an arbitrary function in the time domain as $f^{\zeta}(\mathbf{x}, t)$, its representation in the Laplace domain is denoted as $f^{\zeta}(\mathbf{x}, s)$. Here, the homogenization theory is applied in the Laplace domain where the complex function $f^{\zeta}(\mathbf{x}, s)$ is dependent on the two spatial scales:

$$f(\mathbf{x}, \mathbf{y}(\mathbf{x}), s) = f^{\zeta}(\mathbf{x}, s) \tag{214}$$

The spatial derivative of f^ζ is computed using the chain rule:

$$f^\zeta_{,x_i}(\mathbf{x},s) = f_{,x_i}(\mathbf{x},\mathbf{y},s) + \frac{1}{\zeta} f_{,y_i}(\mathbf{x},\mathbf{y},s) \tag{215}$$

where comma denotes the derivative with respect to each coordinate variable.

All the response fields are assumed to be spatially periodic over the characteristic volume throughout the deformation process:

$$f(\mathbf{x},\mathbf{y},s) = f(\mathbf{x},\mathbf{y}+\mathbf{k}\hat{\mathbf{y}},s) \tag{216}$$

where $\hat{\mathbf{y}}$ denotes the period of microstructure; and $\mathbf{k}$ is a $n_{\mathrm{sd}} \times n_{\mathrm{sd}}$ diagonal matrix with integer components.

The traditional homogenization procedure which applies in the time domain searches displacements as an asymptotic expansion with respect to the scaling factor, ζ. Apply the Laplace transform on the displacement expansion in the time domain, the displacement expansion in the Laplace domain is directly obtained as:

$$u_i^\zeta(\mathbf{x},s) = u_i(\mathbf{x},\mathbf{y},s) = u_i^0(\mathbf{x},s) + \zeta u_i^1(\mathbf{x},\mathbf{y},s) + \zeta^2 u_i^2(\mathbf{x},\mathbf{y},s) + \zeta^3 u_i^3(\mathbf{x},\mathbf{y},s) + O(\zeta^4) \tag{217}$$

The physical meaning of the scaling factor, ζ, is retained since the Laplace transform only performs on the time variable. The leading order displacement term, $\mathbf{u}^0$, is a function of the macroscopic coordinate vector $\mathbf{x}$ only, and the higher order displacement terms depend on both $\mathbf{x}$ and $\mathbf{y}$. The linearity of the deformation equation suggests the strain expansion as:

$$\epsilon_{ij}(\mathbf{x},\mathbf{y},s) = \epsilon_{ij}^0(\mathbf{x},\mathbf{y},s) + \zeta\epsilon_{ij}^1(\mathbf{x},\mathbf{y},s) + \zeta^2\epsilon_{ij}^2(\mathbf{x},\mathbf{y},s) + O(\zeta^3) \tag{218}$$

where the strains at each order of ζ are expressed as:

$$\epsilon_{ij}^{\alpha}(\mathbf{x},\mathbf{y},s) = e_{xij}(\mathbf{u}^{\alpha}(\mathbf{x},\mathbf{y},s)) + e_{yij}(\mathbf{u}^{\alpha+1}(\mathbf{x},\mathbf{y},s)); \quad \alpha = 0,1,2\ldots \tag{219}$$

$$e_{\xi ij}(\mathbf{u}^{\alpha}) = u_{(i,\xi_j)}^{\alpha}(\mathbf{x},\mathbf{y},s) = \frac{1}{2}\left(u_{i,\xi_j}^{\alpha}(\mathbf{x},\mathbf{y},s) + u_{j,\xi_i}^{\alpha}(\mathbf{x},\mathbf{y},s)\right); \quad \xi = x,y \tag{220}$$

Substituting Eq. 218 into Eq. 210, the stress expansion is obtained:

$$\sigma_{ij}(\mathbf{x},\mathbf{y},s) = \sigma_{ij}^{0}(\mathbf{x},\mathbf{y},s) + \zeta\sigma_{ij}^{1}(\mathbf{x},\mathbf{y},s) + \zeta^2\sigma_{ij}^{2}(\mathbf{x},\mathbf{y},s) + O(\zeta^3) \tag{221}$$

where the stress component at each order of ζ is expressed as:

$$\sigma_{ij}^{\alpha}(\mathbf{x},\mathbf{y},s) = C_{ijkl}(\mathbf{y},s)\epsilon_{kl}^{\alpha}(\mathbf{x},\mathbf{y},s); \quad \alpha = 0,1,2,\ldots \tag{222}$$

Due to the periodic assumption of microstructures in the problem domain, elastic moduli and density depend on the microscopic coordinate vector, $\mathbf{y}$, only (i.e. $\rho^{\zeta}(\mathbf{x}) = \rho(\mathbf{y})$ and $\mathbf{C}^{\zeta}(\mathbf{x}) = \mathbf{C}(\mathbf{y})$). Substituting Eqs. 217 and 221 to Eq. 211, the coefficients in the asymptotic expansion construct the equilibrium equations with respect to the ascending order of ζ:

$$O(\zeta^{-1}): \quad \sigma_{ij,y_j}^{0}(\mathbf{x},\mathbf{y},s) = 0 \tag{223a}$$

$$O(1): \quad \sigma_{ij,x_j}^{0}(\mathbf{x},\mathbf{y},s) + \sigma_{ij,y_j}^{1}(\mathbf{x},\mathbf{y},s) = \rho(\mathbf{y})u_i^{0}(\mathbf{x},s)s^2 \tag{223b}$$

$$O(\zeta): \quad \sigma_{ij,x_j}^{1}(\mathbf{x},\mathbf{y},s) + \sigma_{ij,y_j}^{2}(\mathbf{x},\mathbf{y},s) = \rho(\mathbf{y})u_i^{1}(\mathbf{x},\mathbf{y},s)s^2 \tag{223c}$$

$$O(\zeta^2): \quad \sigma_{ij,x_j}^{2}(\mathbf{x},\mathbf{y},s) + \sigma_{ij,y_j}^{3}(\mathbf{x},\mathbf{y},s) = \rho(\mathbf{y})u_i^{2}(\mathbf{x},\mathbf{y},s)s^2 \tag{223d}$$

To involve wave dispersions at the microscale in the homogenized solution, the high order equilibrium equations (i.e., O(ζ) and O(ζ^2)) need to be incorporated. Since the homogenization only applies on the spatial scales, $\mathbf{x}$ and $\mathbf{y}$, the Laplace transform does not change the homogenization procedure compared to the homogenization in the time domain which has been extensively discussed in Chapter 4. In this section, the principal equations are provided for completeness.

3.1 Homogenization Procedure

The first order displacement term, $\mathbf{u}^1$, as a function of both $\mathbf{x}$ and $\mathbf{y}$, is expressed in the following form by taking the linear separation of variables:

$$u_i^1(\mathbf{x}, \mathbf{y}, s) = U_i^1(\mathbf{x}, s) + H_{ikl}(\mathbf{y}, s) e_{xkl}(\mathbf{u}^0(\mathbf{x}, s)) \tag{224}$$

where $\mathbf{H}$ is the first order influence function at the microscale and it is a 3^{rd} rank tensor with the symmetry on the second and third indices (i.e. $H_{ikl} = H_{ilk}$). The microscopic equation of motion is derived by substituting Eq. 224 to Eq. 223a as:

$$\left\{C_{ijkl}(\mathbf{y}, s)(h_{klmn}(\mathbf{y}, s) + I_{klmn})\right\}_{,y_j} = 0; \quad \mathbf{y} \in \Theta \tag{225}$$

in which $h_{ijmn}(\mathbf{y}, s) = H_{(i,y_j)mn}(\mathbf{y}, s)$ is the polarization function. The local periodicity of the first order displacement term, $\mathbf{u}^1$, leads to the periodic first order influence function. In addition, the normalization is used to enforce the unique solution of $\mathbf{H}$:

$$\langle H_{ikl}(\mathbf{y}, s) \rangle = \frac{1}{|\Theta|} \int_\Theta H_{ikl}(\mathbf{y}, s) d\mathbf{y} = 0 \tag{226}$$

in which $\langle \cdot \rangle = \dfrac{1}{|\Theta|} \displaystyle\int_\Theta \cdot \, d\mathbf{y}$ denotes the averaging operator, and $|\Theta|$ is the volume of Θ. By ensuring that the average of the influence function vanishes, the rigid body modes are eliminated from the solution. Eqs. 225 and 226 together with the periodic boundary conditions will uniquely determine the value of $\mathbf{H}$

The homogenized equation of motion at $O(1)$ is obtained by applying the averaging operator on Eq. 223b and exploiting the local periodicity of $\boldsymbol{\sigma}^1$:

$$\rho_0 u_i^0(\mathbf{x}, s)s^2 = D_{ijmn}^0(s)e_{xmn}(\mathbf{u}^0)_{,x_j}; \quad \mathbf{x} \in \Omega \tag{227}$$

where $\rho_0 = \langle \rho \rangle$ is the volume-averaged density; and

$$D_{ijmn}^0(s) = \langle C_{ijmn}^0(\mathbf{y}, s) \rangle \tag{228}$$

$$C_{ijmn}^0(\mathbf{y}, s) = C_{ijkl}(\mathbf{y}, s)(h_{klmn}(\mathbf{y}, s) + I_{klmn}) \tag{229}$$

in which, $\mathbf{D}^0$ is the zeroth order homogenized modulus tensor in the Laplace domain and $\mathbf{I}$ the fourth rank identity tensor.

For the homogenization at $O(\zeta)$, $\mathbf{u}^2$, is approximated by introducing the second order influence function, $\mathbf{P}(\mathbf{y}, s)$ as:

$$u_i^2(\mathbf{x}, \mathbf{y}, s) = U_i^2(\mathbf{x}, s) + H_{ikl}(\mathbf{y}, s)e_{xkl}(\mathbf{U}^1) + P_{ijkl}(\mathbf{y}, s)e_{xkl}(\mathbf{u}^0)_{,x_j} \tag{230}$$

in which $\mathbf{P}$ is a fourth rank tensor and symmetric with respect to the last two indices, but not necessarily with respect to the first two indices (i.e., $P_{ijkl} \neq P_{jikl}$ and $P_{ijkl} \neq P_{klij}$) for arbitrary microstructural configurations. Substituting Eq. 230 into Eq. 223b and considering Eq. 230, the microscopic equation of motion at $O(\zeta^0)$ solving for $\mathbf{P}$ is derived as:

$$C_{ijpmn,y_j}^1 = \theta(\mathbf{y})D_{ipmn}^0(s) - C_{ipmn}^0(\mathbf{y}, s); \quad \mathbf{y} \in \Theta \tag{231}$$

and

$$C_{ijpmn}^1(\mathbf{y}, s) = C_{ijkl}\left\{p_{klpmn}(\mathbf{y}, s) + H_{kmn}(\mathbf{y}, s)\delta_{lp}\right\} \tag{232}$$

where $\theta(\mathbf{y}) = \rho(\mathbf{y})/\rho_0$, $p_{klpmn} = P_{(k,y_l)pmn}$ and $\boldsymbol{\delta}$ is the Kronecker delta. The local periodicity and the normalization conditions are employed in the same manner as for $\mathbf{H}$. The homogenized equation of motion at $O(\zeta)$ is derived by substituting Eqs. 224

and 230 to Eq. 223c and applying the average operator in addition to considering $\boldsymbol{\sigma}_2$ being locally periodic:

$$\rho_0 U_i^1 s^2 + \langle \rho(\mathbf{y}) H_{ikl}(\mathbf{y}, s)\rangle e_{xkl}(\mathbf{u}^0) s^2 = \\ D^0_{ijmn}(s) e_{xmn}(\mathbf{U}^1)_{,x_j} + D^1_{ijkmn}(s) e_{xmn}(\mathbf{u}^0)_{,x_k x_j}; \quad \mathbf{x} \in \Omega \quad (233)$$

where the first order homogenized stiffness tensor, $\mathbf{D}^1$, is defined as:

$$D^1_{ijpmn}(s) = \langle C^1_{ijpmn}(\mathbf{y}, s)\rangle \quad (234)$$

For the homogenization at $O(\zeta^2)$, the third order displacement term, $\mathbf{u}^3$, is approximated by introducing the third order influence function, $\mathbf{Q}(\mathbf{y}, s)$ as:

$$u_i^3(\mathbf{x}, \mathbf{y}, s) = U_i^3(\mathbf{x}, s) + H_{ikl}(\mathbf{y}, s) e_{xkl}(\mathbf{U}^2) + P_{ijkl}(\mathbf{y}, s) e_{xkl}(\mathbf{U}^1)_{,x_j} + Q_{ijkmn}(\mathbf{y}, s) e_{xmn}(\mathbf{u}^0)_{,x_k x_j} \quad (235)$$

Substituting Eq. 235 to Eq. 223c, the governing equation for the third order influence function, $\mathbf{Q}$, after some algebra, becomes:

$$C^2_{ijprmn,y_j}(\mathbf{y}, s) = \theta(\mathbf{y}) D^1_{irpmn}(s) - C^1_{irpmn}(\mathbf{y}, s) \\ + \theta(\mathbf{y}) \left\{ H_{ikp}(\mathbf{y}, s) - \rho_0^{-1} \langle \rho(\mathbf{y}) H_{ikp}(\mathbf{y}, s)\rangle \right\} D^0_{krmn}(s); \quad \mathbf{y} \in \Theta \quad (236)$$

where

$$C^2_{ijprmn}(\mathbf{y}, s) = C_{ijkl}(\mathbf{y}, s) \left\{ q_{klprmn}(\mathbf{y}, s) + P_{krmn}(\mathbf{y}, s) \delta_{lp} \right\} \quad (237)$$

in which $q_{klprmn}(\mathbf{y}, s) = Q_{(k,y_l)prmn}(\mathbf{y}, s)$. The third order influence function, $\mathbf{Q}$, is a fifth rank tensor with the minor symmetry only on the last two indices (i.e. $Q_{ijkmn} = Q_{ijknm}$). Since the explicit computation of $\mathbf{Q}$ is not necessary in the high order homogenization model described below, the boundary value problem for $\mathbf{Q}$ is not discussed further. Substituting Eqs. 224, 230 and 235 and applying the averaging operator to Eq. 223d in addition to $\boldsymbol{\sigma}^3$ being locally periodic, the macroscopic homogenized equation of motion at $O(\zeta^2)$ is then derived as:

$$\begin{aligned}
&\rho_0 U_i^2(\mathbf{x}, s)s^2 + \langle \rho(\mathbf{y}) H_{ikl}(\mathbf{y}, s)\rangle e_{xkl}(\mathbf{U}^1)s^2 + \langle \rho(\mathbf{y}) P_{ijkl}(\mathbf{y}, s)\rangle e_{xkl}(\mathbf{u}^0)_{,y_j} s^2 \\
&= D^0_{ijmn}(s) e_{xmn}(\mathbf{U}^2)_{,x_j} + D^1_{ijrmn}(s) e_{xmn}(\mathbf{U}^1)_{,x_r x_j} + D^2_{ijprmn}(s) e_{xmn}(\mathbf{u})^0_{,x_r x_p x_j}; \quad \mathbf{x} \in \Omega
\end{aligned} \tag{238}$$

where the second order homogenized stiffness tensor, $\mathbf{D}^2$, is expressed as:

$$D^2_{ijprmn}(s) = \langle C^2_{ijprmn}(\mathbf{y}, s)\rangle \tag{239}$$

Considering a mean displacement by averaging the displacement over the characteristic volume:

$$U_i(\mathbf{x}, s) = \langle u_i(\mathbf{x}, \mathbf{y}, s)\rangle = u_i^0(\mathbf{x}, s) + \zeta U_i^1(\mathbf{x}, s) + \zeta^2 U_i^2(\mathbf{x}, s) + O(\zeta^3) \tag{240}$$

The summation of Eqs. 227, 233 and 238 leads to a high order homogenized equation of motion in terms of the mean displacement, $\mathbf{U}$, neglecting $O(\zeta^3)$ and the higher order terms:

$$\begin{aligned}
&\rho_0 U_i(\mathbf{x}, s)s^2 + \zeta\langle \rho(\mathbf{y}) H_{ikl}(\mathbf{y}, s)\rangle e_{xkl}(\mathbf{U})s^2 + \zeta^2\langle \rho(\mathbf{y}) P_{ijmn}(\mathbf{y}, s)\rangle e_{xmn}(\mathbf{U})_{,x_j} s^2 = \\
&D^0_{ijmn}(s) e_{xmn}(\mathbf{U})_{,x_j} + \zeta D^1_{ijkmn}(s) e_{xmn}(\mathbf{U})_{,x_k x_j} + \zeta^2 D^2_{ijprmn}(s) e_{xmn}(\mathbf{U})_{,x_r x_p x_j}; \quad \mathbf{x} \in \Omega
\end{aligned} \tag{241}$$

The terms inducing micro-inertia effects in the macroscopic equation of motion defined in Eq. 241 are scaled by the orders of ζ, which leads to zero at the asymptotic limit. This appears to indicate that the contribution of the high order terms are trivial. This apparent contradiction is resolved by observing that the coefficients in these terms themselves are size dependent. It can be shown that $\mathbf{D}^1$ and $\langle\rho\mathbf{H}\rangle$ are proportional to $\hat{l}$, and $\mathbf{D}^2$ and $\langle\rho\mathbf{P}\rangle$ are proportional to $\hat{l}^2$ [16]:

$$\mathbf{D}^1 = O(\mathbf{C}\hat{l}); \quad \langle\rho\mathbf{H}\rangle = O(\rho\hat{l}) \tag{242a}$$

$$\mathbf{D}^2 = O(\mathbf{C}\hat{l}^2); \quad \langle\rho\mathbf{P}\rangle = O(\rho\hat{l}^2) \tag{242b}$$

where $\hat{l} = l/\zeta$ is the characteristic length of the microstructure in the stretched coordinate system $\mathbf{y}$, and l the characteristic length of microstructure in the macroscopic coordinate system $\mathbf{x}$. $\mathbf{D}^1$, $\mathbf{D}^2$, $\langle\rho\mathbf{H}\rangle$ and $\langle\rho\mathbf{P}\rangle$ are homogeneous functions of degree 1. Consequently:

$$\zeta\mathbf{D}^1 = O(\mathbf{C}l); \quad \zeta\langle\rho\mathbf{H}\rangle = O(\rho l) \tag{243a}$$

$$\zeta^2\mathbf{D}^2 = O(\mathbf{C}l^2); \quad \zeta^2\langle\rho\mathbf{P}\rangle = O(\rho l^2) \tag{243b}$$

In this study, $\zeta\mathbf{D}^1$, $\zeta^2\mathbf{D}^2$, $\zeta\langle\rho\mathbf{H}\rangle$ and $\zeta^2\langle\rho\mathbf{P}\rangle$ which are directly calculated using the physical geometric size as opposed to stretched configurations. The coefficients are therefore expressed at order $O(1)$.

3.2 A Simplified High Order Homogenization Model

Under the assumption that: (1) the homogenized material exhibits orthotropy or higher symmetry; (2) within a microstructural constituent domain, the elastic modulus tensor and constituent density are assumed to be constant, but the properties are allowed to vary from constituent to another and generate micro-inertia under dynamic conditions. Two conclusions are drawn:

$$D^1_{ijkl}(s) = 0 \tag{244}$$

$$\langle\rho(\mathbf{y})H_{ikl}(\mathbf{y}, s)\rangle = 0 \tag{245}$$

The demonstration of the above equations are provided in Chapter 4 in the time domain, and the demonstration procedure in the Laplace domain is identical to what is in the time domain since all the manipulation is regarding the spatial variables. The fourth order derivative in Eq. 241 prevents the standard finite element solution. In order to apply the standard finite element solution on the problem, the high order term needs to be broken down to lower order terms as follows:

$$D^2_{ijprmn}(s) \approx A_{ijpq}(s) D^0_{qrmn}(s) \tag{246}$$

Since the multiplication only permutes over the fourth subscript, no inversion of $\mathbf{D}^0$ may be found. Instead, we search for the Moore-Penrose pseudo-inversion of $\mathbf{D}^0$ which is defined as:

$$A^*_{ijpq}(s) = D^2_{ijprmn}(s) D^{0\ \text{-mp}}_{qrmn}(s) \tag{247}$$

where '-mp' denotes the Moore-Penrose pseudo-inverse as provided in Appendix C. The fourth order term in Eq. 241 is expressed as:

$$\zeta^2 D^2_{ijprmn}(s) e_{xmn}(\mathbf{U})_{,x_r x_p x_j} = \zeta^2 A^*_{ijpq}(s) D^0_{qrmn}(s) e_{xmn}(\mathbf{U})_{,x_r x_p x_j} \tag{248}$$

Using Eq. 227 and neglecting $O(\zeta^3)$ and the higher order terms:

$$\zeta^2 A^*_{ijpq}(s) D^0_{qrmn}(s) (e_{xmn}(\mathbf{U}))_{,x_r x_p x_j} = \zeta^2 \rho_0 A^*_{ijmn}(s) e_{xmn}(\mathbf{U})_{,x_j} s^2 \tag{249}$$

Substituting Eq. 248 to Eq. 241, the macroscopic equation of motion in terms of the mean displacement, $\mathbf{U}$, becomes:

$$\rho_0 U_i(\mathbf{x}, s) s^2 + \zeta^2 \langle \rho(\mathbf{y}) P_{ijmn}(\mathbf{y}, s) \rangle (e_{xmn}(\mathbf{U}))_{,x_j} s^2 = \\ D^0_{ijmn}(s) (e_{xmn}(\mathbf{U}))_{,x_j} + \zeta^2 \rho_0 A^*_{ijmn}(s) e_{xmn}(\mathbf{U})_{,x_j} s^2 \tag{250}$$

The second order influence function $\mathbf{P}$ exhibits minor symmetry with respect to the last two indices only, and we employ its symmetric part as:

$$J_{ijmn}(s) = \frac{1}{2}\left(\langle \rho(\mathbf{y}) P_{ijmn}(\mathbf{y}, s)\rangle + \langle \rho(\mathbf{y}) P_{jimn}(\mathbf{y}, s)\rangle\right) \tag{251}$$

In addition, $\mathbf{A}^*$ possesses the minor symmetry with respect to the first two indices only (i.e. $A^*_{ijpq} = A^*_{jipq}$). $\mathbf{A}^*$ is then decomposed into its symmetric and antisymmetric components as:

$$A_{ijkl}(s) = \frac{1}{2}\left(A^*_{ijkl}(s) + A^*_{ijlk}(s)\right) \tag{252a}$$

$$B_{ijkl}(s) = \frac{1}{2}\left(A^*_{ijkl}(s) - A^*_{ijlk}(s)\right) \tag{252b}$$

Using the symmetry of strain tensor along with Eq. 252, the equation of motion for the high order homogenization model reduces to:

$$\rho_0 U_i(\mathbf{x}, s) s^2 = D^0_{ijmn}(s)(e_{xmn}(\mathbf{U}))_{,x_j} - L_{ijmn}(s)(e_{xmn}(\mathbf{U}))_{,x_j} s^2; \quad \mathbf{x} \in \Omega \tag{253}$$

where the micro-inertia induced acceleration modulus tensor, $\mathbf{L}$, is defined as:

$$L_{ijmn}(s) = \zeta^2 (J_{ijmn}(s) - \rho_0 A_{ijmn}(s)) \tag{254}$$

where the antisymmetric components of the micro-inertia terms, $\mathbf{B}$, in the governing equation of motion vanish by multiplying with $\mathbf{e}_x(\mathbf{U})$. The tensor, $\mathbf{L}$, satisfies the minor symmetry for both the first two and last two indices (i.e. $L_{ijmn} = L_{jimn}$; $L_{ijmn} = L_{ijnm}$) that facilitates the finite element solution. From Eq. 253, the constitutive equation for the high order homogenization model at the macroscale is defined in the Laplace domain as:

$$\Sigma_{ij}(\mathbf{x},s) = \left(D^0_{ijmn}(s) - s^2 L_{ijmn}(s)\right) e_{xmn}(\mathbf{U}); \quad \mathbf{x} \in \Omega \tag{255}$$

4 Calculation of Dissipated Energy

The dissipated energy is calculated for the high order homogenization model to assess wave dissipation. In the present work, the Prony series is used for the linear viscoelastic material model and the modulus tensor is expressed as:

$$g_{ijkl}(\mathbf{y},t) = 3K_\infty(\mathbf{y}) \left(1 + \sum_{i=1}^{n} p_i(\mathbf{y}) e^{-t/q_i(\mathbf{y})}\right) E^1_{ijkl} + 2G_\infty(\mathbf{y}) \left(1 + \sum_{i=1}^{n} p_i(\mathbf{y}) e^{-t/q_i(\mathbf{y})}\right) E^2_{ijkl} \tag{256}$$

where

$$E^1_{ijkl} = \frac{\delta_{ij}\delta_{kl}}{3} \tag{257}$$

$$E^2_{ijkl} = \frac{\delta_{ik}\delta_{jl} + \delta_{il}\delta_{jk}}{2} - E^1_{ijkl} \tag{258}$$

The displacement, $\mathbf{u}(\mathbf{x},\mathbf{y},s)$, is be expressed in terms of the mean displacement, $\mathbf{U}(\mathbf{x},s)$, by revisiting the asymptotic expansion of $\mathbf{u}(\mathbf{x},\mathbf{y},s)$:

$$\begin{aligned} u_i(\mathbf{x},\mathbf{y},s) = {} & u^0_i(\mathbf{x},s) + \zeta U^1_i(\mathbf{x},s) + \zeta^2 U^2_i(\mathbf{x},s) + \cdots \\ & + \zeta H_{ikl}(\mathbf{y},s) \left(e_{xkl}(\mathbf{u}^0) + \zeta e_{xkl}(\mathbf{U}^1) + \zeta^2 e_{xkl}(\mathbf{U}^2)\right) + \cdots \\ & + \zeta^2 P_{ijkl}(\mathbf{y},s) \left(e_{xkl}(\mathbf{u}^0)_{,x_j} + \zeta e_{xkl}(\mathbf{U}^1)_{,x_j} + \zeta^2 e_{xkl}(\mathbf{U}^2)_{,x_j}\right) + \cdots \end{aligned} \tag{259}$$

It is straightforward that $\mathbf{u}(\mathbf{x},\mathbf{y},s)$ is expanded by the ascending order of ζ in terms of the mean displacement as:

$$u_i(\mathbf{x},\mathbf{y},s) = U_i(\mathbf{x},s) + \zeta H_{ikl}(\mathbf{y},s)e_{xkl}(\mathbf{U}) + \zeta^2 P_{ijkl}(\mathbf{y},s)e_{xkl}(\mathbf{U})_{,x_j} + \cdots \tag{260}$$

The strain in the Laplace domain is then calculated as:

$$\epsilon_{ij}(\mathbf{x},\mathbf{y},s) = \left(I_{ijkl} + h_{ijkl}(\mathbf{y},s)\right) e_{xkl}(\mathbf{U}) + O(\zeta) \tag{261}$$

The influence function indicates the heterogeneity of the strain tensor in microstructures. The strain tensor needs to be transformed from the Laplace domain to the time domain in order to calculate the dissipated energy in the time domain: $\epsilon(\mathbf{x},\mathbf{y},s) \rightarrow \epsilon(\mathbf{x},\mathbf{y},t)$. Besides, the dissipated energy is decomposed into two components: deviatoric and hydrostatic components. The dissipated energy density rate due to deviatoric components is calculated as:

$$s^k_{ij}(\mathbf{x},\mathbf{y},t) = \int_0^t e^{-(t-\tau)/q_k(\mathbf{y})}\dot{\epsilon}'_{ij}(\mathbf{x},\mathbf{y},\tau)d\tau \tag{262}$$

$$\dot{w}^k_s(\mathbf{x},t) = \frac{1}{\Theta}\int_\Theta 2G_\infty(\mathbf{y})\frac{p_k(\mathbf{y})}{q_k(\mathbf{y})}s^k_{ij}s^k_{ij}d\mathbf{y} \tag{263}$$

where $\boldsymbol{\epsilon}'$ is the deviatoric component of strain, $\mathbf{s}^k$ is the deviatoric component of dissipating strain. w^k_s is the deviatoric component induced dissipated energy density associated with the k^{th} internal viscous variable. The integration over the microstructure, Θ, calculates the dissipated energy density rate at each integration point at the macroscale. Similarly, the dissipated energy density rate due to hydrostatic components is calculated as:

$$b_{ij}^k(\mathbf{x},\mathbf{y},t) = \int_0^t e^{-(t-\tau)/q_k(\mathbf{y})}\dot{\epsilon}_{ll}(\mathbf{x},\mathbf{y},\tau)\delta_{ij}d\tau \tag{264}$$

$$\dot{w}_b^k(\mathbf{x},t) = \frac{1}{\Theta}\int_\Theta K_\infty(\mathbf{y})\frac{p_k(\mathbf{y})}{q_k(\mathbf{y})}b_{ij}^k b_{ij}^k d\mathbf{y} \tag{265}$$

where $\mathbf{b}^k$ is the hydrostatic component of dissipated strain and w_b^k the hydrostatic components induced dissipated energy density associated with the k^{th} internal dissipated variable. The total dissipated energy density rate is calculated as:

$$\dot{w}(\mathbf{x},t) = \sum_k^n \dot{w}_s^k(\mathbf{x},t) + \sum_k^n \dot{w}_b^k(\mathbf{x},t) \tag{266}$$

The total dissipated energy, W_d, is calculated by integration over the macrostructure, Ω, and the time history:

$$W_d(t) = \int_0^t \int_\Omega \dot{w}(\mathbf{x},t)d\mathbf{x}dt \tag{267}$$

5 Numerical Implementation

The numerical implementation of the multiscale homogenization model includes the computation of corresponding fields in the time domain and the Laplace domain. A numerical inverse Laplace transform [17] based on the Fast Fourier Transform and the ϵ-algorithm [43] is used to convert solutions from the Laplace domain into the time domain. Several steps are followed in the numerical implementation:

1. A group of discrete time steps (i.e., t_β where $\beta = 1, 2, \cdots N_t$ and N_t is the number of time steps) are generated within the given time duration. A group of complex arguments (i.e., s_α where $\alpha = 1, 2, \cdots N_s$ and N_s is the number of complex arguments) are generated along a vertical line (i.e., of the same real part) in the complex plane and within the convergence region of the inverse

Laplace transform integration. Note that the density and coverage of generated complex arguments along the vertical line should be large enough for accurate inverse Laplace transform.

2. The first order influence function at s_α, $\mathbf{H}(\mathbf{y}, s_\alpha)$, is obtained using the finite element solution of the boundary value problem defined by Eq. 225 in the $O(1)$ homogenization and the local periodicity and normalization conditions of $\mathbf{H}(\mathbf{y}, s_\alpha)$. The weak form of Eq. 225 is:

$$\int_\Theta w_{i,y_j}(\mathbf{y}, s) C_{ijkl}(\mathbf{y}, s) h_{klmn}(\mathbf{y}, s) d\mathbf{y} = -\int_\Theta w_{i,y_j}(\mathbf{y}, s) C_{ijmn}(\mathbf{y}, s) d\mathbf{y} \qquad (268)$$

3. Provided with $\mathbf{H}(\mathbf{y}, s_\alpha)$, the second order influence function at s_α, $\mathbf{P}(\mathbf{y}, s_\alpha)$, is obtained using the finite element solution of the boundary value problem defined by Eq. 231 in the $O(\zeta)$ homogenization and the local periodicity and normalization conditions of $\mathbf{P}(\mathbf{y}, s_\alpha)$. The weak form of Eq. 231 is:

$$\int_\Theta w_{i,y_j}(\mathbf{y}, s_\alpha) \left(C_{ijkl}(\mathbf{y}, s_\alpha)(p_{klpmn}(\mathbf{y}, s_\alpha) + H_{kmn}(\mathbf{y}, s_\alpha)\delta_{lp}) \right) d\mathbf{y} =$$
$$-\int_\Theta w_i(\mathbf{y}, s_\alpha) \left(\theta(\mathbf{y}) D^0_{ipmn}(s_\alpha) - C^0_{ipmn}(\mathbf{y}, s_\alpha) \right) d\mathbf{y} \qquad (269)$$

4. The homogenized modulus tensors $\mathbf{D}_0(s_\alpha)$ and $\mathbf{D}_2(s_\alpha)$ defined in Eqs. 228 and 239 are evaluated numerically based on the solutions of $\mathbf{H}(\mathbf{y}, s_\alpha)$ and $\mathbf{P}(\mathbf{y}, s_\alpha)$.

5. The mean displacement at s_α, $\mathbf{U}(\mathbf{x}, s_\alpha)$, is obtained using the finite element solution of the boundary value problem defined by Eq. 253 at the macroscale together with the corresponding boundary conditions. The weak form of Eq. 253

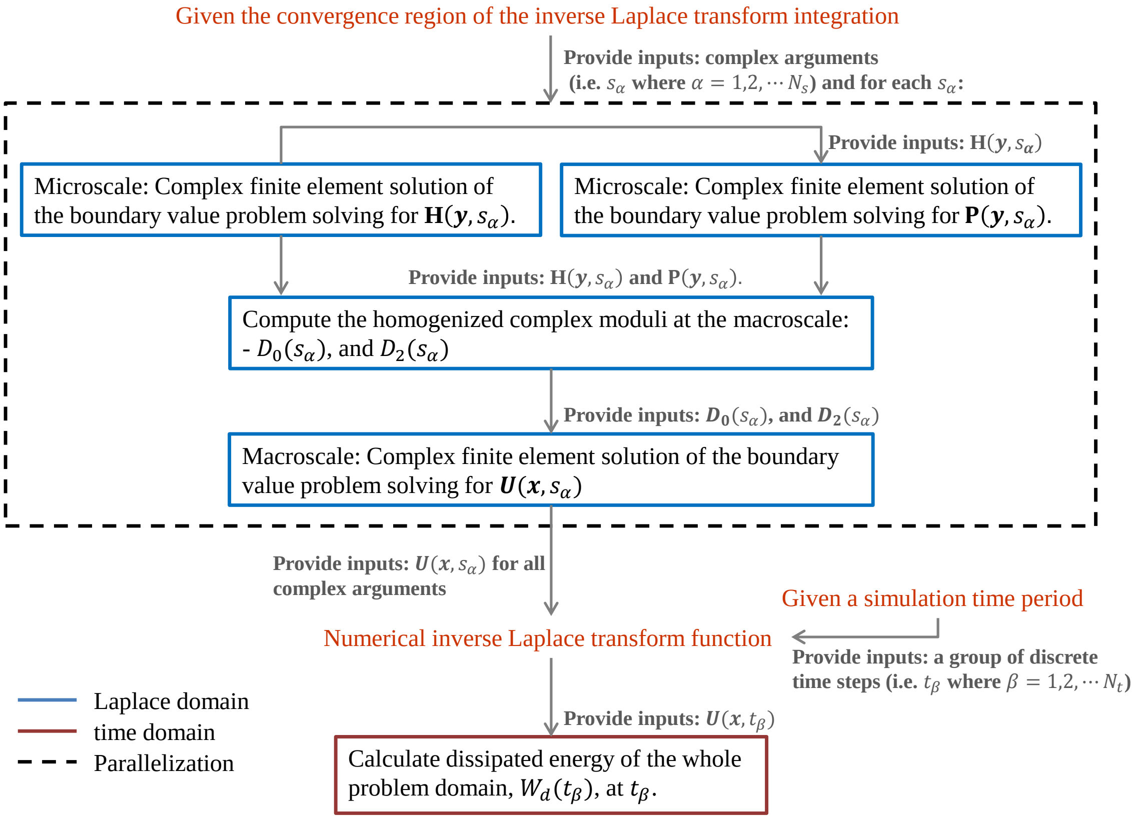

Figure 30: Computational flowchart.

is:

$$\int_\Omega \rho_0 w_i(\mathbf{x}, s_\alpha) U_i(\mathbf{x}, s_\alpha) s_\alpha^2 d\mathbf{x} - \int_\Omega w_{i,x_j}(\mathbf{x}, s_\alpha) L_{ijmn}(s_\alpha) e_{xmn}(\mathbf{U}) s_\alpha^2 d\mathbf{x}$$
$$+ \int_\Omega w_{i,x_j}(\mathbf{x}, s_\alpha) D^0_{ijmn}(s_\alpha) e_{xmn}(\mathbf{U}) d\mathbf{x} = \int_{\Gamma^t} w_i(\mathbf{x}, s_\alpha) \Sigma_{ij}(\mathbf{x}, s_\alpha) n_j d\mathbf{x} \quad (270)$$

6. Repeat Steps 2-5 to calculate the mean displacements in the Laplace domain for all the complex arguments. Provide the complex valued mean displacements to the numerical inverse Laplace transform and calculate the mean displacements for all the time steps in the real time domain.

7. Calculate the dissipated energy of the whole problem domain at each time step using the mean displacements in the time domain obtained in Step 6.

Table 5: Material constants for elastic and viscoelastic phases.

Elastic phase			
$E[GPa]$	ν	ρ[kg/m^3]	
2.0	0.3	7900	
Viscoelastic phase			
G_∞[MPa]	K_∞[MPa]	ρ[kg/m^3]	
22.4	431.4	1070	
p_1	p_1	p_1	p_1
0.8458	1.686	3.594	4.342
q_1 [ms]	q_2 [ms]	q_3 [ms]	q_4 [ms]
463.4	0.06407	1.163×10^{-4}	7.321×10^{-7}

Note that the finite element solutions in Steps 2, 3 and 5 are complex valued due to the complex modulus tensors in the Laplace domain. The finite element discretization of the weak forms (i.e., Eqs. 268, 269 and 270) is identical to what has been extensively discussed by **?**] and skipped in this manuscript. In addition, the computations in Steps 2-5 are independent with each other with respect to each complex argument, s_α, and are able to be parallelized. This will increase the computational efficiency significantly in cluster environment. The flowchart summarizing the computational implementation of the multiscale homogenization model is shown in Fig. 30.

6 Numerical Verification

A series of numerical simulations has been conducted to assess the performance of the proposed high order homogenization model and verified against direct numerical simulations. A two-dimensional square composite domain was considered as illustrated in Fig. 31. Two different microstructures are considered: layered and particulate. The microstructures consist of an elastic and a viscoelastic phase as shown in Fig. 31. The material parameters for the elastic and viscoelastic phases are summarized in Table 5. The volume fraction of the elastic phase in the layered and the particulate microstructures are 80% and 63.6%, respectively. The composite domain was excited using a displacement controlled sinusoidal disturbance applied at the 50 mm segment along the vertical centerline (i.e., v-cl in Fig. 31). The maximum loading amplitude is set to $u_R = 0.01$mm. The domain is clamped at the bottom edge. The direct numerical simulations employed to verify the multiscale model is the direct finite element analysis (direct FEA), in which all heterogeneities are fully resolved throughout the composite domain. The direct FEA simulations use the explicit time integration with time step sizes significantly smaller than the stability limit to ensure high accuracy.

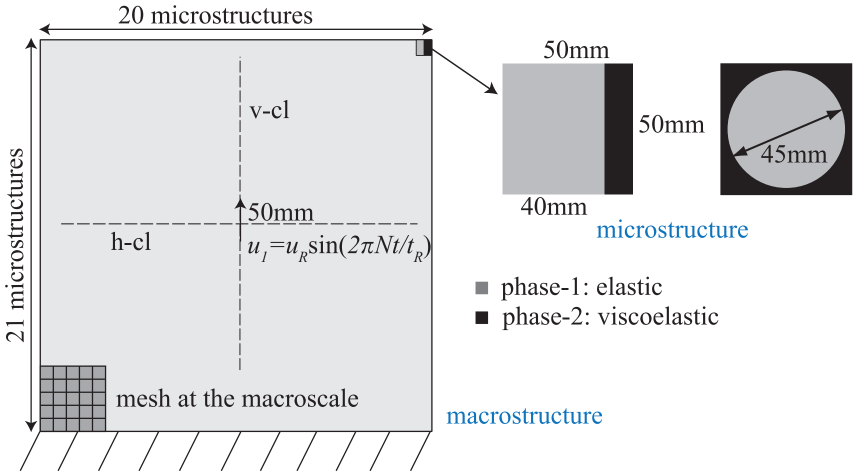

Figure 31: Layered and fibered composite structures under sinusoidal displacement disturbance.

6.1 Dynamic Response of Layered Composite

Figures 32-35 show the vertical component of the macroscopic displacement field (i.e., U_2) computed using the multiscale model and the direct FEA. The displacement within the problem domain is plotted at five time instances (i.e., $t = 0.4, 0.8, 1.2, 1.6$ and 2 ms) for four loading frequencies: 500 Hz, 1000 Hz, 1500 Hz and 3000 Hz. The domain and loading was chosen to ensure that within the simulation period ($t_R = 2$ ms), boundary dispersion (i.e., the interference due to reflection of the deformation waves off the domain boundaries) is relatively small and that the dispersion is largely induced by micro-heterogeneity only.

The response predictions of the multiscale model at all frequencies shown in Figs. 32-35 are in good agreement with the direct FEA. At the relatively low loading frequency of 500 Hz (Fig. 32), the wavelength remains well above the microstructure size and the effect of micro-heterogeneity induced wave dispersion is insignificant. The displacement contours show an ellipsoidal shape (e.g., Fig. 32b), since the propagations along the horizontal and vertical directions are governed by the s and p wave speeds, respectively. When the applied loading frequency is 1000 Hz, the interaction of the wave with the material microstructure is apparent as shown in Fig. 33. The interactions intensify at 1500 Hz loading frequency (Fig. 34). The wave along the horizontal centerline (h-cl in Fig. 31) is largely attenuated, which indicates the possibility of the occurrence of bandgaps. A second possible source of wave attenuation is the material dissipation due to the viscoelastic phase. The contribution of material dissipation on wave attenuation is further discussed below in terms of dissipated energies. When the loading frequency increases to 3000 Hz (Fig. 35), strong wave dispersion is observed and wave propagation is largely attenuated in most directions.

The occurrence of the bandgap behavior is further investigated by conducting a one-dimensional shear wave propagation analysis in a layered media with identical composition to the composite domain studied herein. The one-dimensional wave propagation problem in periodic viscoelastic media has a semi analytical solution as described in Chapter 3. The results of the one-dimensional analysis are employed to partially verify the wave propagation in the 2-d multiscale simulations along the horizontal centerline since the propagation along the horizontal centerline is relatively undisturbed. Figure 36 shows the displacement histories of an observation point at loading frequencies of 1000 Hz, 1250 Hz and 1500 Hz as computed using the one-dimensional solution. The observation point is four microstructures (i.e., 200 mm) away from the loading end. An increase in wave attenuation is observed with increasing load frequency. When the load frequency is set at 1500 Hz frequency, the observation point remains undisturbed throughout the analysis period indicating either the occurrence of the bandgap or very strong material dissipation. The results of the one-dimensional simulation are in agreement with the two-dimensional simulation along the horizontal centerline.

The direct FEA solution under the loading frequency of 3000 Hz shows a near-complete wave attenuation along the horizontal direction, whereas along the vertical direction localized within the central two layers, wave propagates without significant attenuation. This result is consistent with the layered microstructure aligned along the vertical direction, allowing the p-waves to propagate freely through the uniform constituents at the mid-section. In comparison, the localized vertical wave propagation is largely attenuated in the homogenized component of the multiscale model. This discrepancy is attributed to the smearing effect due to the averaging performed over the microstructure (i.e., unit cell) domain in the multiscale model, and that the plotted macroscale displacement field, $\mathbf{U}$, is the average component of the response field and the fluctuations within the microstructure domain is not shown in the multiscale solution.

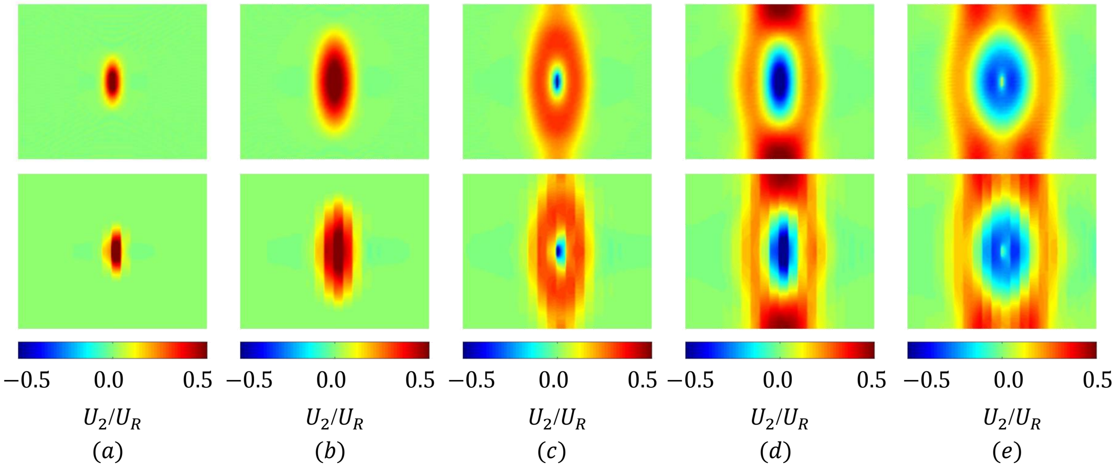

Figure 32: High order homogenization (top row) and direct FEA (bottom row) solutions when loading frequency = 500 Hz: (a) t = 0.4 ms; (b) t = 0.8 ms; (c) t = 1.2 ms; (d) t = 1.6 ms; (e) t = 2 ms.

The dissipated energy is calculated when the loading frequencies equal to 500,

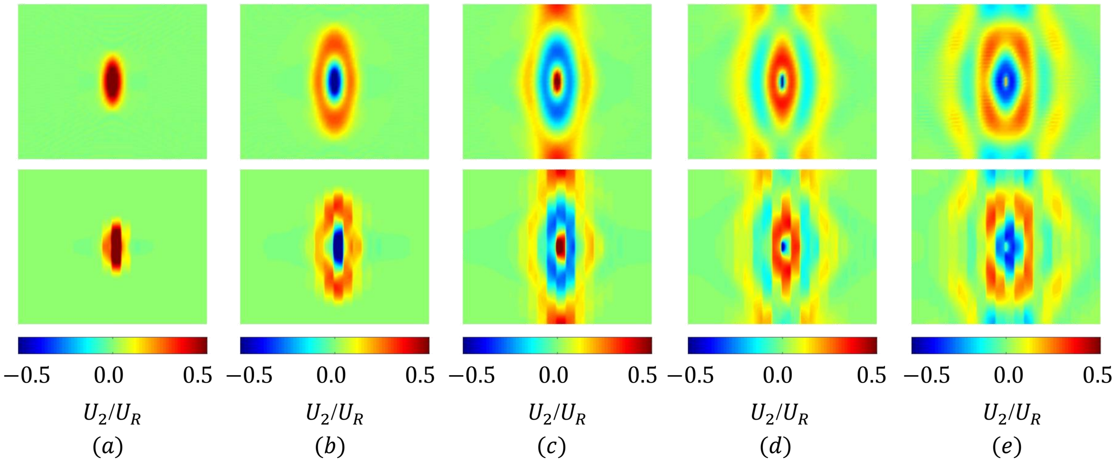

(a) (b) (c) (d) (e)

Figure 33: High order homogenization (top row) and direct FEA (bottom row) solutions when loading frequency = 1000 Hz: (a) t = 0.4 ms; (b) t = 0.8 ms; (c) t = 1.2 ms; (d) t = 1.6 ms; (e) t = 2 ms.

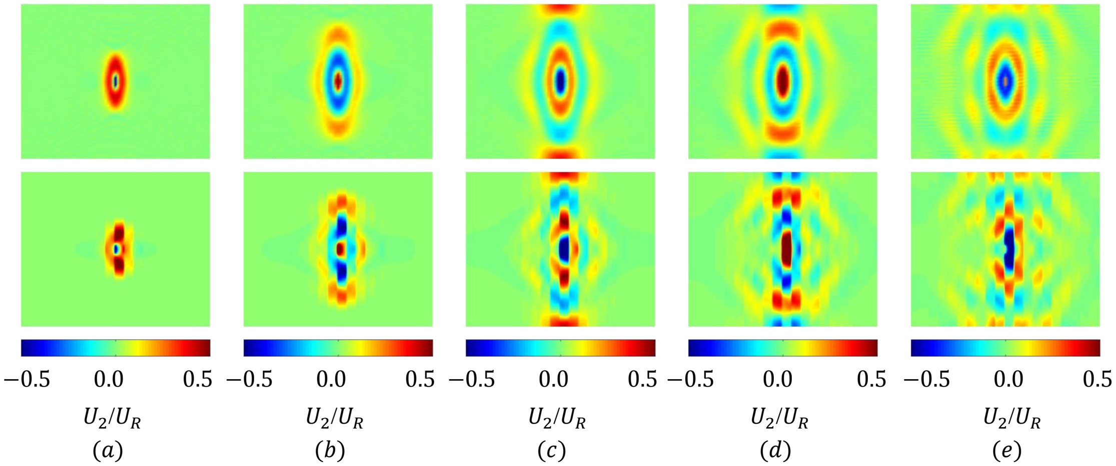

(a) (b) (c) (d) (e)

Figure 34: High order homogenization (top row) and direct FEA (bottom row) solutions when loading frequency = 1500 Hz: (a) t = 0.4 ms; (b) t = 0.8 ms; (c) t = 1.2 ms; (d) t = 1.6 ms; (e) t = 2 ms.

1000, 1500 and 3000 Hz respectively. The dissipated energy ratio defined as the ratio of dissipated energy to total energy input is plotted in Fig. 37 where the high order homogenization solutions are compared with the direct finite element solution. The high order homogenization method predicts the dissipated energy in good agreement with the finite element solutions. In particular, when the loading frequency is 3000 Hz, the high order homogenization prediction is also close to the direct finite element

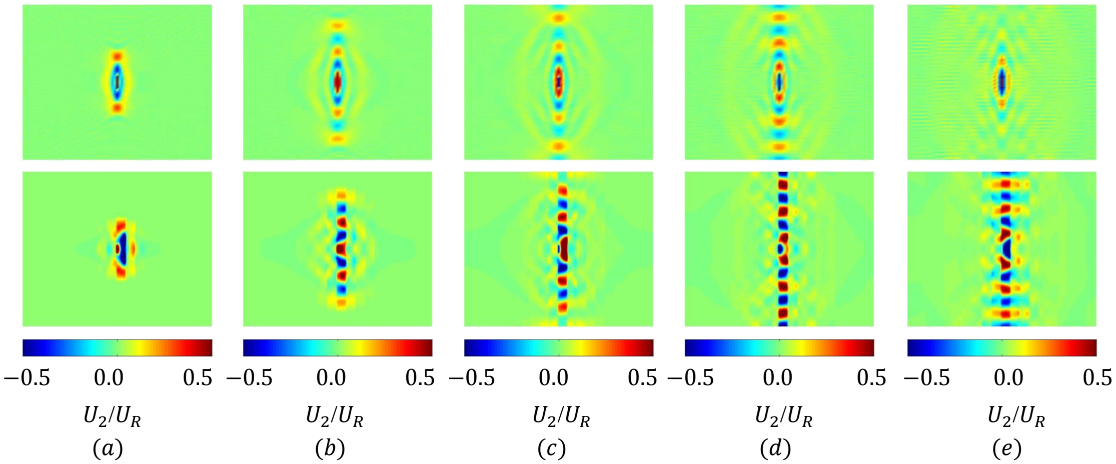

Figure 35: High order homogenization (top row) and direct FEA (bottom row) solutions when loading frequency = 3000 Hz: (a) t = 0.4 ms; (b) t = 0.8 ms; (c) t = 1.2 ms; (d) t = 1.6 ms; (e) t = 2 ms.

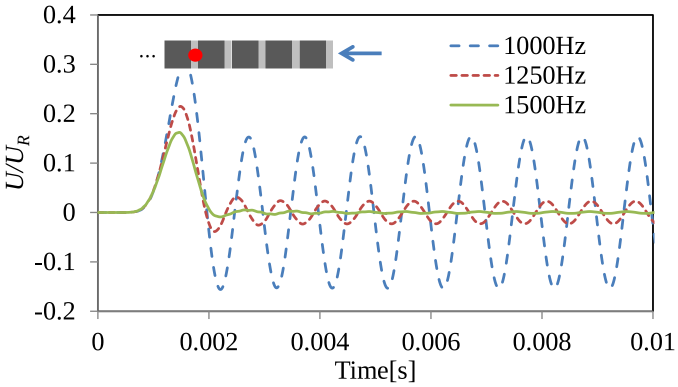

Figure 36: One-dimensional wave propagation in viscoelastic-elastic composite beam.

solution despite the discrepancy in the displacement contours as show in Fig. 35. This is because in the calculation of dissipated energy, the microscopic information (i.e., influence functions) is retrieved at each integration point at the macroscale as shown in Eq. 261. On the other hand, it is found that the dissipated energy ratio at the end of the simulation period tends to stabilize when the loading frequency increases as shown in Fig. 37. When the loading frequency is 500 Hz, the total dissipated energy ratio is around 30%; when the loading frequency increases above 1000 Hz until 3000 Hz, the total dissipated energy ratio stays around 50%. This finding actually elucidates the contribution of bandgap on attenuating the wave propagation. Specifically, when the loading frequency reaches 3000 Hz, only 50% of the total energy input is dissipated by material dissipation, and the rest of the input energy would make the wave propagate in all directions if there were no dispersion in microstructures. However, in fact, as shown in Fig. 35, the wave propagation in the horizontal direction is forbidden. This means that the bandgap prohibits the wave propagation in the horizontal direction.

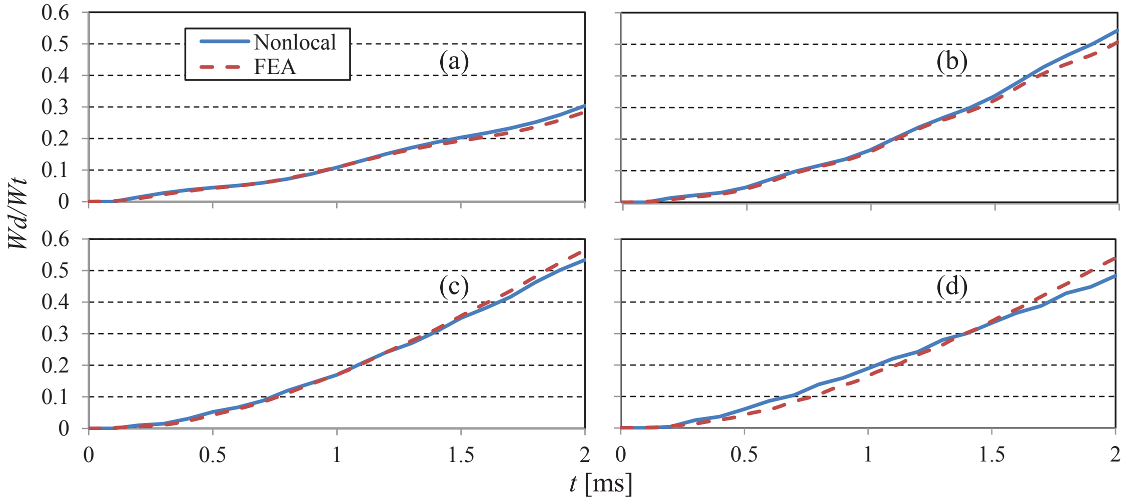

Figure 37: Dissipated energies calculated by the high order homogenization and direct FEA with loading frequency (a) 500 Hz; (b) 1000 Hz; (c) 1500 Hz; (d) 3000 Hz.

6.2 Dynamic Response of Particulate Composite

The capability and the performance of the proposed multiscale model are further demonstrated by investigating the dynamic behavior of a particulate composite. The domain of the composite structure and the loading conditions remain identical to the layered configuration. The geometry of the particulate microstructure is shown in Fig. 31. The particle phase is taken to be elastic, whereas the matrix is viscoelastic with material properties shown in Table 5. Figure 38 illustrates the vertical component of the macroscopic displacement field (i.e., U_2) computed using the multiscale model at five time instances within the observation period (i.e., at 1.2, 2.4, 3.6, 4.8 and 6.0 ms) for three different loading frequencies (i.e., 250 Hz, 500 Hz and 1000 Hz). The wave propagation response is markedly different compared to the layered configuration due to the significantly different microstructural configurations. The loading frequency of 250 Hz corresponds to the a wave propagation response with little material dispersion. When the loading frequency increases to 500 Hz, strong wave dispersion occurs and the wave propagations particularly along the horizontal and vertical centerlines demonstrate significant wave attenuation. The wave propagation falls into the bandgap when the loading frequency reaches to 1000 Hz. In contrast to the layered microstructure, near complete wave attenuation occurs at a lower frequency in the particulate composite. The sensitivity of the attenuation characteristics to the microstructure points to the capability to control the dispersion and wave attenuation characteristics through microstructure design.

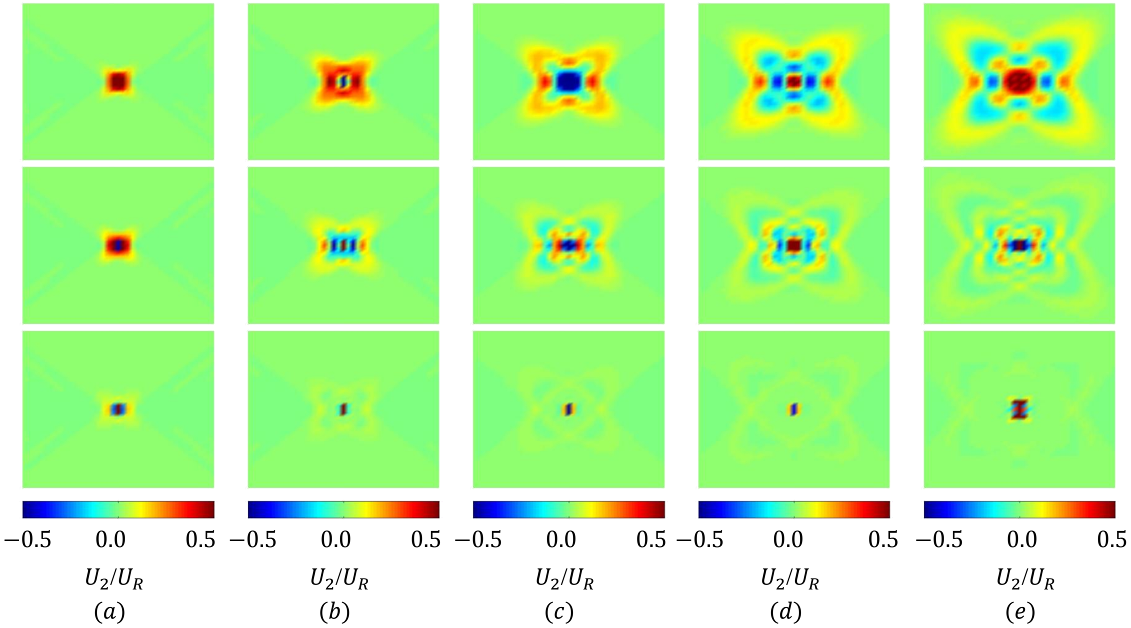

Figure 38: High order homogenization solutions when loading frequency = 250 Hz (top row), 500 Hz (middle row) and 1000 Hz (bottom row) at (a) t = 1.2 ms; (b) t = 2.4 ms; (c) t = 3.6 ms; (d) t = 4.8 ms; (e) t = 6.0 ms.

6.3 Computational Efficiency

The proposed multiscale model is significantly more computationally efficient compared to the direct finite element analysis. For example of the layered composite structure, 6720 elements were used for the discretization of the macroscopic domain and 800 elements were used for the microscopic domain with the multiscale model. In comparison, 168,000 elements were used in the direct finite element solution in order to calculate the wave dispersion at high frequency loadings. For the multiscale model, both the microscopic and macroscopic problems need to be evaluated for each complex argument, s, however the tremendous reduction in the number of elements increases the computational efficiency significantly. On the other hand, 500 iterations (i.e. a set of 500 complex arguments, s) are enough to render accurate dispersive wave responses in the homogenization model while $200,000$ time steps are required to obtain accurate dispersive wave responses in the direct finite element solution. The parallelization in the homogenization model for the micro- and macroscopic problems also improves the computational efficiency in cluster environment.

7 Conclusions

In this chapter, we presented a high order homogenization model for simulating wave propagation in viscoelastic composite structures. The proposed model is defined in the Laplace domain based on the mathematical homogenization with multiple spatial scales. The high order asymptotic terms have been introduced to capture micro-heterogeneity induced wave dispersions. The complex wave fields were solved using the complex finite element solution formulated in the Laplace domain. The proposed model was verified against the direct finite element solution and the one-dimensional semi-analytical solution.

Based on the numerical results, the proposed model is able to accurately predict the wave propagation and dispersion in the layered and particulate viscoelastic composites under different loading frequencies. In addition, the complex high order homogenization model was shown to successfully predict the occurrence of and the wave propagation within the bandgaps. The sensitivity of wave attenuation with respect to the microstructure leads to the capability to control the dispersion and wave attenuation characteristics through microstructure design.

CHAPTER 6

SUMMARY AND FUTURE WORK

1 Conclusions

This dissertation proposed a computational framework of the dynamic response of composite structures. The framework is developed based on the mathematical homogenization theory with multiple spatial scales. The multiscale homogenization model serves to reproduce wave attenuation and micro-heterogeneity induced wave dispersion. The principal achievements of this dissertation are summarized below:

Chapter 2 provided an investigation of the blast mitigation effect of polyurea, used in protective layers, on woven E-glass fiber-reinforced vinyl-ester (EVE) composites. The response of EVE layers was modeled based on a multiscale computational damage model that included adiabatic heating and rate-dependence in the constituent (i.e. matrix and fiber) behavior. The numerical simulations were validated against experimental data demonstrating the capability of the multiscale model in capturing the inelastic response of EVE composite materials. The significant blast mitigation effect of polyurea layer was demonstrated numerically. The predictive simulations suggested better blast mitigation characteristics with increasing polyurea thickness and confining the perimeter of polyurea layers.

Chapter 3 presented a dispersive homogenization solution in the Laplace domain for one-dimensional wave propagation in viscoelastic composites. The high order asymptotic terms were considered in the homogenization formulations to include micro-heterogeneity induced wave dispersion. A semi-analytical solution was derived for wave propagation in bi-material viscoelastic composite structures. The numerical verifications indicate that the proposed nonlocal model is able to accurately account for the dispersion and dispersion induced attenuation under a wide range of loading and material parameters.

Chapter 4 presented a high order homogenization model for multi-dimensional wave propagation in elastic composite materials. The high order asymptotic terms have been introduced to capture the micro-inertia effects caused by the impedance contrast between the microstructural constituents. The finite element formulation for the evaluation of the microscale influence functions and the homogenized model were provided. The proposed high order homogenization model was validated by comparing against the direct finite element solutions and the local homogenization model. From the modeling perspective, the high order homogenization model possesses several advantages. First, the high order homogenization model is able to capture complete density and modulus disparities induced wave dispersion. Second, the proposed model is able to capture wave propagation behaviors within phononic bandgaps. The appearance of bandgap in the high frequency range is due to complex wavenumber which leads to an exponential attenuation. In the proposed model, the ability to model wave propagation within bandgap stems from the complex treatment of the response fields.

Chapter 5 further discussed the high order homogenization model in the Laplace domain for multi-dimensional wave propagation in viscoelastic composites. The homogenization model was defined in the Laplace domain allowing the representation of linear viscoelastic constitutive relationship using a proportionality law. The complex wave fields were solved using the complex finite element solution formulated in the Laplace domain. The proposed model was verified against the direct finite element solution and the one-dimensional semi-analytical solution. The proposed model accurately predicted the wave propagation and dispersion in the layered and particulate viscoelastic composites under different loading frequencies. In addition, the wave propagations within the bandgaps were successfully predicted and the occurrence of bandgaps was adjusted through revising microstructures.

2 Future Work

While the multiscale models work well with the current wave propagation problems in composite structures, several challenges remain in more realistic and complicated applications. First, microstructure is proved to be able to influence the wave dispersion induced wave attenuation characteristics. Therefore, the optimal design of microstructure will provide an additional mechanism of vibration control and impact/blast survivability in heterogeneous materials. This work would require a thorough parametric investigation of microstructures to integrate geometric and constitutive optimizations of rendering satisfactory wave attenuation characteristics. The second challenge is the extension of the proposed model to account for failure process which acts as a necessity in simulating blast incidents where damage essentially controls dynamic responses. However, this is a computationally demanding undertaking, since the present complex homogenization procedure in the Laplace domain cannot be employed in a straightforward manner for damage constitutive models. Accordingly, a computational model operating with general constitutive definitions will be of great value to realistic applications.

Appendix A

THE SOLUTIONS OF LOCALIZATION FUNCTIONS

In chapter 3, the localization functions: $1+H_{,y}(y,s)$, $H(y,s)+P_{,y}(y,s)$ and $P(y,s)+Q_{,y}(y,s)$ in Eq. 105 are derived and shown as follows:

$$1+H_{1,y}(y,s)=\frac{E_0}{E_1}\tag{271}$$

$$1+H_{2,y}(y,s)=\frac{E_0}{E_2}\tag{272}$$

$$H_1(y,s)+P_{1,y}(y,s)=\frac{E_0(1-\alpha)(\rho_1-\rho_2)}{2\rho_0E_1}(2y-\alpha\hat{l})\tag{273}$$

$$H_2(y,s)+P_{2,y}(y,s)=\frac{E_0\alpha(\rho_1-\rho_2)}{2\rho_0E_2}((1+\alpha)\hat{l}-2y)\tag{274}$$

$$\begin{aligned}P_1(y,s)+Q_{1,y}(y,s)=&\frac{E_0^2(1-\alpha)\left[E_1(-2\rho_1+\rho_0)+E_2(\rho_1+\rho_2-\rho_0)\right]}{2\rho_0{E_1}^2E_2}(y^2-\alpha\hat{l}y)\\&-\frac{E_0^3(1-\alpha)\alpha\hat{l}^2}{12\rho_0{E_1}^3{E_2}^2}\cdot\Big[\left((1-\alpha)^2{E_1}^2+\alpha^2{E_2}^2\right)(\rho_0-\rho_1-\rho_2)\\&-E_1E_2\left((2\alpha^3-4\alpha^2+\alpha)\rho_1-(2\alpha^3-2\alpha^2-\alpha+1)\rho_2\right)\Big]\end{aligned}\tag{275}$$

$$\begin{aligned}P_2(y,s)+Q_{2,y}(y,s)=&\frac{E_0^2\alpha\left[E_1(\rho_0-\rho_1-\rho_2)+E_2(2\rho_2-\rho_0)\right]}{2\rho_0E_1{E_2}^2}((\hat{l}+\alpha\hat{l})y-y^2)\\&+\frac{E_0^3\alpha\hat{l}^2}{12\rho_0{E_1}^2{E_2}^3}\cdot\Big[\left(-1-3\alpha+3\alpha^2+\alpha^3\right)(\rho_0-\rho_1-\rho_2){E_1}^2\\&+\alpha^2\left(\left(1+4\alpha+\alpha^2\right)\rho_1-\left(6+5\alpha+\alpha^2\right)\rho_2\right){E_2}^2\\&+E_1E_2\left((\alpha+7\alpha^2-6\alpha^3-2\alpha^4)\rho_1+(-1-4\alpha+\alpha^2+8\alpha^3+2\alpha^4)\rho_2\right)\Big]\end{aligned}\tag{276}$$

Appendix B

PROOF OF $\langle \rho \mathbf{H} \rangle = 0$

In Chapter 4, premultiplying Eq. 135 with the first order influence function, $\mathbf{H}(\mathbf{y})$ and integrating over the domain of the microstructure:

$$\int_{\Theta} H_{ikl} C^{1}_{ijpmn,y_j} d\mathbf{y} = \int_{\Theta} \theta H_{ikl} D^{0}_{ipmn} d\mathbf{y} - \int_{\Theta} H_{ikl} C^{0}_{ipmn} d\mathbf{y} \tag{277}$$

Integrating by parts leads to:

$$\int_{\Theta} H_{ikl} C^{1}_{ijpmn,y_j} d\mathbf{y} = \int_{\Gamma} H_{ikl} C^{1}_{ijpmn} n_j d\mathbf{y} - \int_{\Theta} H_{ikl,y_j} C^{1}_{ijpmn} d\mathbf{y} \tag{278}$$

The boundary integral vanishes due to periodicity. Considering Eq. 132 and 136, Eq. 277 becomes:

$$\begin{gathered} -\int_{\Theta} H_{ikl,y_j} C_{ijrs} \left(p_{rspmn} + H_{rmn} \delta_{sp} \right) d\mathbf{y} = \\ \int_{\Theta} \theta H_{ikl} d\mathbf{y} D^{0}_{ipmn} - \int_{\Theta} H_{ikl} C_{iprs} h_{rsmn} d\mathbf{y} - \int_{\Theta} H_{ikl} C_{iprs} \delta_{rm} \delta_{sn} d\mathbf{y} \end{gathered} \tag{279}$$

Applying the averaging operator to the first term on the right hand side of the equation above:

$$\begin{gathered} -\int_{\Theta} H_{ikl,y_j} C_{ijrs} p_{rspmn} - H_{ikl,y_j} C_{ijrp} H_{rmn} d\mathbf{y} = \\ \frac{|\Theta|}{\rho_0} \langle \rho H_{ikl} \rangle D^{0}_{ipmn} - \int_{\Theta} H_{ikl} C_{iprs} h_{rsmn} d\mathbf{y} - \int_{\Theta} H_{ikl} C_{ipmn} d\mathbf{y} \end{gathered} \tag{280}$$

The major symmetry of $\mathbf{C}$ suggests:

$$H_{ikl} C_{iprs} h_{rsmn} = h_{ijmn} C_{ijrp} H_{rkl} \tag{281}$$

Define:

$$u_{klpmn} = \frac{1}{|\Theta|}\int_{\Theta} h_{ijkl} C_{ijrp} H_{rmn} d\mathbf{y} \tag{282}$$

and $\hat{u}_{klpmn} = u_{klpmn} - u_{mnpkl}$, Eq. 280 becomes:

$$-\int_{\Theta} h_{ijkl} C_{ijrs} p_{rspmn} d\mathbf{y} - |\Theta|\hat{u}_{klpmn} = \frac{|\Theta|}{\rho_0}\langle \rho H_{ikl}\rangle D^0_{ipmn} - \int_{\Theta} H_{ikl} C_{ipmn} d\mathbf{y} \tag{283}$$

Considering Eq. 128, premultiplying the equation with $\mathbf{P}(\mathbf{y})$ and integrating over the microstructure:

$$\int_{\Theta} P_{ipkl} C^0_{ijmn,y_j} d\mathbf{y} = 0 \tag{284}$$

Integrating by parts:

$$\int_{\Theta} P_{ipkl} C^0_{ijmn,y_j} d\mathbf{y} = \int_{\Gamma} P_{ipkl} C^0_{ijmn} n_j d\mathbf{y} - \int_{\Theta} P_{ipkl,y_j} C^0_{ijmn} d\mathbf{y} \tag{285}$$

The boundary integral vanishes due to periodicity and Eq. 132 yields:

$$\int_{\Theta} p_{ijpkl} C^0_{ijmn} d\mathbf{y} = \int_{\Theta} p_{ijpkl} C_{ijst} h_{stmn} d\mathbf{y} + \int_{\Theta} p_{ijpkl} C_{ijst} \delta_{sm}\delta_{tn} d\mathbf{y} = 0 \tag{286}$$

By virtue of the major symmetry of $\mathbf{C}(\mathbf{y})$,

$$\int_{\Theta} h_{ijkl} C_{ijrs} p_{rspmn} d\mathbf{y} = -\int_{\Theta} p_{rspmn} C_{rskl} d\mathbf{y} \tag{287}$$

Using the above conclusion, Eq. 283 becomes:

$$\int_{\Theta} p_{rspmn} C_{rskl} d\mathbf{y} - |\Theta|\hat{u}_{klpmn} = \frac{|\Theta|}{\rho_0}\langle \rho H_{ikl}\rangle D^0_{ipmn} - \int_{\Theta} H_{ikl} C_{ipmn} d\mathbf{y} \tag{288}$$

Integrating Eq. 136 over the microstructure:

$$\int_\Theta C^1_{klpmn} d\mathbf{y} - \int_\Theta C_{klrp} H_{rmn} d\mathbf{y} = \int_\Theta p_{rspmn} C_{rskl} d\mathbf{y} \tag{289}$$

Substituting Eq. 289 into Eq. 288:

$$\frac{|\Theta|}{\rho_0} \langle \rho H_{ikl} \rangle D^0_{ipmn} = \int_\Theta C^1_{klpmn} d\mathbf{y} - \int_\Theta H_{rmn} C_{rpkl} d\mathbf{y} - |\Theta| \hat{u}_{klpmn} + \int_\Theta H_{ikl} C_{ipmn} d\mathbf{y} \tag{290}$$

Let:

$$v_{klpmn} = \frac{1}{|\Theta|} \int_\Theta H_{imn} C_{ipkl} d\mathbf{y} \tag{291}$$

$$\hat{v}_{klpmn} = v_{klpmn} - v_{mnpkl} \tag{292}$$

and defining $\mathbf{D}^1$ as:

$$D^1_{klpmn} = \frac{1}{|\Theta|} \int_\Theta C^1_{klpmn} d\mathbf{y} \tag{293}$$

Eq. 290 is written in terms of $\hat{\mathbf{w}}$ and $\mathbf{D}^1$:

$$\langle \rho H_{ikl} \rangle D^0_{ipmn} = \rho_0 \left(D^1_{klpmn} - \hat{w}_{klpmn} \right) \tag{294}$$

where:

$$\hat{w}_{klpmn} = \hat{u}_{klpmn} + \hat{v}_{klpmn} \tag{295}$$

For macroscopically orthotropic materials, $\mathbf{D}^1 = 0$, then Eq. 290 becomes:

$$\langle \rho H_{ikl} \rangle D^0_{ipmn} = -\rho_0 \hat{w}_{klpmn} \tag{296}$$

Noting that ρ_0 is independent of $\mathbf{H}(\mathbf{y})$, and that $\hat{\mathbf{w}}$ and $\mathbf{D}^0$ are independent of ρ, only the trivial solution is satisfied for an arbitrary chosen density variation within the microstructure:

$$\langle \rho H_{ikl} \rangle = 0 \tag{297}$$

Appendix C

MOORE-PENROSE PSEUDO-INVERSE

The Moore-Penrose pseudo-inverse $\mathbf{A}^{\text{-mp}}$ of a matrix $\mathbf{A}$ is a generalization of the inverse matrix. Let $\mathbb{K}$ denote one of the fields of real or complex numbers, $M(m,n;\mathbb{K})$ denote the vector space of $m \times n$ matrices over $\mathbb{K}$. For $\mathbf{A} \in M(m,n;\mathbb{K})$, a Moore-Penrose pseudo-inverse of $\mathbf{A}$ is defined as a matrix $\mathbf{A}^{\text{-mp}} \in M(n,m;\mathbb{K})$ satisfying all of the following four criteria:

$$\mathbf{A}\mathbf{A}^{\text{-mp}}\mathbf{A} = \mathbf{A} \tag{298}$$

$$\mathbf{A}^{\text{-mp}}\mathbf{A}\mathbf{A}^{\text{-mp}} = \mathbf{A}^{\text{-mp}} \tag{299}$$

$$(\mathbf{A}\mathbf{A}^{\text{-mp}})^{*} = \mathbf{A}\mathbf{A}^{\text{-mp}} \tag{300}$$

$$(\mathbf{A}^{\text{-mp}}\mathbf{A})^{*} = \mathbf{A}^{\text{-mp}}\mathbf{A} \tag{301}$$

where the superscript $*$ denotes the Hermitian transpose. Moore - Penrose pseudo-inverse exists and is unique. Equations 298 and 299 define the generalized inverse and Eqs. 300 and 301 determine the uniqueness of the pseudo-inverse of $\mathbf{A}$.

BIBLIOGRAPHY

[1] A. R. Abu, K. Rashid, and G. Z. Voyiadjis. A Finite Strain Plastic-Damage Model for High Velocity Impact Using Combined Viscosity and Gradient Localization Limiters: Part I-Theoretical Formulation. *Int. J. Damage Mech.*, 15(4): 293–334, 2006.

[2] I. Abu-Alshaikh, D. Turhan, and Y. Mengi. Propagation of transient out-of-plane shear waves in viscoelastic layered media. *Int. J. Mech. Sci.*, 43:2911–2928, 2001.

[3] M. R. Amini, J. Isaacs, and S. Nemat-Nasser. Investigation of Effect of Polyurea on Response of Steel Plates to Impulsive Loads in Direct Pressure-Pulse Experiments. *Mech. Mater.*, 42(6):628–639, 2010.

[4] M.R. Amini, J. Simon, and S. Nemat-Nasser. Numerical Modeling of Effect of Polyurea on Response of Steel Plates to Impulsive Loads in Direct Pressure-pulse Experiments. *Mech. Mater.*, 42(6):615–627, 2010.

[5] A. V. Amirkhizi, J. Isaacs, J. McGee, and S. Nemat-Nasser. An Experimentally-Based Viscoelastic Constitutive Model for Polyurea, Including Pressure and Temperature Effects. *Philos. Mag.*, 86(36):5847–5866, 2006.

[6] I. V. Andrianov, V. I. Bolshakov, V. V. Danishevs'kyy, and D. Weichert. Higher order asymptotic homogenization and wave propagation in periodic composite materials. *Proc. R. Soc. Lond. A*, 464(2093):1181–1201, 2008.

[7] I. V. Andrianov, V. V. Danishevs' kyy, H. Topol, and D. Weichert. Homogenization of a 1d nonlinear dynamical problem for periodic composites. *ZAMM-Journal of Applied Mathematics and Mechanics/Zeitschrift für Angewandte Mathematik und Mechanik*, 91(6):523–534, 2011.

[8] I. V. Andrianov, V. V. Danishevs'kyy, O. I. Ryzhkov, and D. Weichert. Dynamic homogenization and wave propagation in a nonlinear 1d composite material. *Wave Motion*, 2012.

[9] Y. A. Bahei-El-Din, G. J. Dvorak, and O. J. Fredricksen. A Blast-Tolerant Sandwich Plate Design with A Polyurea Interlayer. *Int. J. Solids Struct.*, 43 (25-26):7644–7658, 2006.

[10] N. Bakhvalov and G. Panasenko. *Homogenisation: averaging processes in periodic media*. Mathematical problems in the mechanics of composite materials. Springer, 1989.

[11] N. Bakhvalov and G. Panasenko. Homogenisation: averaging processes in periodic media (mathematical problems in the mechanics of composite materials). *Recherche*, 67:02, 1989.

[12] N. S. Bakhvalov and M. E. Eglit. Equations of higher order of accuracy describing the vibrations of thin plates. *J. Appl. Math. Mech. USS*, 69:593–610, 2005.

[13] T. Bennett and H. Askes. Finite element modelling of wave dispersion with dynamically consistent gradient elasticity. *Comput. Mech.*, 43(6):815–825, 2009.

[14] T. Bennett, I. M. Gitman, and H. Askes. Elasticity theories with higher-order gradients of inertia and stiffness for the modelling of wave dispersion in laminates. *Int. J. Fract.*, 148:185–193, 2007.

[15] A. Benssousan, J. L. Lions, and G. Papanicolaou. *Asymptotic Analysis for Periodic Structures*. North-Holland, Amsterdam, 1978.

[16] C. Boutin. Microstructural effects in elastic composites. *Int. J. Solids Struct.*, 33:1023–1051, 1996.

[17] L. Brancik. Programs for fast numerical inversion of laplace transforms in matlab language environment. *Sbornik 7. Proc. Matlab 99, Prague*, pages 27–39, 1999.

[18] T. M. Chen. A modified hybrid laplace transform/finite element method for transient heat conduction problems. *Comput. Methods Appl. Mech. Engrg.*, 98: 261–272, 1992.

[19] W. Chen and J. Fish. A dispersive model for wave propagation in periodic heterogeneous media based on homogenization with multiple spatial and temporal scales. *ASME J. Appl. Mech.*, 68:153–161, 2001.

[20] S. Chin-Teh. Transient rotary shear waves in nonhomogeneous viscoelastic media. *Int. J. Solids Struct.*, 7:25–37, 1971.

[21] ASM International. Handbook Committee. *ASM Handbook*. ASM International, 1992. ISBN 0871703785.

[22] E. Cosserat and F. Cosserat. *Theorie des Corps Deformables*. Hermann & Fils, Paris, France., 1909.

[23] J. A. Cottrell, Thomas J. R. Hughes, A. Reali, and G. Sangalli. Isogeometric discretizations in structural dynamics and wave propagation. In *ECOMAS Thematic Conference on Computational Methods in Structural Dynamics and Earthquake Engineering, Crete, Greece*, pages 13–16, 2007.

[24] R. Crouch and C. Oskay. Symmetric meso-mechanical model for failure analysis of heterogeneous materials. *Int. J. Mult. Comp. Eng.*, 8:447–461, 2010.

[25] J. F. Dube, G. Pijaudier-Cabot, and C. La Borderie. Rate dependent damage model for concrete in dynamics. *J. Engng. Mech.*, 122(10):939–947, 1996.

[26] T. El Sayed, A. Mota, F. Fraternali, and M. Ortiz. A Variational Constitutive Model for Soft Biological Tissues. *J. Biomech.*, 41(7):1458–1466, 2008.

[27] T. El Sayed, W. Mock, A. Mota, F. Fraternali, and M. Ortiz. Computational Assessment of Ballistic Impact on A High Strength Structural Steel/Polyurea Composite Plate. *Comput. Mech.*, 43(4):525–534, 2009.

[28] J. Engelbrecht, A. Berezovski, F. Pastrone, and M. Braun. Waves in microstructured materials and dispersion. *Philos. Mag.*, 85:4127–4141, 2005.

[29] C. Eringen and E. S. Suhubi. Nonlinear theory of micro-elastic solids ii. *Int. J. Eng. Sci.*, 2:189–203, 1964.

[30] J. Fish, W. Chen, and G. Nagai. Non-local dispersive model for wave propagation in heterogeneous media: multi-dimensional case. *Int. J. Numer. Methods Eng.*, 54:347–363, 2002.

[31] J. Fish, W. Chen, and G. Nagai. Non-local dispersive model for wave propagation in heterogeneous media: one-dimensional case. *Int. J. Numer. Methods Eng.*, 54: 331–346, 2002.

[32] J. Fish, V. Filonova, and S. Kuznetsov. Micro-inertia effects in nonlinear heterogeneous media. *Int. J. Numer. Meth. Engng.*, 91:1406–1426, 2012.

[33] D. Fragiadakis, R. Gamache, R. B. Bogoslovov, and C. M. Roland. Segmental Dynamics of Polyurea: Effect of Stoichiometry. *Polym. J.*, 51(1):178–184, 2010.

[34] Y. Fung. *Foundations of solid mechanics.* Prentice Hall, Englewood Cliffs, New Jersey, 1965.

[35] S. Gonella, M. S. Greene, and W. Kam Liu. Characterization of heterogeneous solids via wave methods in computational microelasticity. *J. Mech. Phys. Solids*, 59:959–974, 2011.

[36] M. Grujicic, W.C. Bell, B. Pandurangan, and T. He. Blast-Wave Impact-Mitigation Capability of Polyurea When Used as Helmet Suspension Pad Material. *Mater. Des.*, 31:4050–4065, 2010.

[37] M. Grujicic, B. Pandurangan, and T. He. Computational Investigation of Impact Energy Absorption Capability of Polyurea Coatings via Deformation-Induced Glass Transition. *Mater. Sci. Eng., A*, 527:7741–7751, 2010.

[38] J. M. Guedes and N. Kikuchi. Preprocessing and postprocessing for materials based on the homogenization method with adaptive finite element methods. *Comput. Meth. Appl. Mech. Engrg.*, 83:143–198, 1990.

[39] T. Hui and C. Oskay. A nonlocal homogenization model for wave dispersion in dissipative composite materials. *Int. J. Solids Struct.*, 50(38-48), 2013.

[40] Y. Jiangong. Viscoelastic shear horizontal wave in graded and layered plates. *Int. J. Solids Struct.*, 48:2361–2372, 2011.

[41] M. Kafesaki, M. M. Sigalas, and E. N. Economou. Elastic wave band gaps in 3-d periodic polymer matrix composites. *Solid State Commun.*, 96(5):285–289, 1995.

[42] C. Li and J. Lua. A Hyper-Viscoelastic Constitutive Model for Polyurea. *Mater. Lett.*, 63(11):877–880, 2009.

[43] J. R. Macdonald. Accelerated convergence, divergence, iteration, extrapolation, and curve fitting. *J. Appl. Phys.*, 35:3034–3041, 1964.

[44] B. Merheb, P. A. Deymier, M. Jain, M. Aloshyna-Lesuffleur, S. Mohanty, A. Berker, and R. W. Greger. Elastic and viscoelastic effects in rubber/air acoustic band gap structures: A theoretical and experimental study. *J. Appl. Phys.*, 104(6):064913, 2008.

[45] R. D. Mindlin. Micro-structure in linear elasticity. *Arch. Ration. Mech. Anal.*, 16:51–78, 1964.

[46] R. P. Moiseyenko and V. Laude. Material loss influence on the complex band structure and group velocity in phononic crystals. *Phys. Rev. B: Condens. Matter*, 83(6):064301, 2011.

[47] S. Mukherjee and E. H. Lee. Dispersion relations and mode shapes for waves in laminated viscoelastic composites by finite difference methods. *Comput. Struct.*, 5:279–285, 1975.

[48] T. Naciri, P. Navi, and A. Ehrlacher. Harmonic wave propagation in viscoelastic heterogeneous materials part i: Dispersion and damping relations. *Mech. Mater.*, 18:313–333, 1994.

[49] A. H. Nayfeh. Discrete lattice simulation of transient motions in elastic and viscoelastic composites. *Int. J. Solids Struct.*, 10:231–242, 1974.

[50] A. Needleman. Material rate dependence and mesh sensitivity in localization problems. *Comput. Meth. Appl. Mech. Engng.*, 67:69–86, 1988.

[51] R. O. Ochola, K. Marcus, G. N. Nurick, and T. Franz. Mechanical Behaviour of Glass and Carbon Fibre Reinforced Composites at Varying Strain Rates. *Compos. Struct.*, 63(3-4):455–467, 2004.

[52] K. Oguni and G. Ravichandran. Dynamic Compressive Behavior of Unidirectional E-glass/Vinylester Composites. *J. Mater. Sci.*, 36(4):831–838, 2001.

[53] J. H. Oh, Y. J. Kim, and Y. Y. Kim. Wave attenuation and dissipation mechanisms in viscoelastic phononic crystals. *J. Appl. Phys.*, 113(10):106101, 2013.

[54] C. Oskay and J. Fish. Eigendeformation-based reduced order homogenization for failure analysis of heterogeneous materials. *Comput. Meth. Appl. Mech. Eng.*, 196:1216–1243, 2007.

[55] C. Oskay and G. Pal. A multiscale failure model for analysis of thin heterogeneous plates. *Int. J. Damage Mechanics*, 19:575–611, 2010.

[56] S. A. Papanicolopulos, A. Zervos, and I. Vardoulakis. A three-dimensional c1 finite element for gradient elasticity. *Int. J. Numer. Methods Eng.*, 77(10):1396–1415, 2009.

[57] P. Perzyna. Fundamental Problems in Viscoplasticity. *Adv. Appl. Mech.*, 9(2): 244–368, 1966.

[58] A. V. Porubov, E. L. Aero, and G. A. Maugin. Two approaches to study essentially nonlinear and dispersive properties of the internal structure of materials. *Phys. Rev. E*, 79:046608, 2009.

[59] I. E. Psarobas. Viscoelastic response of sonic band-gap materials. *Phys. Rev. B: Condens. Matter*, 64(1):012303, 2001.

[60] K. Ravi-Chandar and J. Niemczura. Tensile Shock Waves in Rubber. In *Bulletin of the American Physical Society*, volume 56. American Physical Society, 2011.

[61] L. Ren and R. Zhang. Hybrid laplace transform finite element method for solving the convection–dispersion problem. *Adv. Water Resour.*, 23:229–237, 1999.

[62] C. M. Roland, J. N. Twigg, Y. Vu, and P. H. Mott. High Strain Rate Mechanical Behavior of Polyurea. *Polym. J.*, 48(2):574–578, 2007.

[63] R. Roy, B. K. Sarkar, and N. R. Bose. Impact Fatigue of Glass Fibre-Vinylester Resin Composites. *Composites Part A*, 32(6):871–876, 2001.

[64] M. B. Rubin, P. Rosenau, and O. Gottlieb. Continuum model of dispersion caused by an inherent material characteristic length. *J. Appl. Phys.*, 77:4054–4063, 1995.

[65] E. Sánchez-Palencia. *Non-homogeneous media and vibration theory*, volume 127. Springer-Verlag, Berlin, 1980.

[66] F. Santosa and W. W. Symes. A dispersive effective medium for wave propagation in periodic composites. *SIAM J. Appl. Math.*, 51:984–1005, 1991.

[67] M. M. Sigalas and E. N. Economou. Elastic waves in plates with periodically placed inclusions. *J. Appl. Phys.*, 75(6):2845–2850, 1994.

[68] J. C. Simo and J. W. Ju. Strain- and stress-based continuum damage models - i. formulation. *Int. J. Solids Struct.*, 23(7):821–840, 1987.

[69] T. Suzuki and P. K. Yu. Tunneling in photonic band structures. *JOSA B*, 12 (5):804–820, 1995.

[70] T. Suzuki and P. K. L. Yu. Complex elastic wave band structures in three-dimensional periodic elastic media. *J. Mech. Phys. Solids*, 46(1):115–138, 1998.

[71] S. A. Tekalur, K. Shivakumar, and A. Shukla. Mechanical Behavior and Damage Evolution in E-Glass Vinyl Ester and Carbon Composites Subjected to Static and Blast Loads. *Composites Part B*, 39(1):57–65, 2008.

[72] S. A. Tekalur, A. Shukla, and K. Shivakumar. Blast Resistance of Polyurea Based Layered Composite Materials. *Compos. Struct.*, 84(3):271–281, 2008.

[73] T. C. T. Ting. The effects of dispersion and dissipation on wave propagation in viscoelastic layered composities. *Int. J. Solids Struct.*, 16:903–911, 1980.

[74] L. Tsai and V. Prakash. Structure of weak shock waves in 2-d layered material systems. *Int. J. Solids Struct.*, 42:727–750, 2005.

[75] J. O. Vasseur, B. Djafari-Rouhani, L. Dobrzynski, M. S. Kushwaha, and P. Halevi. Complete acoustic band gaps in periodic fibre reinforced composite materials: the carbon/epoxy composite and some metallic systems. *J. Phys. Condens. Matter.*, 6(42):8759, 1994.

[76] G. Z. Voyiadjis, A. R. Abu, and K. Rashid. A Finite Strain Plastic-Damage Model for High Velocity Impacts Using Combined Viscosity and Gradient Localization Limiters: Part II-Numerical Aspects and Simulations. *Int. J. Damage Mech.*, 15(4):335–373, 2006.

[77] Z. P. Wang and C. T. Sun. Modeling micro-inertia in heterogeneous materials under dynamic loading. *Wave Motion*, 36:473–485, 2002.

[78] L. Xue, W. Mock, and T. Belytschko. Penetration of Dh-36 Steel Plates with and without Polyurea Coating. *Mech. Mater.*, 42:981–1003, 2010.

[79] E. Yablonovitch and K. M. Leung. Photonic band structure: Non-spherical atoms in the face-centered-cubic case. *Physica B*, 175(1):81–86, 1991.

[80] E. Yablonovitch, T. J. Gmitter, and K. M. Leung. Photonic band structure: The face-centered-cubic case employing nonspherical atoms. *Phys. Rev. Lett.*, 67(17): 2295, 1991.

[81] H. Yan, C. Oskay, A. Krishnan, and L. R. Xu. Compression after Impact Response of Woven Fiber-Reinforced Composites. *Compos. Sci. Technol.*, 70:2128–2136, 2010.

[82] J. Yi, M. C. Boyce, G. F. Lee, and E. Balizer. Large Deformation Rate-Dependent Stress-Strain Behavior of Polyurea and Polyurethanes. *Polym. J.*, 47(1):319–329, 2006.

[83] Y. P. Zhao and P. J. Wei. The band gap of 1d viscoelastic phononic crystal. *Comput. Mater. Sci.*, 46(3):603–606, 2009.